SCUOLA DI DOTTORATO

UNIVERSITÀ DEGLI STUDI DI MILANO-BICOCCA

Department of Materials Science

PhD Course in Science and Nanotechnology of Materials XXIX Cycle

Curriculum in Materials Science

NOVEL MATERIAL DESIGN AND MANIPULATION STRATEGIES FOR ADVANCED OPTOELECTRONIC APPLICATIONS

Francesco Bruni

Registration number: 709727

Tutor: Prof. SERGIO BROVELLI

Coordinator: Prof. GIAN PAOLO BRIVIO

ACADEMIC YEAR 2015/2016

INDEX

In this thesis, I report the results obtained during my PhD, which has been focused on organic semiconductors for photovoltaics and photodetecting applications. Initially, I worked on the control of the morphology in binary blends of small organic molecules and fullerenes using the so called latent pigment approach. Subsequently, I investigated the charge accumulation and polarization effect occurring at the interface between water and a polymeric semiconductor used as optical component in retinal prosthesis by means of inorganic colloidal nanocrystals featuring a ratiometric sensing ability for electron withdrawing agents. As a last part of the work, I focalized on the applications of these nanocrystals as ratiometric sensors for intracellular pH probing and pressure optical monitoring.

Specifically, during the first part of my PhD, I worked in the field of organic photovoltaics on the morphology engineering of the active layer of small molecules bulk-heterojunction solar cells. I demonstrated a new strategy to fine tune the phase-segregation in thin films of a suitably functionalized electron donor blended with fullerene derivatives by introducing in the system a post-deposition thermally activated network of hydrogen bonds that leads to improved stability and high crystallinity. Moreover, this process increases the carrier mobility of the donor species and allows for controlling the size of segregated domains resulting in an improved efficiency of the photovoltaic devices.

This work revealed the great potential of the latent hydrogen bonding strategy that I subsequently exploited to fabricate nanometric semiconductive features on the film surface by using a very simple maskless lithographic technique. To do so, I focalized a UV laser into a confocal microscope and used the objective as a "brush" to thermically induce a localized hydrogen bonding driven crystallization with diffraction limited resolution.

My work on organic semiconductors continued with a study on the surface polarization driven charge separation at the P3HT/water interfaces in optoelectronic devices for biologic applications. In this work, I probed the local accumulation of

positive charges on the P3HT surface in aqueous environment by exploiting the ratiometric sensing capabilities of particular engineered core/shell heterostuctures called dot-in-bulk nanocrystals (DiB-NCs). These structures feature two-colour emission due to the simultaneous recombination of their core and shell localized excitons. Importantly, the two emissions are differently affected by the external chemical environment, making DiB-NCs ideal optical ratiometric sensors.

In the second part of my PhD, I, therefore, focalized on the single particle sensing application of DiB-NCs. Specifically, I used them to ratiometrically probe intracellular pH in living cells. With this aim, I studied their ratiometric response in solution by titration with an acid and a base. Subsequently, I internalized them into living human embryonic kidney (HEK) cells and monitored an externally induced alteration of the intracellular pH. Importantly, viability test on DiB-NCs revealed no cytotoxicity demonstrating their great potential as ratiometric pH probes for biologic application.

Finally, I used DiB-NCs as a proof-of-concept single particle ratiometric pressure sensitive paint (r-PSP). In this application, the emission ratio between the core and the shell emission is used to determine the oxygen partial pressure and therefore the atmospheric pressure of the NC environment.

1 Post-Deposition Activation of Latent Hydrogen Bonding

Small conjugated molecules (SM) are rapidly gaining momentum as a valid alternative to semiconducting polymers for the production of solution-processed bulk heterojunction (BHJ) solar cells, as they allow to overcome current limitations imposed by the intrinsic polydispersity of long conjugated chains and low batch-to-batch reproducibility. The major issue with SM-BHJ solar cells is the low carrier mobility due to the scarce control on the phase segregation process and consequent lack of preferential percolative pathways for free carriers to the extraction electrodes. In this work of thesis, I demonstrate a new paradigm for fine tuning the phase segregation in SM-BHJs based on the post-deposition exploitation of latent hydrogen bonding in binary blends of functionalized electron-donor moieties mixed with PCBM. The strategy consist in the chemical protection of the hydrogen bond forming sites of the donor species with a thermo-labile functionality whose controlled thermal cleavage leads to the formation of highly crystalline, stable, phase-separated molecular aggregates. This approach allows for the fine tuning of the nanoscale film connectivity and thereby to simultaneously optimize the generation of geminate carriers at the donor-acceptor interfaces and the extraction of free charges via ordered phase-separated domains. As a result, the PV efficiency undergoes an over twenty-fold increase with respect to control devices. This strategy, demonstrated here with a binary mixture of diketopyrrolopyrrole derivatives with PCBM can in principle be extended to other molecular systems for achieving highly efficient, stable, small-molecule BHJ solar cells.

1.1 Introduction

1.1.1 Bulk heterojunction solar cells

The field of OPV took a major step forward in 1986, when Tang at Kodak published in Applied Physics Letters his results on the first bi-layer heterojunction solar cell. [1] He proposed a new approach to OPV based on two organic materials with different electronic properties (a p-type semiconductor or "electron donor" and a n-type semiconductors or "electron acceptor") and discovered that that the splitting of the photogenerated exciton in elementary charges is facilitated at the heterointerface between the organic materials, thus improving the photovoltaic performance. The donor-acceptor (D-A) hetrojunction described by Tang has become the central part of all efficient organic solar cells.[2] Following observations clarified that only the excitons generated within a certain distance (diffusion length) to the donor and acceptor interface participated in the photovoltaic process.

Therefore, the bi-layer geometry imposes an intrinsic limit to the generation of the photocurrent. Specifically, for a bi-layer, to efficiently produce separated carriers it is necessary that the donor and acceptor layers are thinner than the diffusion length (typically 10-20 nm), which clearly limits the optical absorption of the active layer. Blending donors and acceptors in an intermixed layer forming a distributed BHJ, rather than keeping a bi-layer geometry, allow to overcome this issue by maximizing the interfaces area and thereby minimizing the distance between the exciton generation spot and the D-A interface.

The ideal structure of a BHJ solar cell is shown in Fig.1.1a and consist of two continuous domains of donor and acceptor phases interpenetrated in a double comb configuration, this assures a large interfacial area and the existence of effective percolation

pathways for electron and holes, connecting the electron acceptor phase to the cathode and the p-type donor region to the anode. In this design, the size of the domains should never exceed twice the value of the diffusion length. Over the last years, several studies have dedicated to the realization of this design, but the creation of interpenetrated molecular domains require the use of expensive and time-consuming lithographic methods which increase the device complexity and rise the fabrication costs.

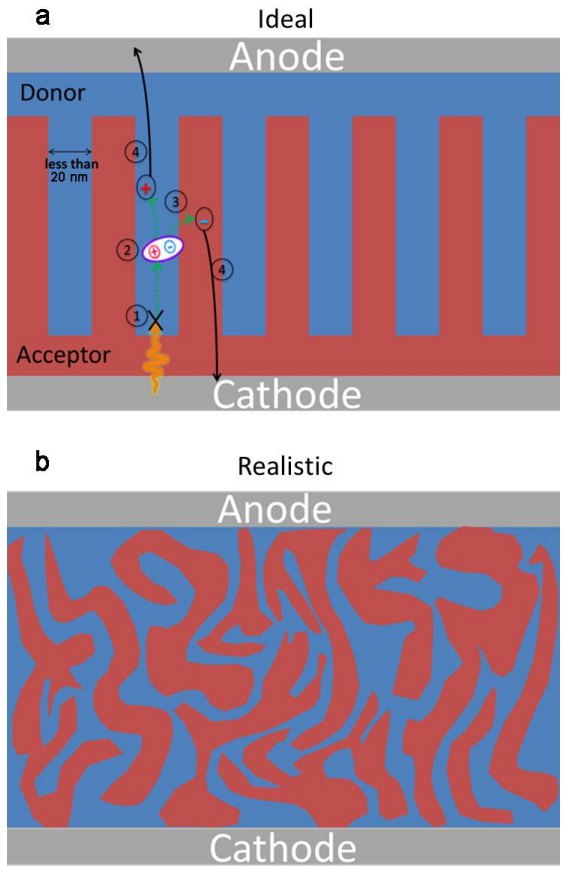

Figure 1.1 **a**) Schematic representation of the ideal interdigitated BHJ solar cell and of the photophysical processes underpinning cell operation: 1. exciton formation, 2. exciton migration, 3. exciton splitting, 4. charge percolation. **b**) Schematic representation of phase segregation in a distributed BHJ solar cell.

For these reason, spontaneous phase segregation of donor and acceptor species is commonly exploited to produce a distributed junction over the bulk of a blended film as shown in Fig.1.1b.

In this system, absorption of a photon generates an exciton (1) which migrates within the diffusion length through the domain until it reaches the D-A interfaces (2). There, the strong local electric field, generated by the abrupt changes of the potential due to the offset between the lowest unoccupied molecular orbital (LUMO) (for electrons) and the highest occupied molecular orbital (HOMO) (for holes) of the donor and acceptor molecules, promotes the ultrafast process of charge separation (3). The free charges can now migrate to the corresponding electrode (4) producing a photocurrent on an external circuit.[3] The energy diagram of a typical D-A interface is reported in Fig.1.2, showing the process of exciton splitting.

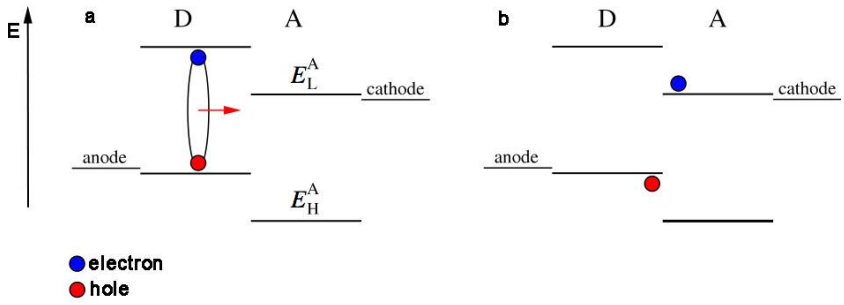

Figure 1.2 Energy diagram of the process of exciton splitting: **a**) Exciton is localized on the donor, **b**) charges are separated at the interface with the acceptor. Because of the offset between the LUMOs of the donor and of the acceptor, the electron is transferred to the acceptor molecules.

The current-voltage characteristics of a solar cell in the dark and under illumination are shown in Fig.1.3. In the dark, there is almost no current flowing for potential lower than the open circuit voltage, above which a small current flows through the device. In contrast, under illumination conditions, the device generates power (between (a) and (b)), which appears as a shift

of the IV curve in the fourth quadrant. At maximum power point (MPP), the product of current and voltage is the largest.

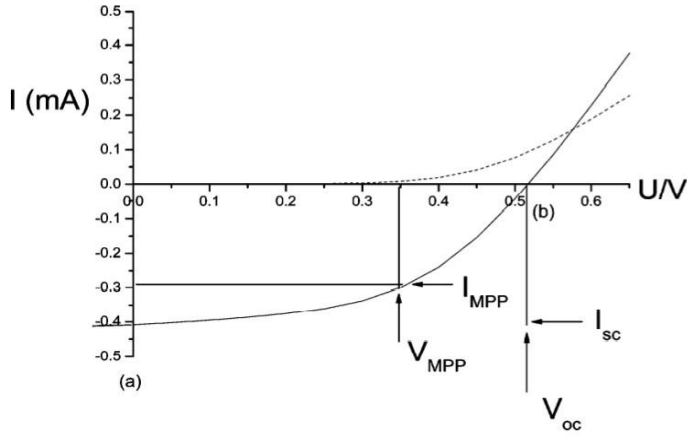

Figure 1.3 Current-voltage (I-V) curves of an organic solar cell (dark, dashed line; illuminated, continuous line). The characteristic intersections with the abscissa and ordinate axis are the open circuit voltage (V_{OC}) and the short circuit current (I_{SC}), respectively. The largest power output (P_{max}) achievable is determined by the point where the product of voltage (V_{MPP}) and current (I_{MPP}) is maximized. Division of P_{max} by the product of I_{SC} and V_{OC} yields the fill factor FF.

The processes described above determine the power conversion efficiency (PCE) η of a solar cell defined as

$$\eta = \frac{FF\ V_{OC}\ J_{SC}}{P_{in}}$$

where FF is the fill factor, V_{OC} the open circuit voltage, J_{SC} the short circuit current density and P_{in} the power density of the incident light. Generally, the PCE is measured and reported under standard AM 1.5 G illumination conditions.[4,5] The fill factor is defined as the ratio of the actual maximum power output to the theoretical power output if both current and voltage are maximum.

$$FF = \frac{P_{max}}{I_{SC}\ V_{OC}} = \frac{I_{MPP}\ V_{MPP}}{I_{SC}\ V_{OC}}$$

I_{MPP} and V_{MPP} are respectively the current and the voltage corresponding to the maximum power production, while I_{SC} is the short circuit current (Fig.1.3).

The origin of V_{OC} is not yet completely understood in organic solar cells. On the one hand, some experimental observation reported dependence by the work function of the electrodes[6,7], while on the other hand it was observed to be independent from the choice of the cathode materials.[8] Although a deeper understanding of V_{OC} is needed, it is commonly accepted that it primarily depends on the offset between the HOMO of the donor and the LUMO of the acceptor.[2,6,9] On the basis of a statistical analysis, a simple empirical formula describing the dependence of V_{OC} on the energy of the HOMO of the donor has been obtained using Phenyl-C61-butyric acid methyl ester (PCBM) as acceptor:[10]

$$V_{OC} = \frac{1}{e}\left(\left|E_{Donor}^{HOMO} - E_{PCBM}^{LUMO}\right|\right) - 0.3$$

Where e is the elementary charge, $E_{\mathrm{Donor}}^{\mathrm{HOMO}}$ and $E_{\mathrm{PCBM}}^{\mathrm{LUMO}}$ are respectively the energy of the HOMO of the donor and the LUMO of the acceptor and 0.3 is an empirical constant. Obviously this correlation is simplified as other important factors should be taken into account for a rigorous discussion, such as molecular structures and film morphology.[11,12] J_{SC} is the density of current flowing in the cell when no voltage is applied to the cell. It depends on the rate of charge separation and on the mobility of the free carriers. Hence, it gives information on how

many excitons are split at the interface and how efficiently the charges are removed from the active layer.

The short circuit current (I_{SC}) is determined by the product of the photoinduced charge carrier density and the charge carrier mobility within the organic semiconductors:

$$I_{SC} = ne\mu E$$

Where n is the density of charge carriers, e is the elementary charge, μ is the mobility, and E is the electric field.[13] Therefore, for a given material, I_{SC} is limited by the mobility. The mobility is not only a material property, but it depends on the nanoscale morphology of the active layer and therefore it should be considered a "device parameter".[14,15]

The benchmark donor materials for BHJ solar cells are conjugated semiconducting polymers such as poly 3-hexylthiophene (P3HT) and its derivatives. As for the acceptor materials, the performances of fullerene derivatives, such as PCBM, are unsurpassed and only marginal research is devoted to the development of substitutes.[16,17]

In polymer based BHJs, phase segregation is a spontaneous process determined by low entropy of mixing between conjugated polymers and fullerene derivatives. However, polymers are affected by intrinsic problems such as chain length polydispersity, batch-to-batch variation, difficult purification, and indistinct intermolecular packing that hinder the reproducibility of the devices on a large scale.[18] A way to overcome these problems is to replace polymers with small conjugated molecules, which are characterized by a well defined molecular weight as well as the fact that they can be easily synthetized with high purity.

1.1.2 Small molecule solar cells

Small molecules solar cells do not suffer the problems of polymeric ones because they can be synthetized with high purity and monodisperse molecular weight. As a result, small molecules are gaining interest as candidates for a new generation of efficient BHJ solar cells. Over the last few years, a large variety of donor materials based on conjugated small molecules has been synthetized.[19] However, despite their potential, small molecules have two major drawbacks that have to be overcome for reaching the performances of state of the art polymeric solar cells. The first issue is that the high entropy of mixing with fullerene derivative makes the process of phase segregation no longer spontaneous.[20] Therefore, new approaches have to be developed to induce phase segregation necessary to the production of the BHJ with controlled nanomorphology. In this regard, a widely used strategy is to exploit π-π interactions between the conjugated moieties. For example, morphological studies on molecular bends show that π-π interaction can be controlled by varying the length of the alkyl the substituents on diketopyrrolopyrrole (DPP) molecules.[11,21] However π-π interaction are typically weak and the resulting aggregate are unstable. Furthermore secondary interactions are barely strong enough to provide a driving force for effective phase segregation.

The second issue is that charge-transport in organic semiconductor solids is via intramolecular hopping. Each hopping step, from a molecular site to the next, takes a finite time to occur, which results in low mobility. This limit is typically circumscribed to donor species, since fullerene derivatives exhibit relatively high electron mobility (~10^{-1} $cm^2 V^{-1} s^{-1}$ measured in field effect transistors).[22] Therefore, the challenge is to obtain high mobility donor materials.[23] Once again, controlling π-π interactions between the donor molecules is the most common strategy to promote molecular assembly resulting in a higher mobility.

1.2 The latent pigment strategy

With respect to traditional silicon solar cells where free charges are generated directly upon photoexcitation, splitting of excitons in organic semiconductors requires to overcome a larger potential barrier (exciton binding energy >50 meV)[24,25] owing to the lower dielectric constant of the medium. In BHJ solar cells, this is typically achieved by mixing materials with different electron affinity and oxidation potential, so as to form distributed interfaces where excitons are split in geminate electron-hole pairs by ultrafast charge transfer processes[26-29]. Because of the typical homopolar conductivity of organic materials, the transport of electrons and holes to the respective electrodes requires preferential percolation pathways of p- and n-type character that are formed by separating the donor and the acceptor moieties in phase segregated domains. In order to optimize the photovoltaic efficiency it is therefore pivotal to finely balance the degree of mixing: on the one hand, a fine interpenetration assures that the size of segregated domains does not exceed the exciton diffusion length, which would suppress exciton splitting into geminate e-h pairs at the donor/acceptor interface; on the other hand, phase separation into highly conductive crystalline domains, promotes efficient long-range geminate charge separation and transport[30-33].

In polymer-fullerene blends, phase segregation happens spontaneously due to their unfavourable entropy of mixing, yielding highly interpenetrated phase separated domains (10-20 nm in size)[34] whose extent can be further controlled through post processing techniques, such as thermal or solvent vapour annealing[35-37]. In contrast, phase separation in SM-BHJs lacks of entropic contribution and therefore requires an additional driving force to occur. In order to address this issue, several groups have adopted various approaches including the exploitation of different solubility of the blend constituents in the processing solvents[38], the insertion of additives[39] and the

adoption of post-processing procedures such as solvent vapour and/or thermal annealing[12,21]. Phase segregation can be further promoted by increasing the dipolar character of the donor species or by exploiting π-π interactions between neighbouring conjugated moieties that result in intermolecular aggregation and the formation of close packed crystalline domains[40,41]. Even when successful in inducing phase-separation, these approaches typically introduce no cohesive forces capable of stabilizing the processed blend in a desired optimized morphology. The resulting phase separation is therefore inherently unstable and subject to changes due to temperature or to the exposure to environmental agents, such as moisture or solvents. To date, fine control of phase separation represents the most critical challenge for boosting the efficiency of SM-BHJ solar cells. Specifically, in contrast to polymer BHJs where the film morphology and segregation can be finely controlled through simple annealing procedures owing to the low molecular mobility of long polymeric chains, thermal annealing of small-molecule BHJs leads to rapid and therefore less controllable segregation that may results in suppression of exciton splitting and consequent reduction of photovoltaic activity[42].

In this work, I demonstrate a new paradigm for external fine control of phase segregation in SM-BHJs that rises the device efficiency of over twenty times with respect to unprocessed devices. The strategy consists in the post-deposition activation of a network of latent hydrogen-bonds (H-bonds) between functionalized donor molecules blended with PCBM through thermally induced decomposition of labile protecting groups that prevent the H-bonding from occurring in the as-deposited films. This "latent pigment" concept was initially introduced for increasing the solution processability of molecular pigments[43,44] and, more recently, it has been applied to increase the charge mobility in ambipolar organic transistors through the formation of highly ordered molecular arrangements[45-48]. The key aspect of the approach, schematically depicted in Fig.1.4, is the temporary "deactivation" of the H-bond-forming sites of the donor

molecule by its protection with a thermally labile functionality. This makes the donor miscible with PCBM in common solvents, allowing for the use of conventional solution-based deposition methods on transparent conductive substrates. The formation of phase-segregated domains is successively finely tuned by thermal cleavage of the protective group and consequent activation of the H-bonding sites.

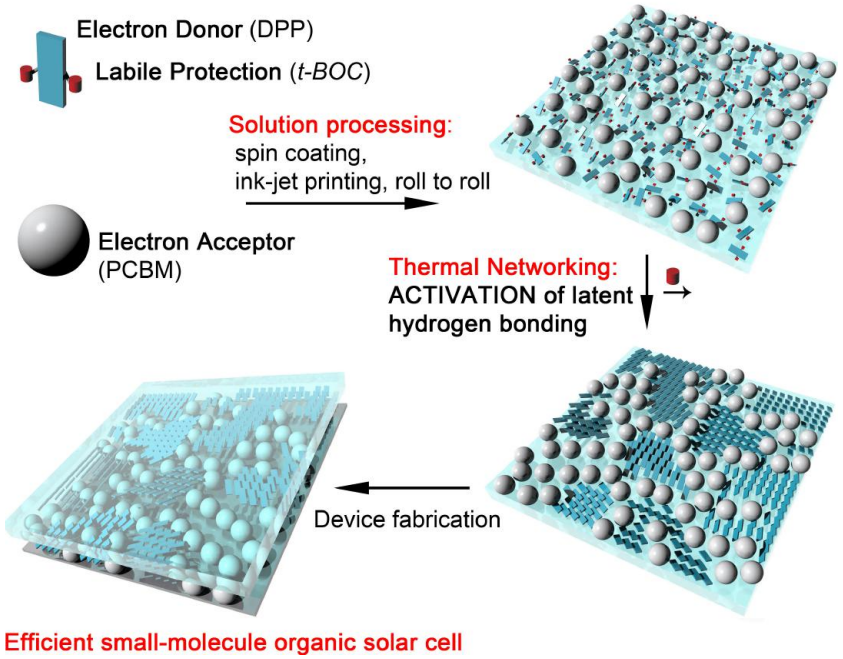

Figure 1.4 Schematic representation of the latent H-bonding strategy in the fabrication of SM-BHJ solar cells. A solution of protected donor and acceptor molecules are deposited on transparent conductive substrates via simple solution processing (i.e. pin coating, roll-to-roll printing). The post-deposition thermal treatment removes the thermolabile protective functionalities thereby activating the latent H-bonding sites. As a result, the donor moieties network leading to a fine controlled phase segregated polycrystalline film. Deposition of the extraction electrodes is carried out by standard procedures.

Through this approach, Ican control the blend morphology from the initial kinetic structures formed during film deposition (i.e.

evaporation of the solvent during spin coating) all the way to thermodynamic macrophase-separated materials and thereby access intermediate morphologies that simultaneously optimize the charge separation efficiency at the donor/acceptor interfaces and charge mobility through the formation of interpenetrated phase separated percolation pathways.

1.2.1 Materials

The material I used in my work is a functionalized diketopyrrolopyrrole (DPP) derivative as electron donor blended with a conventional PCBM acceptor. DPP derivatives have recently received considerable attention as efficient donor materials thanks to their high polarizability and good self-assembly properties arising from their planar conjugated bi-cyclic structure that promotes π-π interaction in the solid state[49]. Furthermore, the electron withdrawing DPP core can be functionalized with electron rich substituents, which confer to the molecule a donor-acceptor-donor (D-A-D) character. The resulting intramolecular charge transfer process provides an additional mean to tune the absorption spectrum so as to cover the whole visible spectral region[18,21].

My molecule of choice is di-tert-butyl3,6-di(biphenyl-4-yl)-1,4-dioxopyrrolo[3,4-c]pyrrole-2,5(1H,4H)-dicarboxylate (hereafter referred to as DPP_H), a D-A-D functionalized DPP whose lactamic nitrogens are protected by tert-butoxycarbonyl (t-BOC) groups (highlighted in red in Fig 1.5). The decomposition of the t-BOC functionalities into gaseous species (CO_2 and isobutene) triggers the formation of H-bonds between neighbouring DPP_H molecules leading to the desired phase segregation.

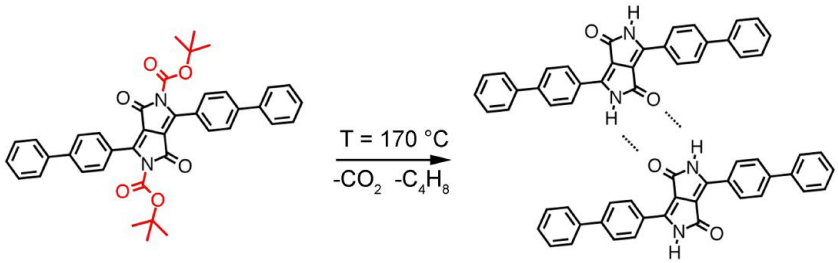

Figure 1.5 Activation of latent H-bonding in di-tert-butyl3,6-di([1,1'-biphenyl]-4-yl)-1,4-dioxopyrrolo[3,4-c]pyrrole-2,5(1H,4H)-dicarboxylate (DPP_H). At 170°C the ter-butoxycarbonyl (t-BOC) protection group (highlighted in red) is converted in carbon dioxide (CO_2) and isobutene (C_4H_8).

Morphological and structural analyses reveal the gradual evolution of the amorphous and uniform pristine film into a mosaic of segregated crystalline domains. The separation of donor and acceptor species is confirmed by spectroscopic measurements that show the progressive increase of the DPP_H luminescence in thermally treated ("deprotected") films, index of slightly reduced ultrafast exciton splitting that instead completely quenches the emission of the pristine "protected" blend. Despite the partially suppressed exciton splitting in phase segregated films, the improved charge mobility leads to a dramatic increase of the short circuit current, and thereby boosts the power conversion efficiency up to twenty times that of pristine devices. In order to unambiguously ascribe the observed improvement of the PV performances to the activation of latent H-bonding network, a control molecule, 3,6-di(biphenyl-4-yl)-2,5-bis(2-ethylhexyl)-2,5-dihydropyrrolo[3,4-c]pyrrole-1,4-dione was synthesised (referred to as DPP_C, Fig 1.6) with similar structure to DPP_H except for the protection of the lactamic nitrogens which, in this case, is provided by 2-ethylhexyl alkyl chains that are stable at the processing temperature and thus unaffected by the thermal treatment. Thermal annealing of the control blends leads to minor changes in the film structure that remains amorphous and to the disruption of the photovoltaic activity, most likely due to uncontrollable complete segregation of DPP_C molecules in nearly pure amorphous domains.

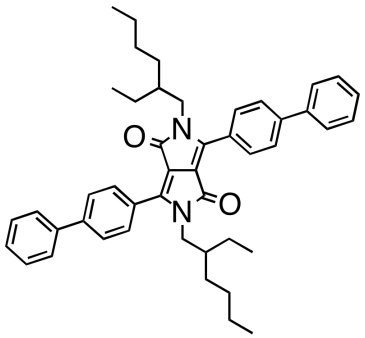

Figure 1.6 Structure of 3,6-di([1,1'-biphenyl]-4-yl)-2,5-bis(2-ethylhexyl)-2,5-dihydropyrrolo[3,4-c]pyrrole-1,4-dione (DPP_C).

1.2.2 Results

Thermal activation of intramolecular aggregation

I start the study by providing evidence of controlled thermal decomposition of the t-BOC protective functionality and consequent formation of intermolecular DPP_H aggregates. In Fig.1.7 I report the thermogravimetric analysis (TGA) of DPP_H powder and the respective mass release curves as obtained through coupled mass spectroscopy measurements on the exhaust gases. At 200°C, a first 29% weight loss is observed with concomitant emission of CO_2 and C_4H_8, as expected for the thermal cleavage of the protective t-BOC group. DPP_H is otherwise stable up to 500°C where a further 40% mass loss and corresponding CO_2 emission indicates the degradation of the DPP core.

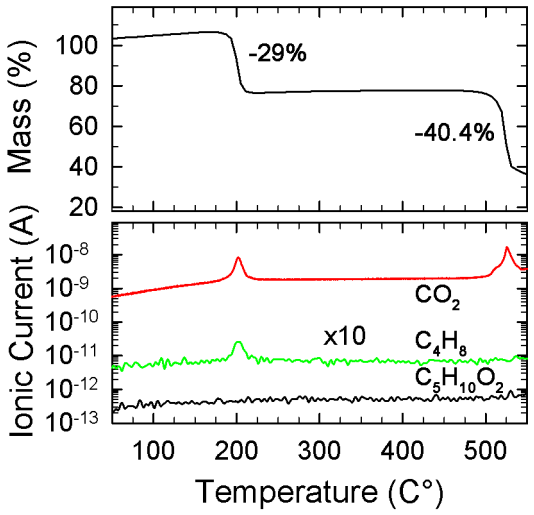

Figure 1.7 Thermogravimetric analysis (TGA) of DPP_H powder performed under nitrogen atmosphere (upper panel) and related mass release curves (lower panel) identifying the emission of CO_2 (red line), C_4H_8 (green line) and $C_5H_{10}O_2$ (black line). The green curve has been shifted upwards by 10 times for clarity.

The thermogram provides an indication of the thermal budget necessary to convert DPP_H into its deprotected form. In order to fine tune the thermal activation of hydrogen networking, Ichose to provide the required thermal budget by heating the samples at 170°C, which is slightly below the peak deprotection temperature of ~200°C. This allows me to slow down the hydrogen networking process and thereby to control its extent through the duration of the thermal treatment, hereafter expressed in terms of thermal treatment time (t_{TT}).

Thermal deprotection and consequent activation of H-bonding sites is confirmed by Fourier transform infrared (FT-IR) transmission measurements that allow to monitor the evolution of the functional groups in the film at different stages of the thermal treatment (Fig.1.8) through the intensity of their characteristic vibrational modes.

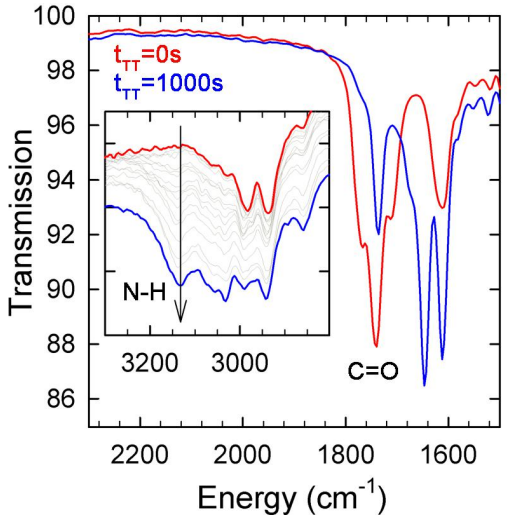

Figure 1.8 IR transmission spectra of pristine (red line) and fully converted (t_{TT} = 1000s , blue line) DPP_H:PCBM films (1:1 wt%) showing the drop of the C=O stretching mode upon thermal deprotection. Inset: IR transmission spectra in the 2800-3300 cm^{-1} region characteristic of N-H stretching mode.

Upon annealing, the characteristic signal of the C=O stretching mode at 1740 cm^{-1} is reduced to below 50% of its initial intensity,

indicating the successful removal of the t-BOC protective groups (the residual signal is due to the C=O bond of PCBM). Most importantly, the characteristic signal of the N-H stretching mode between 3000 cm^{-1} and 3200 cm^{-1} concomitantly grows, confirming the activation of H-bonding sites. As a result of thermal deprotection, DPP_H moieties progressively aggregate both in pure and blended films.

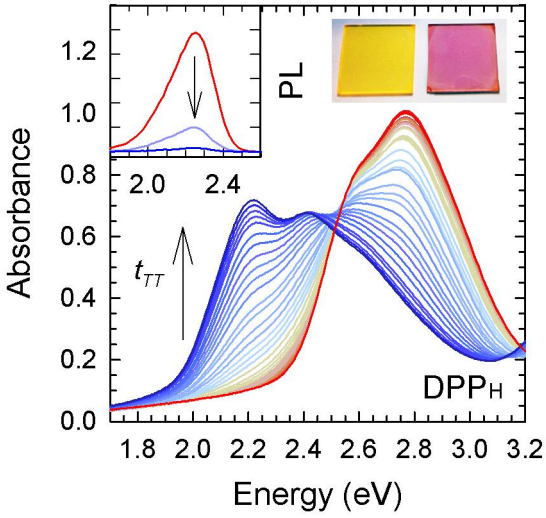

Figure 1.9 Absorption spectra of a pure DPP_H film for increasing treatment time, t_{TT}. The photoluminescence spectra of the pure DPP_H film excited at 400 nm are shown in the inset together with the photographs of the samples before (yellow films) and after 1000s thermal treatment at 170°C (red films).

Figure 1.9 shows the absorption spectrum of a pure DPP_H film as a function of the thermal treatment time, t_{TT} =0-1000 s. The pristine DPP_H film shows an absorption spectrum with a first band at about 2.7 eV that well resembles the absorption profile of the diluted solution (Fig.1.10) and is therefore ascribed to non-interacting DPP_H molecules.

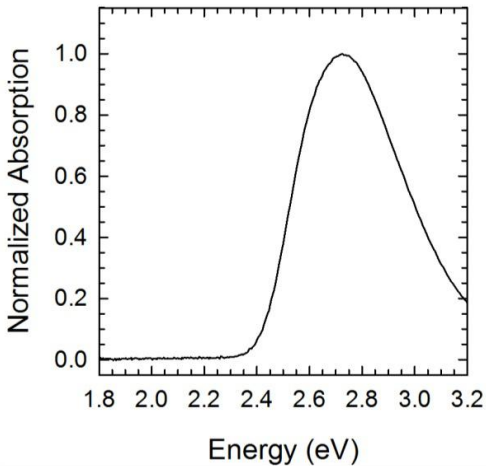

Figure 1.10 UV-Vis absorption spectrum of a diluted solution of DPP_H in chloroform.

The thermal deprotection induces a progressive drop of the 2.7 eV absorption feature with increasing t_{TT}, accompanied by the growth of a lower energy band at 2.2 eV ascribed to molecular aggregates, with a clear isosbestic point at 2.5 eV. Accordingly, the DPP_H photoluminescence (PL) is progressively quenched (inset of Fig.1.9), possibly due to increased exciton mobility in the aggregated film that allows excitons to rapidly reach non-radiative quenching sites or to the lower emission efficiency of aggregates.

Similar evolution of the absorption spectrum is observed for a 1:1 DPP_H:PCBM blended film where the absorption profile of DPP_H is overlapped to the absorption spectrum of PCBM (Fig.1.11). Also in this case, the thermal treatment leads to progressive growth of the absorption band at 2.2 eV, thus confirming that DPP_H moieties aggregate following deprotection also in the blended film.

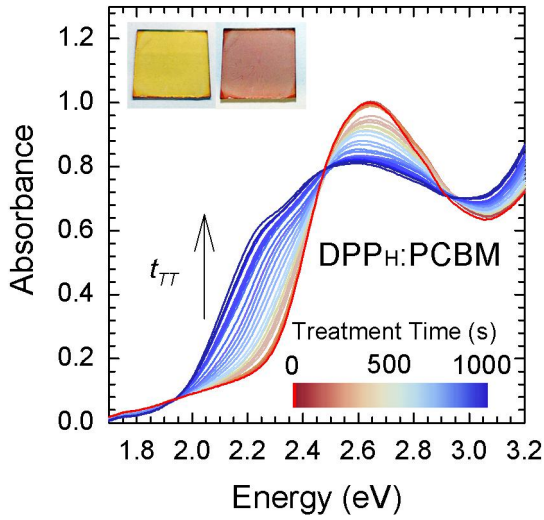

Figure 1.11 Absorption spectra of a DPP_H:PCBM (1:1 wt%) blend film for increasing treatment time, t_{TT}. The photograph of the sample before (yellow films) and after 1000s thermal treatment at 170°C (brown-red films) are shown in the inset.

In contrast, UV-Vis absorption measurements on control films of pure DPP_C and DPP_C:PCBM 1:1 blend show no aggregate band at any t_{TT} (Fig.1.12), thus confirming the key role of H-networking activated by thermal removal of the t-BOC protection as a driving force for intermolecular aggregation in the solid state.

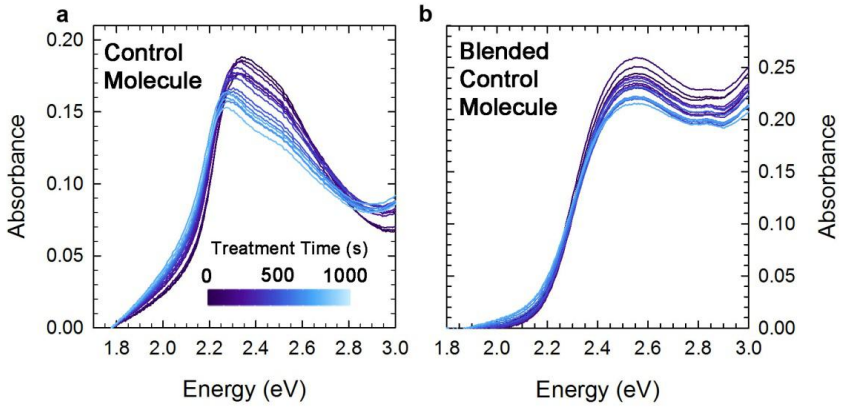

Figure 1.12 UV-Vis absorption spectrum of a film of **a**) pure DPP_C and **b**) DPP_C blended with PCBM (1:1 wt) as a function of t_{TT}.

Morphological and structural analyses

As mentioned above, the key advantage of the proposed strategy is the ability to externally tune the film morphology and phase segregation through the thermal activation of latent H-bonds. To demonstrate the control over film morphology and crystal structure I performed atomic force microscopy (AFM) and X-ray diffraction (XRD) measurements on pure DPP_H and blended films at different stages of thermal treatment. Figure 1.13a and 1.13b report the AFM images and XRD patterns of a 100 nm DPP_H:PCBM (1:1) film on a Si(100) substrate both as-spun and for t_{TT} up to 510 s. The pristine film shows uniform morphology with roughness (rms) below 1 nm and no evident diffraction signal, indicating a substantially amorphous state. After a 30 s thermal treatment, the film surface becomes structured with the formation of elongated lamellar domains with thickness of about 1 nm. The surface roughness undergoes a three-fold increase with respect to its initial value (Table 1).

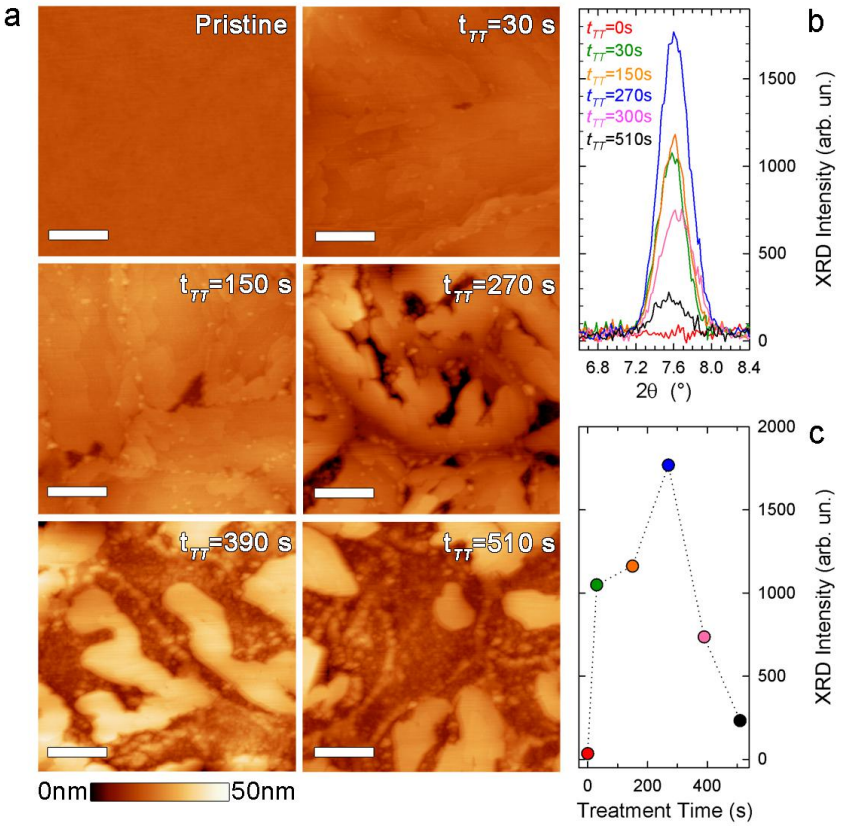

Figure 1.13 Development of crystalline phase segregated domains through activation of latent H-bonds in DPP_H:PCBM blends. **a**) AFM surface topography of DPP:PCBM (1:1 wt%) films on Si(100) substrates as measured at room temperature after thermal treatments performed for the time reported on the top-right of each panel. The white scale bar corresponds to 400 nm. The corresponding surface roughness is reported in Table 1. **b**) X-ray diffraction patterns collected in Bragg-Brentano configuration for the same films as in 'a' showing the XRD peak corresponding to the out-of-plane spacing d = 1.12 nm of the crystal phase of unprotected DPP_H. **c**) Evolution of the integrated intensity of the peak with thermal treatment time. The same colour code applies throughout the figure.

	Roughness (nm)	
t_{TT} (s)	pure DPP_H	DPP_H:PCBM
0	3.30	0.41
30	11.26	2.43
150	9.71	3.18
270	8.37	8.05
390	11.39	8.56
510	13.15	8.25
630	18.24	6.91
750	15.39	8.63
870	9.00	5.17

Table 1 Roughness of pure and blended DPP_H films calculated on 3x3 μm^2 images.

The XRD pattern shows a sharp diffraction peak at $2\theta = 7.6°$ (with replicas up to the fifth order) which are indicative of the development of a crystalline phase with the highest out-of-plane periodicity with spacing of 1.12 nm, consistent with the morphological features observed in the respective AFM image. Extended treatments up to t_{TT}=270 s induce a further increase in crystallinity and the formation of 10-20 nm three-dimensional crystalline domains. Importantly, while the volume fraction of the crystalline phase grows, resulting in more intense XRD signal, the diffraction peak is substantially broader with respect to shorter treatments, which indicates the polycrystalline nature of the film. Longer annealing has a further effect on the surface morphology as the XRD signal broadens and drops in intensity accompanied by a substantial blurring of the morphologic features. The whole process is in any case fully reproducible and thus controllable at any required treatment timescale. The same evolution of the film structure is observed for pure DPP_H films while pure PCBM films are unaffected by the thermal treatment. This suggests that the presence of PCBM does not sensibly

interfere with the thermal activation of the H-network, in agreement with the optical absorption measurements reported in Fig.1.11.

To further investigate the structural changes of the film during the thermal treatment that result in a non-trivial behaviour of the crystallinity, I performed differential scanning calorimetry (DSC) and grazing incidence wide angle X-ray scattering (GIWAXS) measurements at different stages of thermal treatment on pure DPP_H samples.

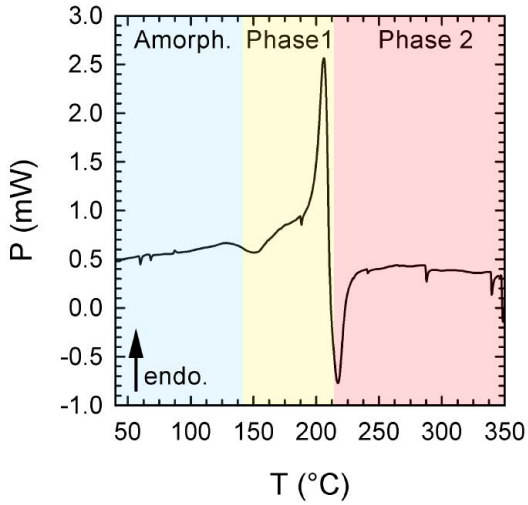

Figure 1.14 Differential scanning calorimetry of pure DPP_H.

The DSC measurement reported in Fig 1.14 shows three separate features that identify three different aggregation stages. The first exothermic features at ~150°C is ascribed to the thermally activated crystallization of the DPP_H molecules in their original chemical structure (crystalline phase 1). In agreement with the thermogram reported in Fig.1.7, the endothermic feature at ~200°C is ascribed to the cleavage of the t-BOC functionality and it is immediately followed by an exothermic feature at ~210°C associated to the crystallization triggered by the activation of the hydrogen bonds in the system (crystalline phase 2). In this framework, the aforementioned behaviour of the crystallinity

observed in XRD analyses performed at different stages of the thermal treatment can be explained as follows: I) before the thermal treatment the film is smooth (see AFM images) and amorphous; II) During the first stages of the thermal treatment the first crystallization process takes place, the film roughness increases and phase segregation occurs (when in blend with PCBM). At this stage the film is in the first crystalline phase and no hydrogen bonding is present in the system; III) After the removal of the t-BOC functionality, the cohesive forces introduced by the hydrogen bonding drive the transition to the second crystalline phase which, cannot be detected by XRD analyses in Bragg-Brentano configuration as the cristallization is mostly on the film plane. As a result, the film morphology changes and the diffraction signal associated to the first crystal phase dims.

To demonstrate the presence of two crystalline phases and to investigate their properties I report GIWAXS measurements performed at different stages of the thermal treatment during the phase transition between the two crystalline structures (Fig 1.15).

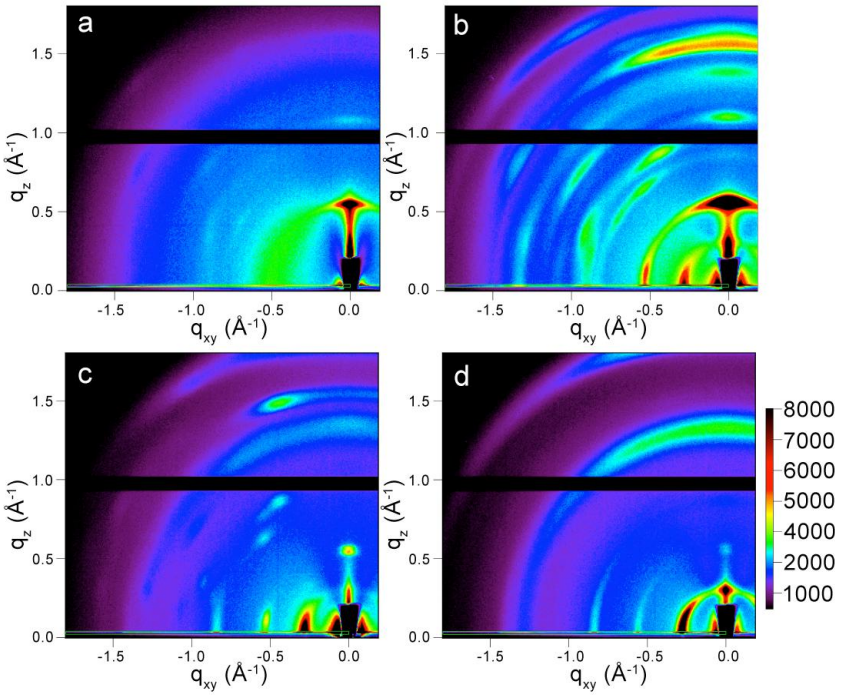

Figure 1.15 GIWAXS measurements on pure DPP_H films at different stages of thermal treatment. All the samples were pre-annealed at 150°C for 1 minute to induce the first phase transition from the amorphous state to phase 1. The following thermal treatment has been performed at 170° for: **a**) 0 min, **b**) 5min, **c**)10 min, **d**) 20 min.

The diffraction pattern reported in Fig1.15a, recorded on a sample pre-annealed at 150°C, shows a peak at q_z=0,5 Å^{-1} indicating an out-of-plane periodicity of 1.10 nm. This is the same feature observed during XRD measurements reported in Fig.1.13 which is ascribed to the first crystalline phase in which the DPP_H still preserve its original chemical structure. In panel b, I report the diffraction pattern recorded after an additional 5 minutes of thermal treatment at 170°C. Here, the diffraction peak at q_z=0,5 Å^{-1} becomes more intense due to the crystallization of the residual amorphous material and another diffraction pattern with in-plane periodicity featuring a peak at q_{xy}=0.3 Å^{-1} with a replica at q_{xy}=0,6 Å^{-1} appears. This pattern can be ascribed to the second crystalline phase observed in DSC

measurements. After 10 minutes of thermal treatment at 170° the peak ascribed to the out-of-plane periodic structure dims as the phase transition to the H-bonded crystalline phase takes place. The diffraction peak along q_{xy} grows and a second order replica appears at q_{xy}=0.9 Å^{-1}. At t_{TT}=20 minutes the film is entirely converted into crystalline phase 2 and the diffraction pattern of phase 1 is almost completely vanished. Importantly, this measurement explains the non-trivial behaviour observed in XRD. The two measurements are consistent in detecting the first crystallization from the amorphous phase to the crystalline phase 1 with out-of-plane periodicity while only GIWAXS measurements can detect the presence of phase 2 because of its in-plane periodicity that is not detectable using Bragg-Brentano geometry.

Importantly the film morphology and crystallinity are preserved for shelf times up to 6 months. As shown in Fig.1.16, the XRD pattern of a representative DPP_H:PCBM film stored in air under ambient illumination for over 6 months shows an intense diffraction peak at 2θ = 7.6° and surface morphology as a blend measured immediately after the thermal deprotection (Fig.1.16).

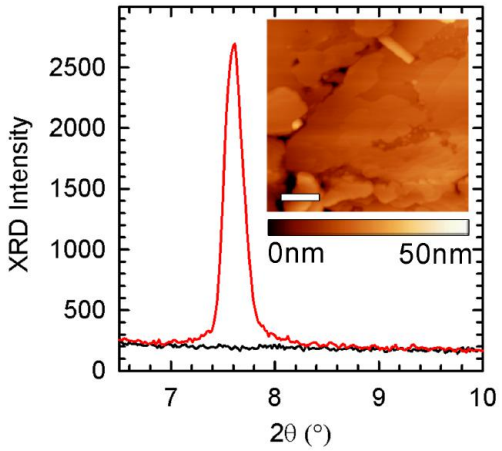

Figure 1.16 Diffraction patterns of DPP_H:PCBM (1:1 wt%) films on silica substrates at t_{TT}=270 s after a shelf time of 6 months (pristine - black line, treated for t_{TT}=270 s - red line). The inset shows the AFM surface topography of the same sample. The scale bar corresponds to 400 nm.

This further emphasises the ability of the thermally activated H-network to stabilize the blend nanoarchitecture for extended periods of time in lighting conditions at room temperature. Furthermore, as a result of the strong cohesive forces introduced by the H-bonds, the processed blend becomes essentially insoluble in common solvents (Fig.1.17), similarly to what observed with latent pigments used in inks and varnishes.[43]

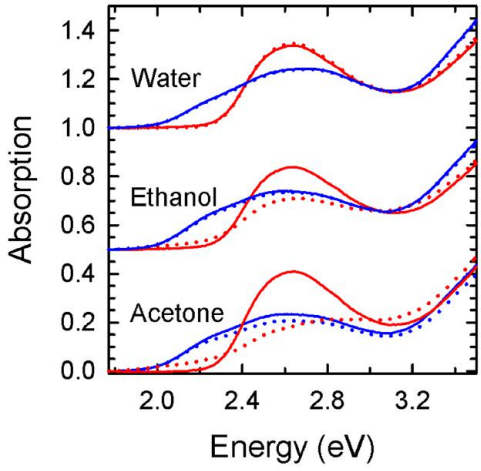

Figure 1.17 UV-Vis absorption spectra of pristine (blue) and treated (t_{TT}=270 s, red) DPP_H:PCBM films before (continuous line) and after (dotted line) washing in various solvents. The spectra of the films washed in water and ethanol have been shifted up for clarity. Deprotected blends are essentially insoluble in any of the solvents tested due to H-networking that introduces strong cohesive forces which dramatically improve the stability of the film with respect to common untreated films.

Specifically, in Fig.1.17, I report the optical absorption spectra of pristine and deprotected blends before and after washing in water, ethanol and acetone. Remarkably, while the pristine films are dissolved by ethanol and acetone, their deprotected analogues are unaffected by the washing procedure.

Organic field effect transistors

To investigate how structural changes affect the electrical properties of the material, I fabricated organic field effect transistors (OFET) in bottom gate/bottom contact configuration embedding DPP_H in the active layer and tested them at different stages of thermal treatment. The OFETSs have a channel length of 1 cm and a channel width of 10 μm.

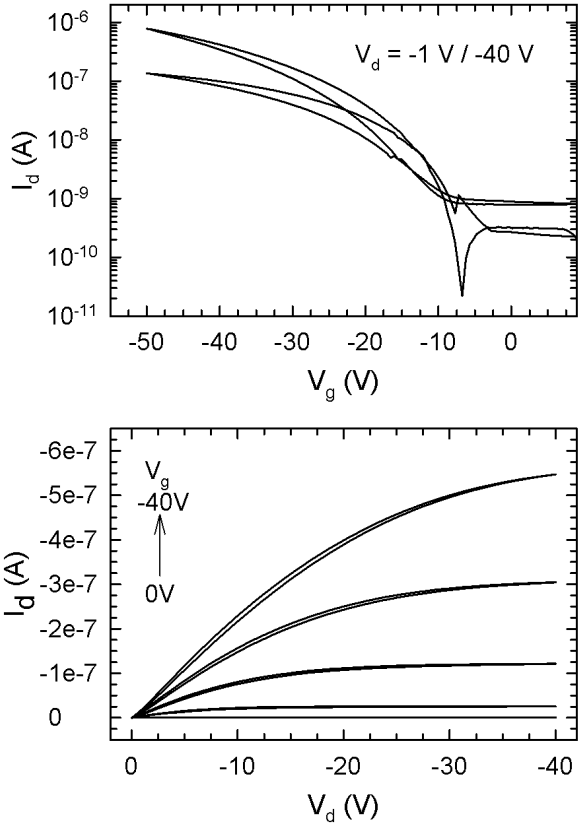

Figure 1.18 OFET characteristics of a device embedding DPP_H at t_{TT}=20min at 170°C. Transfer characteristics (upper panel) measured at V_d=-40V. Output characteristics (lower panel) measured at V_g=0V, -10V, -20V, -30V, -40V.

Representative transfer and output characteristic of an OFET embedding DPP_H at t_{tt}=20min at 170°C are reported in Fig.1.18. The transfer curves (upper panel) show a turn on voltage of -10V, a small hysteresis and an ON/OFF current ratio of $\sim 5 \bullet 10^3$. The output characteristics exhibit very small hysteresis and good linearity at low V_d due to negligible contact resistance.

In Fig.1.19, the mean saturation hole mobility (μ_{sat}) of crystalline DPP_H calculated over 5 samples for each stage is reported as a function of the thermal treatment time at 170°C. All the devices were previously annealed to so that t_{TT}=0min the material is in the first crystalline phase which exhibits an hole mobility of $10^{-6} cm^2/Vs$. OFETs embedding pristine amorphous DPP_H show no electrical response and therefore non-measurable hole mobility.

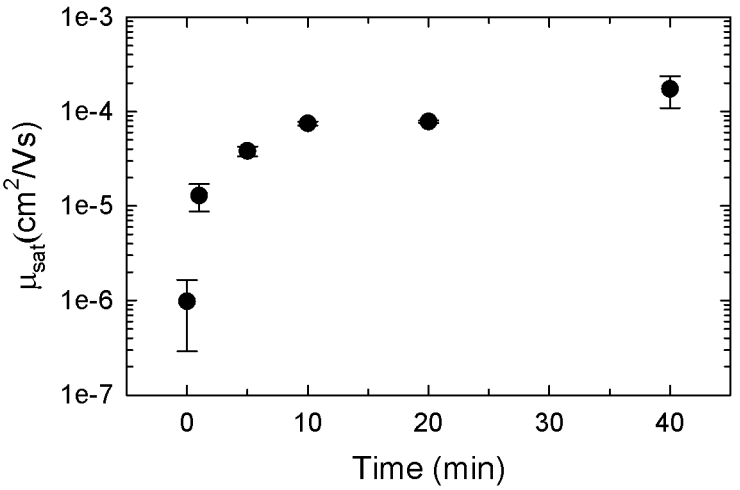

Figure 1.19 Mean saturation hole mobility of OFET embedding DPP_H at different stages of thermal treatment. The mean values are calculated over a set of 5 samples for each step. All samples were pre-annealed at 150°C for 1 minute to convert DPP_H into the first crystalline phase.

The progressive conversion into the hydrogen bonded crystalline promotes a two orders of magnitude increase of the hole mobility which reaches $\mu_{sat}=10^{-4} cm^2/Vs$ at t_{TT}=10 minutes. Longer

thermal treatments further increase the hole mobility possibly due to morphologic changes in the film structure.

Hydrogen-networked SM-BHJ solar cells

To experimentally validate the concept of post-deposition activation of latent H-bonding for improving the performances of SM-BHJ solar cells, I fabricated and tested simple proof-of-principle devices consisting of a 100 nm DPP_H:PCBM (70:30 wt) film at different stages of thermal treatment sandwiched between an ITO/PEDOT:PSS anode and a LiF/Al cathode (1.5 nm LiF, 90 nm Al).

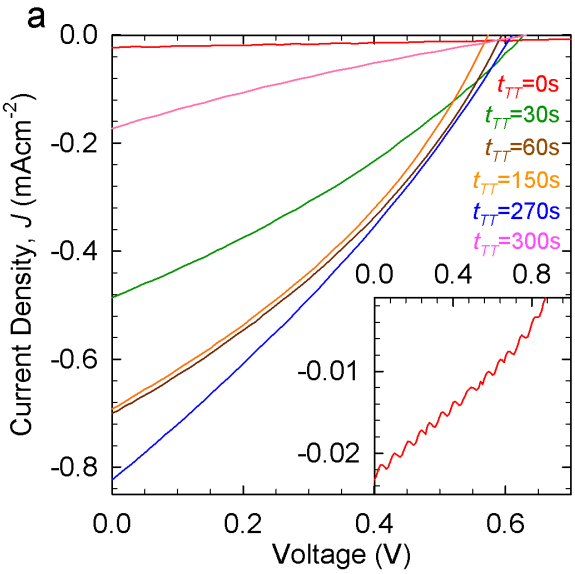

Figure 1.20 Current-voltage (IV) responses of SM-BHJ solar cells incorporating a 100 nm thick DPP_H:PCBM (70:30 wt%) film treated for t_{TT} = 0, 30, 60,150, 270, 300 s under AM 1.5G illumination (100mW/cm^2). The curve corresponding to t_{TT}=300 s is shown as dashed line to distinguish it from the positive trend in PV activity observed for shorter treatment times. Inset, zoomed-in IV response of unprocessed device.

The electrical response of the devices under AM 1.5G illumination is reported in Fig.1.20, showing negligible

dependence of the open circuit voltage (V_{OC}) on t_{TT}, a further evidence that the conjugated structure of the DPP_H core is preserved upon thermal deprotection. Remarkably, the short circuit current density (J_{SC}) shows a 30-fold increase upon annealing for t_{TT} =270 s, resulting in the concomitant growth of the power conversion efficiency (PCE) to ~0.15%, which is over 20 times larger than the efficiency of the pristine device (Fig.1.21).

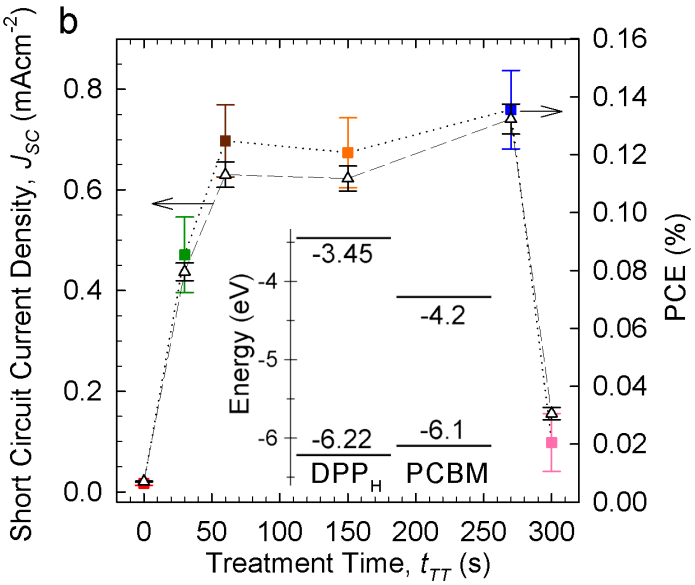

Figure 1.21 Evolution of the short circuit current density (triangles) and power conversion efficiency (PCE, squares) with t_{TT}. Schematic diagram of the energy levels of DPP_H and PCBM are reported in the inset.

The electrical characteristics of the best performing device of each set are reported in Table 2.

t_{TT} (s)	V_{OC} (V)	J_{SC} (mA cm^{-2})	η (%)	FF
0	0.88	0.0232	7.1456e-3	0.35
30	0.63	0.4860	0.0949	0.31
60	0.60	0.7003	0.1387	0.33
150	0.57	0.6920	0.1341	0.34
270	0.61	0.8232	0.1506	0.30
300	0.63	0.1729	0.0229	0.21

Table 2 Characteristics of the best performing device of each set for different thermal treatment times of the active layer. All measurements are performed under AM 1.5G illumination, 100 mW/cm^2.

The same study performed on control solar cells based on a DPP_C:PCBM (70:30 wt) blend shows that, while the pristine device has similar PCE to its DPP_H:PCBM counterpart, the device treated for t_{TT}=270s exhibits no PV activity (Table 3).

t_{TT} (s)	V_{OC} (V)	J_{SC} (mA cm^{-2})	η (%)	FF
0	0.62	0.31	0.047	0.23
0	0.61	0.28	0.042	0.23
0	0.57	0.26	0.037	0.23
0	0.53	0.27	0.036	0.24
270	0	0.032	0	--
270	0	0.028	0	--
270	0	0.023	0	--
270	0	0.023	0	--
270	0	0.023	0	--

Table 3 Characteristics of control BHJ solar cells incorporating DPP_C:PCBM blends for different t_{TT} of the active layer at 170°C. All measurements are performed under AM 1.5G illumination, 100 mW/cm^2.

This unambiguously demonstrates that the deprotection of the DPP_H molecules and the consequent H-networking plays a key role in improving the PV performances of the solar cells. I note that these proof of principle devices have not been optimized for high absolute efficiency in terms of the active layer thickness,

electrodes work functions and donor/acceptor ratio. Improved performances can potentially be achieved by tuning the DPP energy levels and optical gap, so as to better cover the solar spectrum and improve charge separation. In fact, as shown by the energy levels diagram in Fig.1.21, the highest occupied molecular orbital (HOMO) level of DPP_H is slightly lower than the HOMO of PCBM (-6.22 eV vs. -6.1 eV) which results in poor charge separation at the hetero interface. Several examples of BHJ solar cells based on DPP derivatives have been reported achieving conversion efficiencies up to 4%[49-52]. Therefore, significant improvements are expected by applying the proposed strategy to optimized molecular systems. The latent pigment strategy can also be extended to other classes of high performance pigments such as quinacridone and isoindigo[45,53]. Further optimization can also be achieved through the implementation of more complex device architectures[12,54].

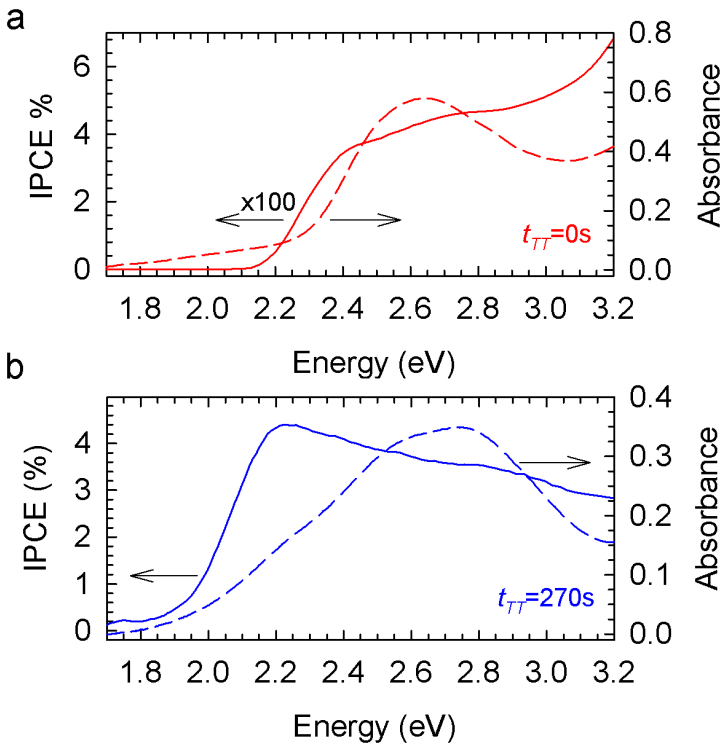

Figure 1.22 Absorption spectrum (dashed line) and IPCE (continous line) spectra for **a)** a SM-BHJ solar cell incorporating a pristine DPP_H:PCBM (70:30 wt%) film (red) and **b)** the same blend treated for 270s (blue lines).

To gather a deeper insight into the role of the molecular aggregates in deprotected crystalline films on the production of photocurrent, I measured the spectrally resolved incident photon-to-current efficiency (IPCE) of the same solar cells as in Fig.1.20 and 1.21. In Fig.1.22 I report the optical absorption and the IPCE spectrum of a pristine device and of a cell treated for t_{TT}=270 s. As expected, the IPCE spectrum of the "protected" device resembles well its absorption spectrum with no evident contribution of intramolecular aggregates at 2.2 eV. On the other hand, the IPCE spectrum of the "deprotected" cell shows a marked band at 2.2 eV that is significantly more intense than the corresponding optical absorbance, indicating that intermolecular

aggregates more efficiently convert absorbed light into photocurrent with respect to isolated molecules.

Photophysical investigation of thermally induced H-Networking

Finally, I use time-resolved photoluminescence experiments to probe the phase separation on a molecular scale and thereby to unravel the photophysical processes underpinning the improved efficiency in H-networked SM-BHJ solar cells. Figures 1.23 shows the time-integrated PL spectra and the PL decay curves of a DPP_H:PCBM blend at increasing t_{TT}.

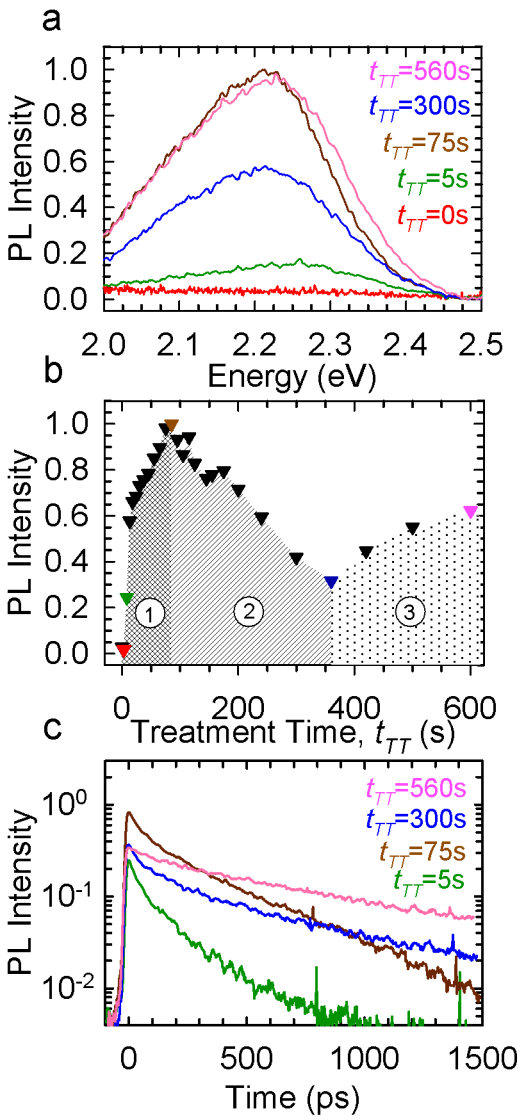

Figure 1.23 **a**) PL spectra, **b**) integrated PL intensity and **c**) PL decays of a DPP_H:PCBM (1:1 wt%) film for different treatment time. The same colour code applies throughout panels 'a' to 'c'.

The corresponding contour plot of PL decay traces vs t_{TT} is reported in Fig.1.24.

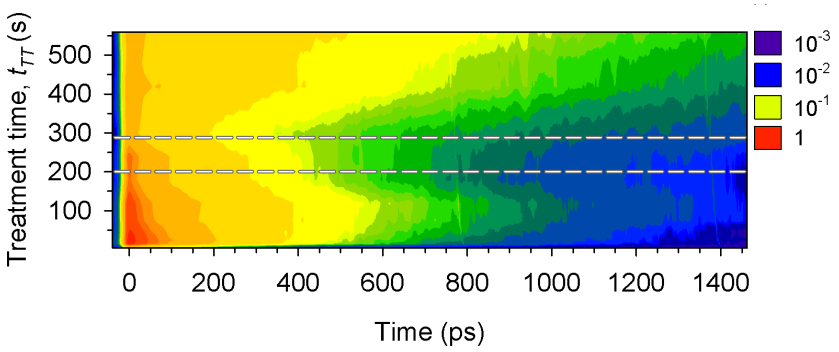

Figure 1.24 Contour plot of the PL decays as a function of t_{TT} (logarithmic scale). The dashed lines highlight the region corresponding to the highest exciton mobility.

In the as-spun DPP_H:PCBM blend, donor and acceptor molecules are finely mixed and the recombination of DPP_H excitons is dominated by ultrafast electron transfer to PCBM. Accordingly, the film is completely non-emitting. Brief thermal treatments lead to the formation of crystalline phase-segregated domains rich in DPP_H in its first crystalline phase and PCBM. In this film morphology, due to the low carrier mobility of the first crystalline phase, DPP_H excitons are photogenerated sufficiently far from PCBM to be able to recombine radiatively before reaching the domain interfaces where they are split by ultrafast electron transfer. As the domain size grows, the film becomes progressively more emissive (zone '1' in Fig.1.23b) and the PL decay curve shows the typical stretched exponential behaviour that reflects the distribution of distances between the photoexcitation spot and the quenching site (i.e. the DPP_H/PCBM interface) characteristic of the diffusion limited recombination regime (Fig.1.23c).[32,55] The progressive conversion into the second crystalline phase, enhances the exciton mobility in the DPP_H-rich domains leading to faster exciton diffusion and consequent quenching of the PL by electron transfer to PCBM or by nonradiative decay in defect sites (zone '2' in Fig.1.23b). Fast migration to the donor-acceptor interfaces and consequent shorter PL lifetime in films subject to treatments between 200 s and 300 s is confirmed by both the

more pronounced fast PL decay component in Fig.1.23c and by the accumulation of isolines in the contour plot in Fig.1.24. Finally, longer thermal treatments further increase the domain size and leads to the slow recover of the emission yield (zone '3' in Fig.1.23b). As a result, the interface exciton splitting becomes progressively weaker and the decay kinetics becomes single exponential with lifetime ~800 ps, indicating that the dominant decay process is now the radiative recombination of excitons in the large DPP_H-rich domains.

Diffraction limited photo-lithography

Finally, to show the great potential of the latent hydrogen bonding strategy, I demonstrate a very simple maskless lithography technique to obtain nanometric crystalline semiconducting features on non-conductive amorphous DPP_H films. This approach consists in conveying thermal energy on a localized area of a DPP_H thin film to locally induce the hydrogen-bonding-triggered crystallization. With this aim, I focalized a 405 nm laser into a confocal microscope and used the objective as a "brush" to draw sub-micrometric semiconductive features on the film surface (Fig.1.25). This process leads to the formation of very stable crystalline domains whose mobility is dramatically higher than the amorphous surroundings.

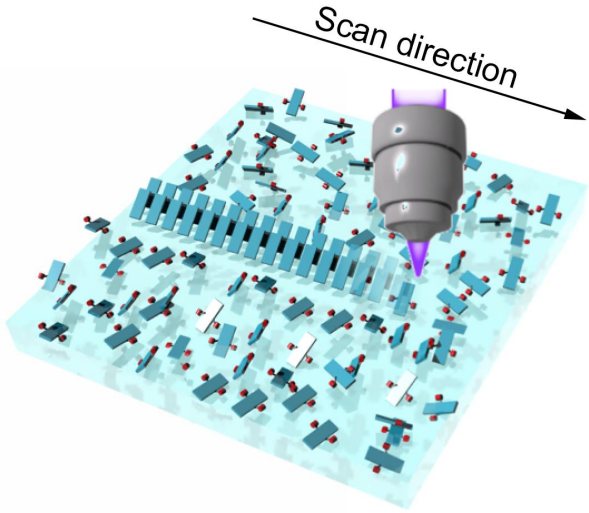

Figure 1.25 Schematic representation of the lithographic technique. A focalized laser radiation is swept on a amorphous DPP_H film to locally induce the formation of hydrogen networked crystalline domains.

To do so, I draw a series of 20 μm x 20 μm matrix of 1024 x 1024 individually exposed pixels using increasing laser fluence and pixel exposure time necessary for achieving various degrees of hydrogen-bonding networking.

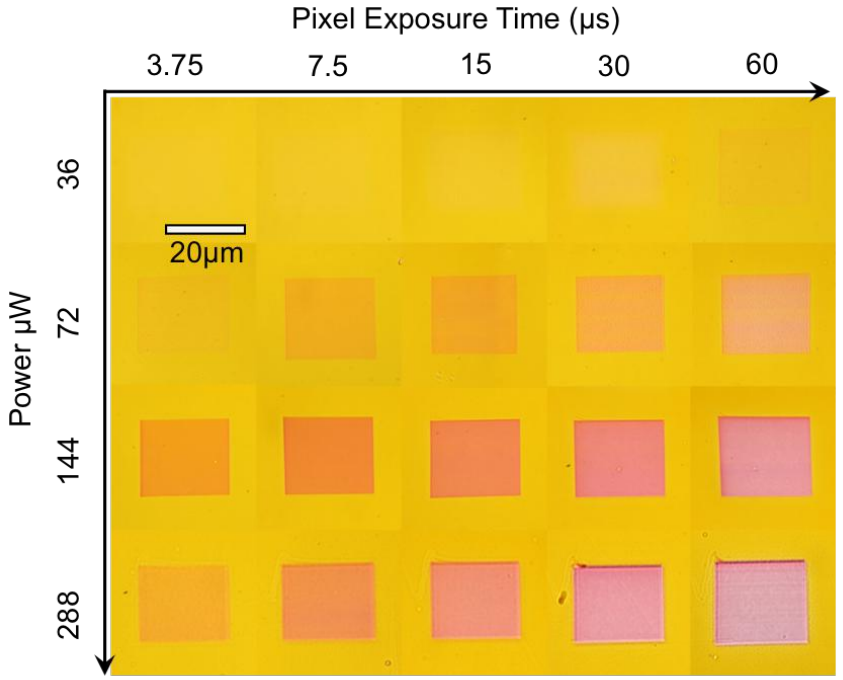

Figure 1.26 Optical microscope images of a set of 20 µm x 20 µm crystalline DPP_H areas surrounded by amorphous materials. Each square is made of 1024x1024 pixels and has been impressed with different power of the laser and pixel exposure time.

This set of images (Fig.1.26) shows the progressive conversion of the PDD_H film from amorphous to completely converted crystalline domains. To quantify this evidence, I performed in-situ absorption spectroscopy on each square by using the same confocal setup I used to draw the features.

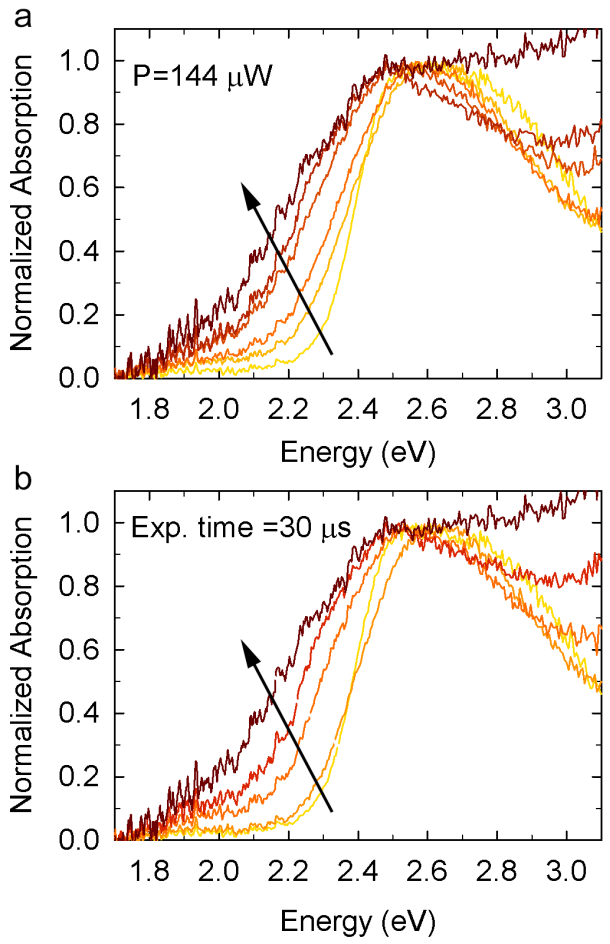

Figure 1.27 In situ optical absorption spectroscopy performed on the square features reported in Fig.1.26 at constant laser power (**a** – P=144 μW and constant pixel exposure time (**b** - t=30 μs)

The data show the progressive growth of the charactheristic absorption band of the aggregate at 2.2 eV at increasing laser power and exposure time.

The lateral resolution of these structures is 370 nm measured as the full width at half maximum of the first derivative of the colour profile extracted by a software.

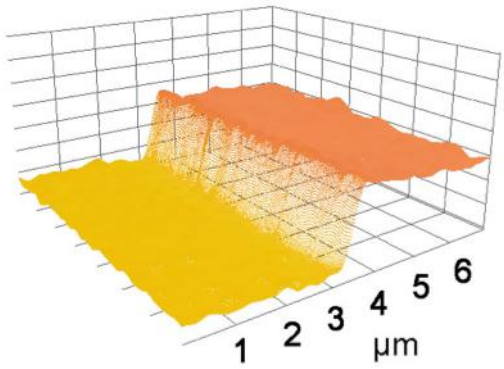

Figure 1.28 Colour profile of the edge of a square feature. The vertical axis represents the colour coordinates. The lateral resolution is 370 nm.

To test the resolution limit of this lithographic technique, I draw a set of lines only 1 pixel wide at constant laser power and different exposure times.

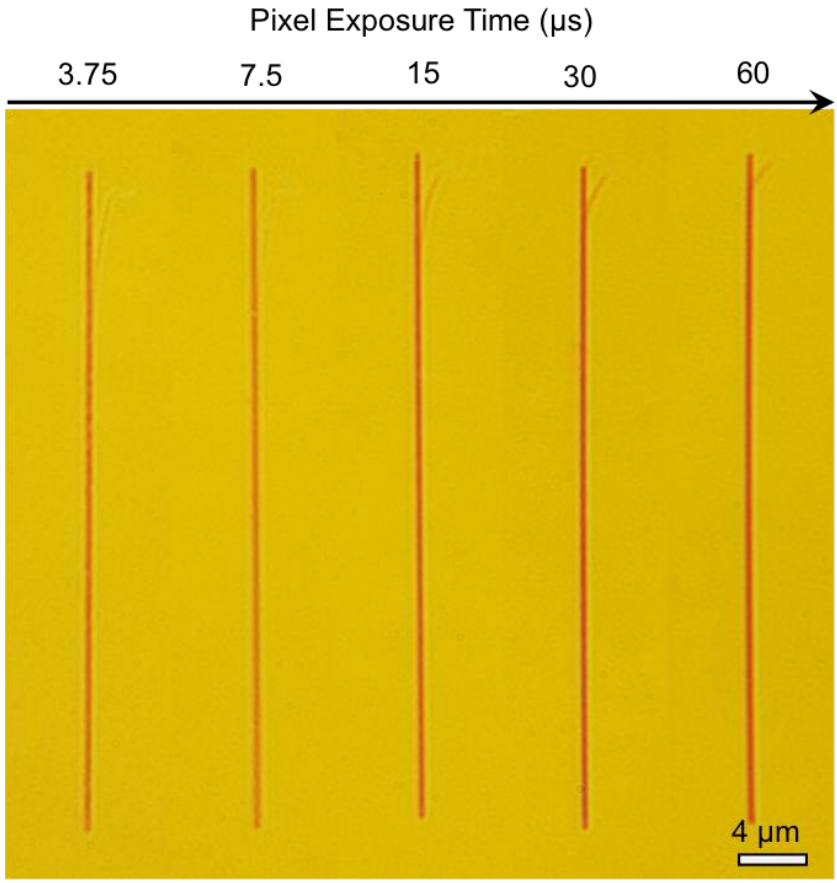

Figure 1.29 DPP_H converted features on an amorphous film. Each line is 1024 pixel long and 1 pixel wide. All line have been impressed with with the same laser power (P=144µW) and different pixel exposure time.

The highest resolution achieved is 265 nm. This value is below the the diffraction limit of 350 nm calculated as the diameter of the first Airy disk according to the formula

$$D = \frac{1.22 \cdot \lambda}{NA}$$

where λ is the excitation wavelength and NA is the numeric aperture of the optical system.

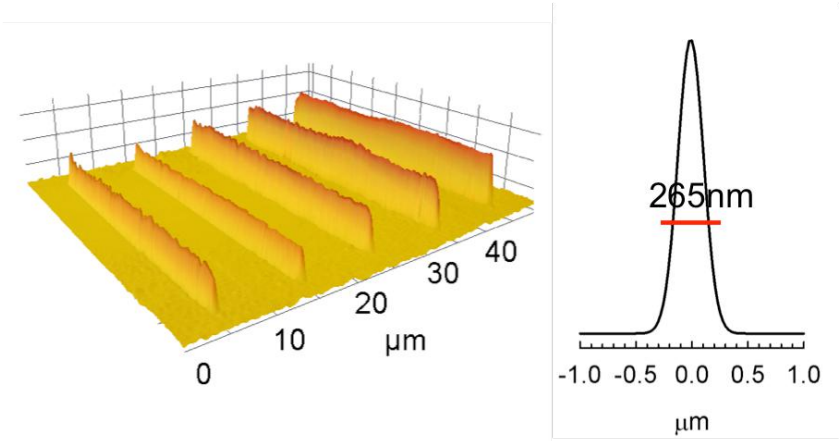

Figure 1.30 Colour profile of the same picture reported in Fig.1.29. The vertical axis represents the colour coordinates (left panel). The narrowest profile (right panel), calculated by mediating the line width on the entire length, has a full width at half maximum of 265 nm.

1.2.3 Methods

Synthesis of DPP_H

In an Ar filled glove box, a suspension of 1 (1.000 g, 2.270 mmol) and DMAP (693 mg, 5.672 mmol) in anhydrous THF (20 ml) is prepared and stirred at room temperature for 15 minutes. A solution of di-tert-butyl dicarbonate (2.480 g, 11.36 mmol) in THF (8 ml) is added and the mixture is stirred at room temperature for 46h. A yellow suspension is obtained. Light petroleum ether (30 ml) is added and the mixture is stirred for 30 minutes and filtered obtaining a yellow solid. Product is dissolved in CH_2Cl_2 and filtered through a short silica plug. Solvent is evaporated under reduced pressure obtaining pure product as a yellow solid (1.186 g, 1.948 mmol, yield 85.8 %). Characterizations are in agreement with those previously reported [56].

Electrochemical Analysis

20 mg of t-BOC protected DPP_H were dispersed in 1 ml of CH_2Cl_2. The suspension was filtered to obtain a saturated solution and casted on the top of a well polished glassy carbon tip working electrode (surface area 0.071 cm^2). A thin molecular film of DDP_H was then obtained by solvent evaporation at room temperature and thermal treatment (20 min at 170°C). The glassy carbon supported film was characterized by Differential Pulsed Voltammetry in tetrabutylammonium perchlorate 10^{-1} M in anhydrous acetonitrile at 20 mV/s. The counter, and pseudoreference electrodes were a Pt flag and a Ag/AgCl wire, respectively. The Ag/AgCl pseudoreference electrode was externally calibrated by adding ferrocene (10^{-3} M) to the electrolyte ($E_{1/2}$=0.39 V, ΔE=62 mV). Measurements were carried out in a glove box filled with argon ([O2]<1 ppm). LUMO energies was calculated by the DPV peak potential value considering the Fc vacuum level at -5.23 eV.

Structural and morphological analyses

X-ray diffraction specular scans on single crystals and films were performed with a PANalytical X'Pert Pro powder diffractometer with Cu Kα radiation. AFM images were obtained with a Nanoscope V MultiMode atomic force microscope (Veeco) using single-beam silicon cantilevers (force constant of 40 N/m) operating in intermittent contact (tapping) mode. Image analysis was performed with the program WSXM.

Differential scanning calorimetry

DSC measurements were conducted under N2 atmosphere at a scan rate of 20 °C/min using a Mettler Toledo STARe system. Standard Mettler Aluminum crucibles were utilised, for this purpose employing samples of ~3 mg in weight.

OFET fabrication

For the preparation of the OFETs, interdigitated substrates (Fraunhofer institute) were sonicated for 10 minutes in acetone and for 30 minutes in isopropanole. A self assembled monolayer of octadecyltrichlorosilane (OTS) was grown in a glovebox. A 5mg/ml solution of DPP_H in chloroform was wire-bar coated on the substrate to obtain a homogenous film ~30nm thick.

Solar cells fabrication and characterization

For the preparation of solar cells, indium tin oxide (ITO)-coated glass substrates were sonicated for 10 minutes in isopropanole and treated in a nitrogen plasma chamber for 10 minutes. A layer of poly(3,4-ethylene dioxythiophene/poly (styrene - sulfonate) (PEDOT:PSS, CleviosP VP.AI 4083) was spin coated from aqueous solution. The film was annealed under nitrogen atmosphere at 150°C for 15 minutes. Profilometric measurements of the PEDOT:PSS layer reported a thickness of 40 nm. A 20 mg/ml chloroform solution of DPP and [60]PCBM

(Solenne B.V., The Netherlands) 70:30 wt. was stirred overnight and then filtered through a 0.22 μm poly (tetrafluoroethylene) PTFE filters. The solution was spin coated on the ITO PEDOT:PSS substrates at 1500 rpm for 60 s which yielded a film ~100 nm thick. A lithium fluoride layer (1.5 nm) coated with aluminium (100 nm) was thermally evaporated using a shadow mask.

Current versus voltage curves (I-V) characteristics were measured with a Keithley 2602 Digital Source Meter. The cells were illuminated from the glass side with a 100 mW/cm^2 ABET Technologies Sun 2000 Solar Simulator. Spectrally resolved incident photon-to-current efficiency (IPCE) was recorded by illuminating the solar cells with calibrated monochromatic light from a Xe lamp coupled to a monochromator. All fabrications and characterizations were performed under nitrogen.

Spectroscopic studies

Spectroscopic measurements were performed on diluted chloroform solution and spin coated films on silica substrates. IR spectroscopy was performed with a μ-FTIR Nicolet iN 10. Absorption spectra were collected with a Varian Cary 50 spectrophotometer. Time-resolved PL measurements were carried out using 410 nm (3.02 eV) excitation from a doubled Ti:Sapphire laser (Coherent Mira 900), and detecting the emitted light with an Hamamatsu C4742-95 streak camera.

1.3 Conclusions

In conclusion I demonstrated a novel approach to fine control the phase segregation of solution processed SM-BHJ solar cells based on the exploitation of latent H-bonding via thermal deprotection of electron donor DPP derivatives blended with PCBM. As shown by AFM and XRD analyses, the thermally induced H-networking of the DPP molecules provides the necessary driving force for the formation of interpenetrated crystalline domains rich in donor and acceptor moieties, resulting in over 20-fold increase of the PV efficiency. The improvement of the PV performances in the SM-BHJ solar cells is due to a larger short-circuit current resulting from the higher carrier mobility in the crystalline aggregates of deprotected DPP molecules. The demonstrated approach to controlled post-deposition phase segregation in SM-BHJ solar cells, demonstrated here for DPP derivatives blended with PCBM, could be extended to smaller band gap molecular semiconductors for achieving a better match with the spectrum of solar radiation and thereby strongly boost the PV efficiency of small-molecule solar cells.

2 Sensing of Photoinduced Charge Separation at the P3HT/Water Interface

Hybrid devices employing organic semiconductors interfaced with an aqueous solution represent a new frontier in bioelectronics and energy applications. Understanding of the energetics and photo-induced processes occurring at the organic-water interface is fundamental for further progress. In this work, I locally probe the interfacial charge states by means of ratiometric optical sensors based on engineered colloidal heterostructures exhibiting good sensibitlity for electron withdrawing/donor agents. The aqueous solution is found to polarize the polymer outermost layers, which together with the polymer p-(photo)doping by dissolved oxygen, localizes photogenerated electrons at the P3HT/water interface, while holes can be transferred to the ITO electrode. Under illumination, the polymer/water interface is negatively charged, attracting positive ions from the electrolyte solution and perturbing the ion distribution in the aqueous solution. The observed capacitive mechanism is of general character and could underlie the behavior of a variety of devices characterized by an organic/water interface, such as prosthetic devices for artificial vision and photoelectrochemical hydrogen producing systems.

2.1 Introduction

A number of organics-based applications ranging from photoelectrochemical water splitting devices,[57-61] to electrolyte-gated field effect transistors,[62,63] and bioelectronics[64-70] have been developed taking inspiration from the prototypical organic solar cell architecture, Scheme 2.1a. These devices share the use of liquid electrolytes at the interface with a photoactive polymer, Scheme 2.1b, typically P3HT. A fascinating application of organic optoelectronics is light-induced neural stimulation, a forerunner of the artificial retinal prosthesis for visual restoration.[66-69] The corresponding devices have a typically simple structure, consisting of an Indium Tin Oxide (ITO) substrate, an organic photoactive layer (P3HT or a P3HT/fullerene blend) and an aqueous electrolytic solution, in which the neuronal cells can grow and live, Scheme 1b. It has been recently demonstrated that such devices can promote neuronal stimulation under pulsed light illumination,[68] possibly in relation to a capacitive coupling at the polymer/electrolyte interface driving the neuronal signaling mechanism. The actual mechanism behind cell stimulation *in vitro* and *in vivo* is still far from being understood, with alternative mechanisms, such as thermal excitation,[71] Faraday currents, or specific photochemical reactions, still under investigation. A full understanding of the photo-electrochemical processes taking place at the organic/electrolyte interface is a crucial step to optimize all related devices. Limited work has been carried out on the characterization of the P3HT/water interface, in view of understanding the operating principles of organic-based water splitting devices.[57,61] Interfacial acid-base reactions at the P3HT surface have been proposed to drive photogenerated electrons from the bulk of the polymer to the surface, where the reaction occurs.[58] Beyond these studies, mainstream research was devoted to the investigation of the role of water impurities on the

degradation of the organic layer, to test and improve the device temporal stability.[72-74]

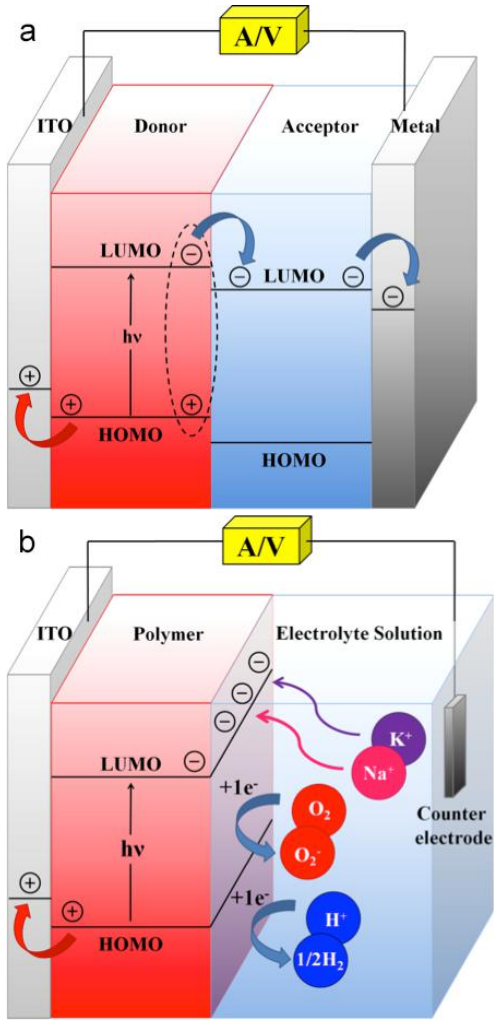

Figure 2.1 **a**) Schematics of an organic solar cell, with main photoinduced electron/hole (e^-/h^+) transfer pathways. The device consists of a transparent electrode, typically a conducting indium-tin oxide (ITO) substrate; the photoactive layer, typically a donor (polymer or small molecule)/acceptor (fullerene derivative) heterojunction, responsible for charge generation and transport; and a metal counter-electrode. **b**) Hybrid organic/aqueous electrolyte devices, highlighting the (e^-/h^+) pathways upon illumination and the possible interfacial reactions.

2.2 Results

In order to locally probe the charge state of the polymer surface in direct contact with water, I carried out specific experiments exploiting the ratiometric sensing ability of so-called dot-in-bulk (DiB) nanocrystals (NCs) (Fig.2.2). These systems consist of a small CdSe core (3 nm diameter) over coated with an ultra-thick shell CdS leading to a total diameter of ~20 nm.

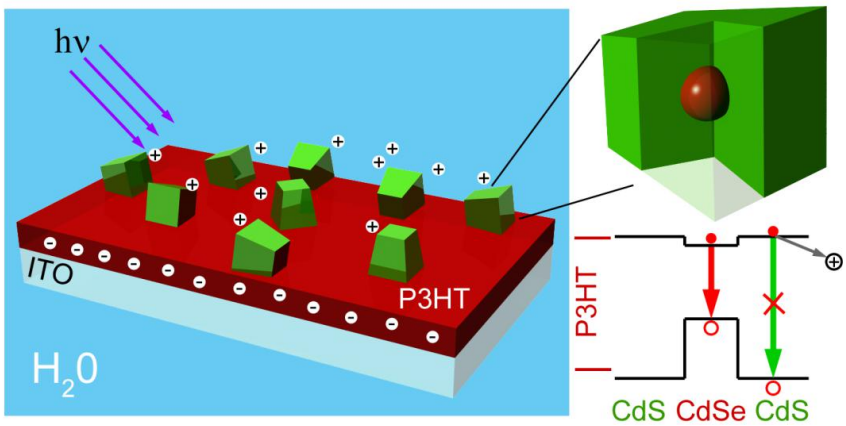

Figure 2.2 Schematic representation of DiB-NCs deposited on ITO/P3HT substrate immersed in water. Under UV illumination, negative polarization of the P3HT surface leads to local acidification of the NC environment. On the right hand side a CdSe/CdS DiB-NC is depicted together with the characteristic energy diagram and the frontier levels of P3HT in dry conditions (dark red lines). Trapping of photogenerated shell electrons leads to selective quenching of the shell luminescence while the core emission is unaffected.

As a result of the polytypic crystal structure of the CdS shell and the electrostatic repulsion between core and shell holes, upon photoexcitation DiB-NCs support two types of excitons. [75,76] Core-excitons emit in the red spectral region and are tightly confined in the center of the NC, which makes them essentially insensible to the NC environment and to surface states. Shell

excitons, on the other hand, are green-emitting Coulombically bound states that can sample the NC surfaces and are therefore strongly affected by surface charges and by the NC chemical surroundings. This property has been recently exploited in ratiometric sensing experiments where the core photoluminescence (PL) acted as the internal reference for the surface sensitive shell emission, Figure 2.2. [77]

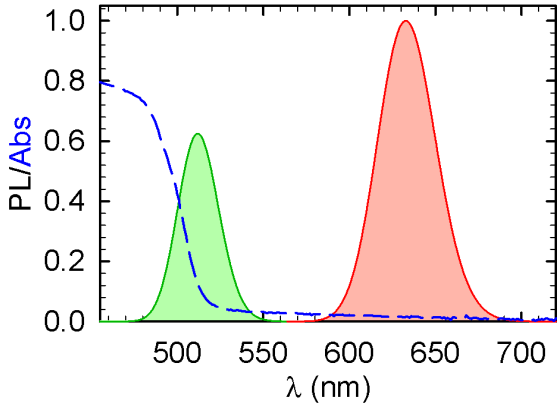

Figure 2.3 Absorption and photoluminescence spectra of DiB-NCs (core radius 1.5 nm, shell thickness 5.8 nm) showing the characteristic two-color emission under cw excitation (excitation wavelength 400 nm) due to radiative recombination of core (650 nm) and shell (510 nm) excitons.

A representative PL spectrum of DiB-NCs on glass is shown in Fig.2.3. Importantly, in these systems, quenching of the shell PL is due exclusively to nonradiative transfer of photogenerated shell electrons, while the few picoseconds residence time of photogenerated holes in the shell makes them unaffected by surface states and chemical agents. As a result, DiB-NCs are particularly suitable for ratiometric detection of electron withdrawing agents and to optically probe the acidity of the NC environment. [77] In these experiments, I deposited DiB-NCs on the P3HT polymer film and checked the stability of both the green and red PL in air. The stability of both emissions has been further confirmed depositing the NCs on glass and collecting the PL spectra over time both in air and water; no quenching is observed in either condition, Figure 2.4.

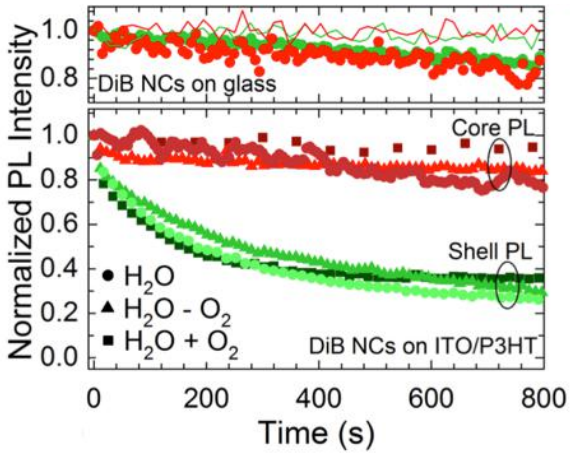

Figure 2.4 Upper panel) Core (red) and shell (green) emission intensity as a function of the excitation time for DiB-NCs deposited on glass in dry conditions (lines) and immersed in water (circles). Lower panel) Time evolution of the core (red tones) and shell (green tones) emission intensity for DiB-NCs on ITO/P3HT immersed into water (circles), deoxygenated water and oxygen-enriched water (the water is deionized in all cases). In all conditions, the core emission is constant over time while the shell luminescence drops to ca. 30% in 500 s due to progressive formation of electron poor environment.

The shell/core PL ratio of the NCs on the dry P3HT film is slightly lower than for DiB-NCs on glass, which accounts for the initial mild electron withdrawing effect of P3HT, in agreement with the alignment of the frontier levels of the polymer and the NCs in dry conditions, Figure 2.2. Upon adding water in the absence of photoexcitation, the polarization of the frontier states of the outermost P3HT layer enhances electron transfer from the DiB-NCs to the polymer, leading to an initial dimming of the shell PL whilst the core emission remains constant. Although already indicative of enhanced electron harvesting ability of the polarized polymer in water, this process is superimposed to another dramatic effect. Specifically, in time and under UV photoexcitation, the shell PL undergoes a progressive decay ultimately reaching ~30% of its initial value. Concomitantly, the core PL intensity remains constant thereby further confirming the photochemical stability of the NCs during the experiment. The dramatic drop of the shell PL points to the gradual formation

of an electron accepting (or depleted) NC environment under illumination. Since one possible origin of this effect could be the gradual evolution of radical oxygen close to the film surfaces efficiently scavenging photogenerated NC electrons, I repeated the sensing experiments in identical excitation conditions but changing the oxygen concentration of the deionized water solution. As shown in Figure 2.4, the ratiometric response of the DiB-NCs in the three experimental configurations is essentially identical, which rules out oxygen as major player, although it might still affect the speed of the reaction. Most importantly, the whole body of ratiometric sensing analysis supports the picture of progressive acidification of the solution in close proximity to the P3HT film under illumination due to accumulation of bulk electrons on the polymer surface progressively charge balanced by the formation of an electron poor (acidic) layer of polarized water molecules.

2.3 Conclusions

In conclusion, I exploited the ratiometric sensing abilities of DiB-NCs to detect the polarization driven accumulation of positive charges at the P3HT/water interface. Under UV irradiation, the surface of P3HT is negatively charged, therefore, perturbating the ions distribution in the water solution by attracting positive ions to the proximity of the polymer surface. The understanding of the processes occurring at the P3HT/water interface is of fundamental interest in developing biocompatible optoelectronic devices such as retinal prostheses and organic systems for photochemical applications. Moreover, this study shows the great potential of DiB-NCs as single particle ratiometric sensor for Coulombically interacting species.

3 Two-color emitting colloidal nanocrystals as single particle ratiometric probes of intracellular pH

Intracellular pH is a key parameter in many biological mechanisms and cell metabolism. This parameter has been frequently used to detect and monitor cancer formation and brain or heart diseases. pH sensing is typically performed by fluorescence microscopy using pH responsive luminescent dyes. The accuracy of this method, however, is limited by the need for quantifying the absolute emission intensity of dye molecules in living biological samples. An alternative approach with a potentially much higher sensitivity and precision is based on probes with a ratiometric response arising from the different pH sensitivity of two emission channels of a single emitter. Current ratiometric probes are typically complex constructs consisting of inorganic nanostructures coupled to organic dyes, which suffer from poor photochemical stability and cross-readout due to the broad linewidth of their emission spectra. In this thesis, I demonstrate that such limitations can be alleviated using a single-particle ratiometric pH probe based on fully inorganic dot-in-bulk CdSe/CdS nanocrystals (NCs). These nanostructures feature emission spectra comprising of two fully spectrally separated, narrow peaks with markedly different pH sensitivity. These two emissions arise from radiative recombination of core- and shell-localized excitons, that are characterized by markedly different responses to the NC environment including the pH level. Specifically, the core emission is much less affected by the pH than the shell luminescence which undergoes drastic enhancement in the 3-11 pH range, resulting in a cross-readout-free ratiometric response as strong as 600%. In vitro microscopy

of Human Embryonic Kidney cells demonstrates that the ratiometric response in biologic media closely resembles the pre-calibration curve obtained through far-field titration experiments. The NCs show good bio-compatibility, enabling to monitor in real-time the externally induced pH variations in living cells.

3.1 Introduction

Intracellular pH plays a fundamental role in the regulation of the cell metabolism and in a large number of biological mechanisms, such as glycolysis and hydrolysis of adenosine triphosphate (ATP), protein folding and enzyme activity.[78-81] Alterations of intracellular pH are also typically indicative of cancer [82-86] or major brain and heart diseases.[87-90] Sensing intracellular pH is, therefore, a key diagnostic tool in biological and medical sciences. Conventional intracellular fluorescent pH probes are organic fluorophores, whose luminescence is quenched in acidic or basic conditions, thus allowing monitoring the cellular pH. The most common organic dyes for pH sensing are fluorescines, cyanine derivatives[91-93] and, more recently, naphthalimide derivatives that feature multiple sites for target-specific functionalization.[94,95] Colloidal semiconductor nanocrystals (NCs)[96,97] and metal nanoclusters with biocompatible capping ligands[98] have been recently proposed as potential alternative materials for intracellular pH sensing,[99-102] as they combine high emission efficiency and size-tunable electronic properties with enhanced stability and exceptionally large surface-to-volume ratios. In addition, NCs feature broad, virtually continuous absorption spectra that allows for non-resonant excitation, which lowers the detection limit and boosts the contrast and the resolution of confocal microscopy by minimizing detrimental background signals due to the diffuse stray-light and the auto-fluorescence of organic tissues.[103-108] The biocompatibility of intracellular pH probes and their selectivity for specific cytoplasmic organelles can be further enhanced by using polymeric or silica nanoparticles as vehicles for their targeted internalization through the cellular membrane.[109-114]

A common experimental difficulty of radiometric luminescence pH sensing is that it requires the accurate quantitative estimation of the emission intensity in biological systems, which is typically strongly dependent on the concentration of fluorophores inside

the cells and requires the use of fluorescent standards, such as rhodamines, to correct for the experimental conditions.[115] This is boosting the interest for ratiometric systems capable of reporting pH variation through the intensity ratio between two coexisting emissions with different pH sensitivity.[116-119] To date, ratiometric pH sensors are mostly based on metallic or semiconducting nanoparticles coupled to organic dyes, whose mutual photophysical interaction through charge- or energy-transfer is determined by the external environment, leading to pH-induced spectral variations.[120-124] Despite the variety of proposed architectures, all ratiometric sensors available to date comprise of at least one organic component,[125-127] which typically suffer from low photostability. In addition to this, a common limitation of ratiometric pH sensors is the strong cross-readout due to the spectral overlap between the broad luminescence profiles of the two emitting species.[115]

In this work, I show the use of intrinsically ratiometric two-colour emitting inorganic heterostructures as single-particle intracellular pH sensors, combining many important advantages over conventional pH probes. Namely, these systems are intrinsically ratiometric, which eliminates the need for supramolecular constructs and for accurate control of secondary interactions and lifts the ubiquitous concentration-dependence of the response signal of radiometric pH probes. Equally importantly, these compact ratiometric nanostructures exhibit widely separated narrow-line emission bands, which completely suppresses cross-readout errors.

CdSe/CdS Dot-in-Bulk Nanocrystals

In this work, I use so-called dot-in-bulk CdSe/CdS NCs (DiB-NCs)[75-77,128] consisting of a small quantum confined CdSe core (radius ~1.5 nm) embedded in a bulk-like CdS particle (thickness ~8.5 nm). In Fig.3.1a and Fig.3.1b are reported transmission electron microscopy images of CdSe/CdS NCs during the synthesis at different shell thickness (3.5 nm and 8.5

nm respectively). Diffraction pattern collected at different reaction time show that the CdS shell grows in the same zincblende structure of the core for a few layers and then rearranges to the more thermodynamically stable wurtzite structure (Fig.3.1c).

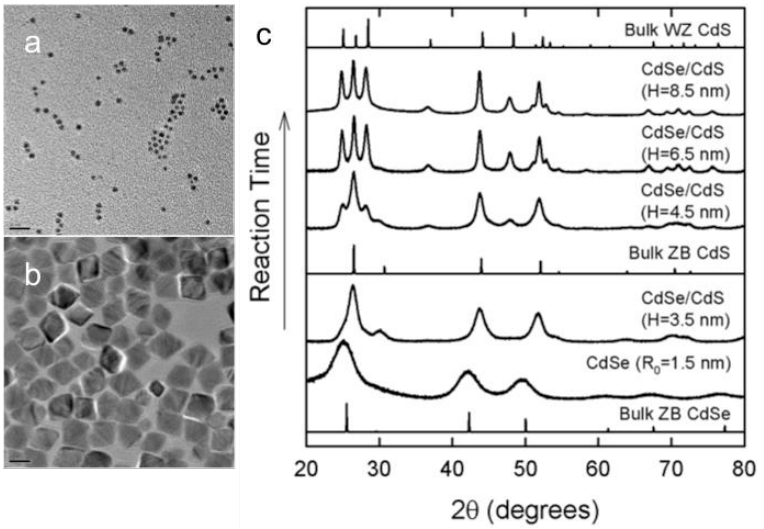

Figure 3.1 Transmission electron microscopy images of CdSe/CdS NCs with core radius R_0 = 1.5 nm and different shell thicknesses (3.5 nm (**a**) and 8.5 nm (**b**)). Scale bars in the main panels correspond to 20 nm. (c) X-ray diffraction (XRD) patterns of NCs with a core radius of 1.5 nm and different thicknesses (H = 0, 3.5, 4.5, 6.5, and 8.5 nm) in comparison to the XRD spectra of bulk CdSe and CdS.

As a result of their unique internal structure, featuring a sharp, unalloyed, core/shell interface[128] and a 30 meV potential barrier between the core and the shell valence bands[76] (Fig.3.2), DiB-NCs exhibit two-color red and green emission respectively from core- and shell excitons under low fluence optical excitation (Fig.3.3) or electrical drive.[75,76]

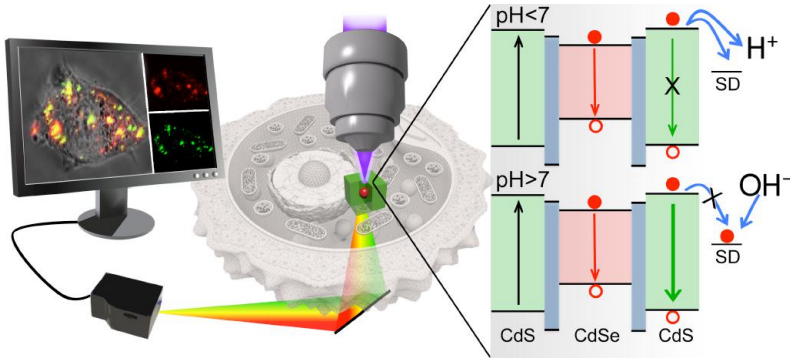

Figure 3.2 Schematic depiction of the use of two-color emitting DiB-NCs for intracellular pH ratiometric imaging, showing the simultaneous generation of two luminescence maps for the core and the shell emissions using the red and green detector channels of a confocal fluorescence microscope, respectively. The schematic representation of the band diagram of CdSe/CdS DiB-NCs and the pH sensing mechanism are shown in the right panel. At pH<7, excess H^+ ions quench the shell luminescence by directly removing electrons from the NC conduction band and by depleting (activating) electron accepting surface defects (SD). At pH>7, excess OH^- species passivate surface electron traps promoting the radiative recombination of excitons.

Two-color light as a result of radiative recombination of excitons localized in different compositional domains of the same heterostructure has been observed also in elongated dot-in-rod structures, tetrapods[129-132] and spherical core/shell systems[133-138].

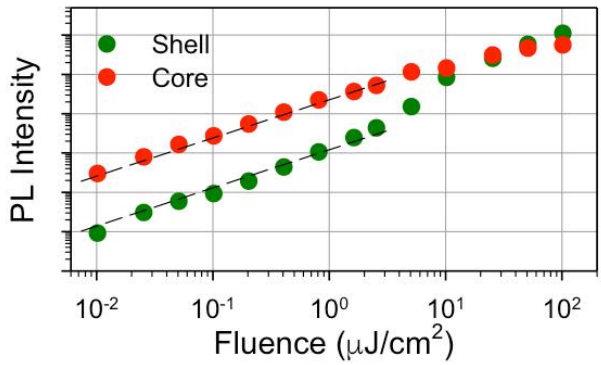

Figure 3.3 Integrated PL intensity of core (red dots) and shell (green dots) emissions as a function of increasing pulsed excitation fluence, plotted on a log-log scale. The data show a linear dependence of both core and shell emission from the excitation fluence except in the range 4-10 μJ/cm^2 due to the Coulomb-blockade.

Representative photoluminescence (PL) spectra of DiB-NCs are reported in Fig.3.4, showing the characteristic red and green emissions at 510 nm and 635 nm respectively. Fundamentally for ratiometric pH sensing, the core and shell excitons in DiB-NCs are differently exposed to the NC surfaces, which leads to a dramatically different response of their respective emission intensities to the local chemical environment:[75] the core PL is weakly affected by the surface chemistry, while suppression (activation) of electron trapping under negative (positive) electrochemical potentials leads to strong enhancement (quenching) of the green shell PL, resulting in a trajectory from red-to-yellow-to-green of the total emission colour as a function of the oxidative vs. reductive nature of the NC surroundings.[77]

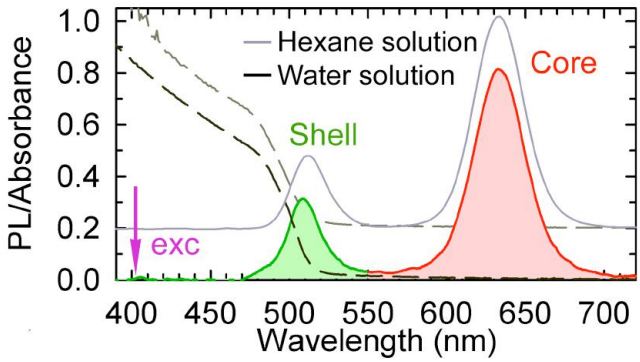

Figure 3.4 Optical absorption (dashed lines) and photoluminescence (solid lines) spectra (λ_{EXC}=405 nm, excitation fluence 1μJ/cm^2) of as-synthesized CdSe/CdS DiB-NCs (core radius=1.5 nm, shell thickness=8.5 nm) capped with oleic acid in hexane (grey lines) and of the same NCs in water obtained through ligand exchange with thioglycolic acid molecules (black lines, pH=7). The absorption and emission spectra of the hexane NC solution have been rigidly shifted for clarity. The core and the shell emission bands in the spectra of aqueous NCs are highlighted by red and green shading, respectively.

Furthermore, in DiB-NCs, quenching of the shell PL is due exclusively to the extraction of photogenerated shell electrons, whereas holes photogenerated in the shell are unaffected by surface states and chemical agents due to their very short (~20-45 ps) residence time in the shell states. As a result, DiB-NCs are sensitive mostly to electron-withdrawing agents,[77] which makes them particularly suitable to optically probe the acidity of the NC surroundings and eliminates possible cross-sensitivity errors due to the competition between electron- and hole-trapping processes that characterize conventional core-only NCs. As previously discussed, thanks to this intrinsic ratiometric sensing ability, DiB-NCs have been used to probe the local charge distribution at the interface between light-sensitive organic semiconductor thin films and water,[139] which constitute the functional platform of neural stimulation devices[67] for the realization of artificial retinal prosthesis for visual restoration.[68] These conditions resemble very closely the situation encountered

in the pH sensing experiment schematically depicted in Fig.3.2: H^+ ions act as electron scavengers resulting in a drop of the shell PL, while OH^- species saturate electron poor surface states, thus enhancing the shell emission intensity. As a result, DiB-NCs can be used as intracellular ratiometric pH sensors whose response, in contrast to conventional ratiomeric pH probes, relies on the direct interaction between the photoexcited carriers and the local chemical surroundings.

The CdSe/CdS DiB-NCs were synthesized according to the procedure reported in ref.[76] using oleic acid as capping agent. To render the NCs soluble in water and thus compatible with bio-imaging experiments, a ligand exchange procedure with thioglycolic acid was performed.[140] The optical properties of DiB-NCs are fully preserved upon the ligand exchange procedure, as reported in Fig.3.4, the optical absorption and PL spectra of a water solution of thioglycolic acid capped CdSe/CdS DiB-NCs and the analogous hexane solution of as-synthesized DiB-NCs capped with oleic acid are compared. The organic and aqueous solutions show identical absorption spectra, with onset at ~520 nm due to strong absorption by the thick CdS shell, and PL profiles featuring two separated bands at 635 nm and 515 nm ascribed to the recombination of core and shell excitons, respectively.[76] The PL quantum efficiency of the pristine NCs (Φ_{PL}=14±2%) is also unchanged upon the ligand exchange procedure, as further confirmed by experimental quantum yield measurements and by the essentially identical decay dynamics of both the core (average lifetime $<\tau_C>$~35 ns) and shell ($<\tau_S>$~100 ps) emission in the two solvents reported in Fig.3.5.

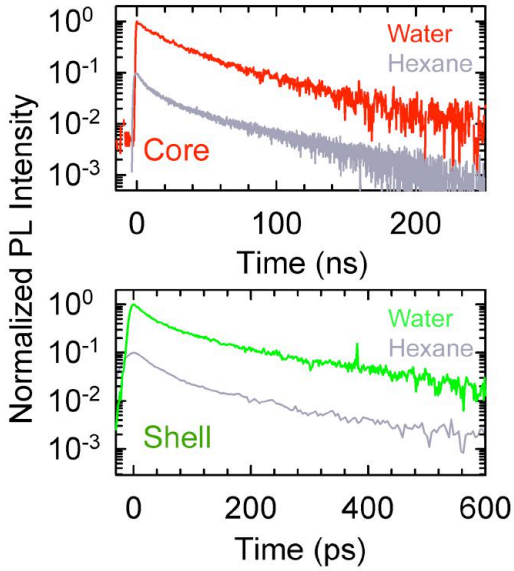

Figure 3.5 Comparison between the time decay curves of the core (upper panel) and the shell (lower panel) emissions of the two NC solutions, showing essentially identical recombination dynamics in water and in hexane.

In order to test the photostability of pristine and ligand exchanged NCs, I monitored their PL intensity for 15 minutes under continuous illumination with UV light. The data in Fig.3.6 shows stable emission from the core and the shell for both the hexane and the water solution, thus confirming the stability of the NCs for illumination times significantly longer than the typical bio-imaging experiment.

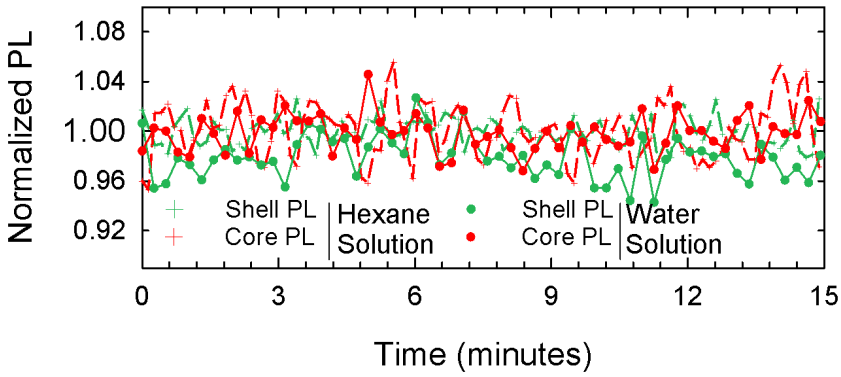

Figure 3.6 Normalized integrated PL intensity of the core (red curves) and the shell (green curves) emission under continuous illumination (λ_{EXC}=405 nm, excitation fluence 1μJ/cm^2) for thioglycolic-capped (circles) and oleic acid passivated (crosses) CdSe/CdS DIB-NCs in water and hexane respectively.

Notably, the two-color emission of DiB-NCs is essentially independent of temperature in the 0-70°C range, as highlighted in Fig.3.7 that shows a rigid red-shift of ~8 nm of both emission peaks and nearly constant I_S/I_C ratio and its first derivative $d(I_S/I_C)/dT$ across the whole temperature range. This is important for ratiometric pH sensing as it removes possible cross sensitivity effects due to variations of the sample temperature during the measurements.

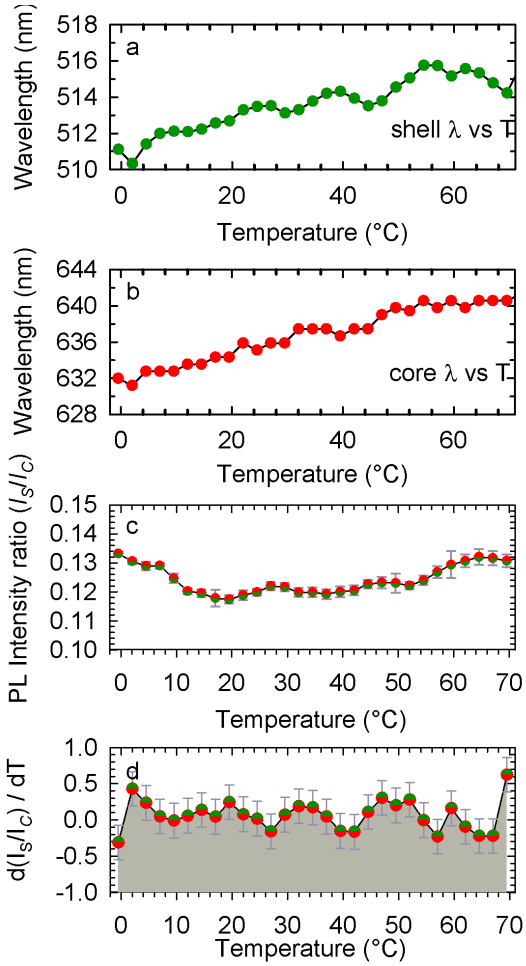

Figure 3.7 Temperature dependent spectral shift of the shell (**a**) and core (**b**) emission at 510 nm and 640 nm respectively. **c**) Temperature dependence of the ratio between the core and the shell integrated PL intensities (I_S/I_C, red/green cyrcles) and **d**) the first derivative of the (I_S/I_C)-vs.-T dependence. All measurements were performed using the 15 μJ/cm^2 excitation fluence and the excitation wavelength of 400 nm.

3.2 Results

pH sensitivity in solution

After assessing the stability of the DiB-NCs in polar environments, I proceeded with the demonstration of their ratiometric pH sensing ability. With this aim, Imonitored the PL of DiB-NCs in water as a function of the pH, which Icontrolled through titration with HNO_3 and NaOH under intense stirring. Figure 3.8 displays a set of PL spectra for increasing pH from 2 to 11 recorded using cw excitation at 405 nm.

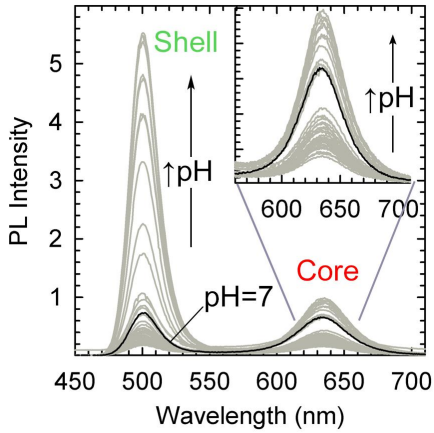

Figure 3.8 Photoluminescence (PL) spectra of thioglycolic acid capped CdSe/CdS DiB-NCs in water at increasing pH (2-11) under 405 nm excitation (fluence 1 μJ cm^{-2}). The spectrum corresponding to the neutral condition (pH=7) is shown as a black line for reference. The inset shows a magnification of the core emission band as a function of the pH for clarity.

In Figure 3.9, I plot the amplitudes of the shell (I_S) and the core-related (I_C) PL bands extracted from the spectra together with their intensity ratio, I_S/I_C.

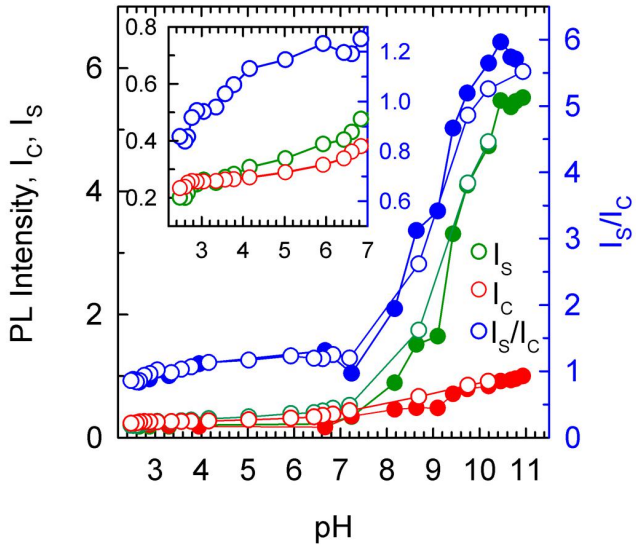

Figure 3.9 Integrated intensity of the core (red circles, I_C) and the shell (green circles, I_S) emissions as a function of the pH in two consecutive cycles (full and empty circles) to demonstrate the reversibility of the pH sensing response. The ratio between the shell and core emission intensities (I_S/I_C) is reported as blue circles. The inset highlights the acidic pH range (one cycle only for clarity), showing a 2-fold variation of the ratiometric response.

The data shows the progressive growth of both emissions with increasing pH, which is ascribed to the progressive suppression of electron harvesting by H^+ ions upon basification of the solution (Fig.3.2), in agreement with spectro-electrochemical observations in reductive conditions.[77] According to the direct exposure of shell excitons to the NC surfaces, I_S undergoes intense, ~30-fold, enhancement with increasing pH, which is almost 10 times stronger than the growth experienced by I_C in the same pH range (~4-fold increase). I notice that the same response is obtained in consecutive pH ramps (see filled dots in Fig.3.9). As a result of this strong difference in pH sensitivity, I_S/I_C spans from 1 to 6 as a function of the pH with a major effect in the basic region (Fig.3.9), leading to a progressive change of the total emission colour from red to green. This effect is highlighted in Fig.3.10, where I report the photographs of the

DiB-NCs solution at pH=3 and pH=11 under 400 nm laser excitation showing distinct red and green luminescence, respectively.

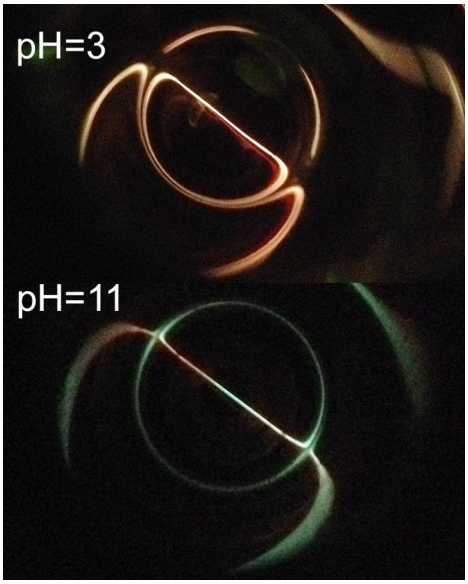

Figure 3.10 Top view photographs of the NC solution during the titration experiment at pH=3 (top panel) and pH=11 (lower panel) showing the dramatic change of total luminescence colour from red (dominated by the core emission) to green (dominated by the shell PL) upon increasing the solution pH.

In order to gather deeper insight into the ratiometric sensing mechanism of DiB-NCs, I measured the time dynamics of both the core and the shell PL as a function of the pH. Looking first at the core emission in Fig.3.11, it can be noted that the decay profile is essentially unaffected by the NC environment, whereas the zero-delay emission intensity grows with increasing pH.

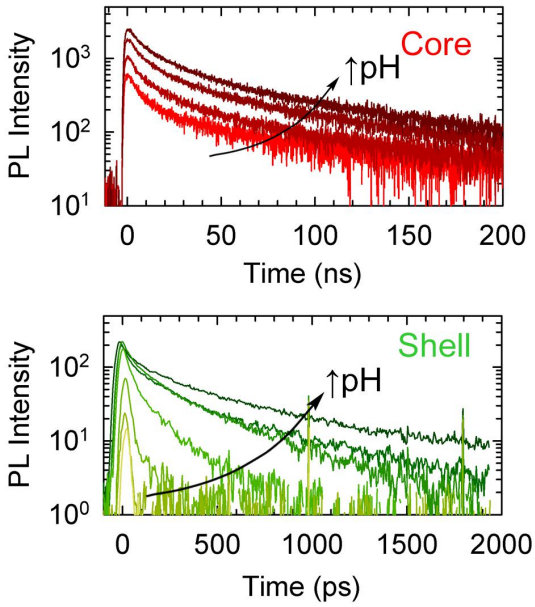

Figure 3.11 Normalized time decay curves of the core (red lines, λ_{PL}=635 nm) and the shell (green lines, λ_{PL}=500 nm) PL at increasing pH (as indicated by the arrow).

This indicates that the electron capture process responsible for PL quenching in acidic conditions is much faster than the ~ 1 ns resolution of the time-correlated single photon counter used for measuring the core PL dynamics. Since the core excitons are localized away from the NC surfaces, extraction of core electrons occurs in only a minor fraction of the NCs ensemble, whereas, in the majority of NCs, the core excitons are almost unaffected by the external conditions, leading to the mild sensitivity of the core PL of the local pH observed in the c.w. measurements. On the other hand, the inspection of the shell PL dynamics performed using a streak camera with ~5 ps resolution, reveals a strong effect of the pH on both the zero-delay PL intensity and on the shell exciton lifetime. This observation points to the coexistence of a distribution of electron capture processes occurring on different time regimes and affecting different subpopulations of NCs in the ensemble. The growth of the zero-delay signal confirms the ultrafast nature of the electron capture process

observed for the core PL that, in a large portion of NCs in the ensemble, depletes the shell conduction band from photo-excited electrons before their radiative decay or localization into core states.[77] Concomitantly, the shell PL lifetime gradually increases upon basification, due to the progressive suppression of slower electron trapping processes, most likely associated to the distribution of NC-H^+ distances in water solution and with the variety of surface sites mediating the electron capture mechanism.[77]

In vitro measurements

To experimentally validate the ratiometric sensing ability of DiB-NCs in *in vitro* conditions, using confocal fluorescence microscopy, I monitored their PL as a function of the intracellular pH after internalization into Human Embryonic Kidney (HEK-293) cells. For fixed cells, the pH was changed by titrating the phosphate-buffered saline (PBS) solution with NaOH or HNO_3 solutions (0.1M) and each image of the same cell was recorded under identical excitation and collection conditions after 15 minutes from the addition of the titrating solution, so as to ensure the achievement of stable intracellular pH. In Fig.3.12 I report the fluorescence images of two HEK-293 cells stained with DiB-NCs overlaid to their respective bright field images (Fig.3.12a-e). Because the DiB-NCs are not functionalized with target-specific ligands, they disperse inside the cell forming small domains of aggregated NCs, enabling to visualize the local intracellular environment even at very low concentration. Better dispersion of the NCs inside the cell or their targeting to specific subcellular organelles is in principle achievable by suitable capping with site selective functionalities, which is however beyond the scope of this proof-of-principle study.

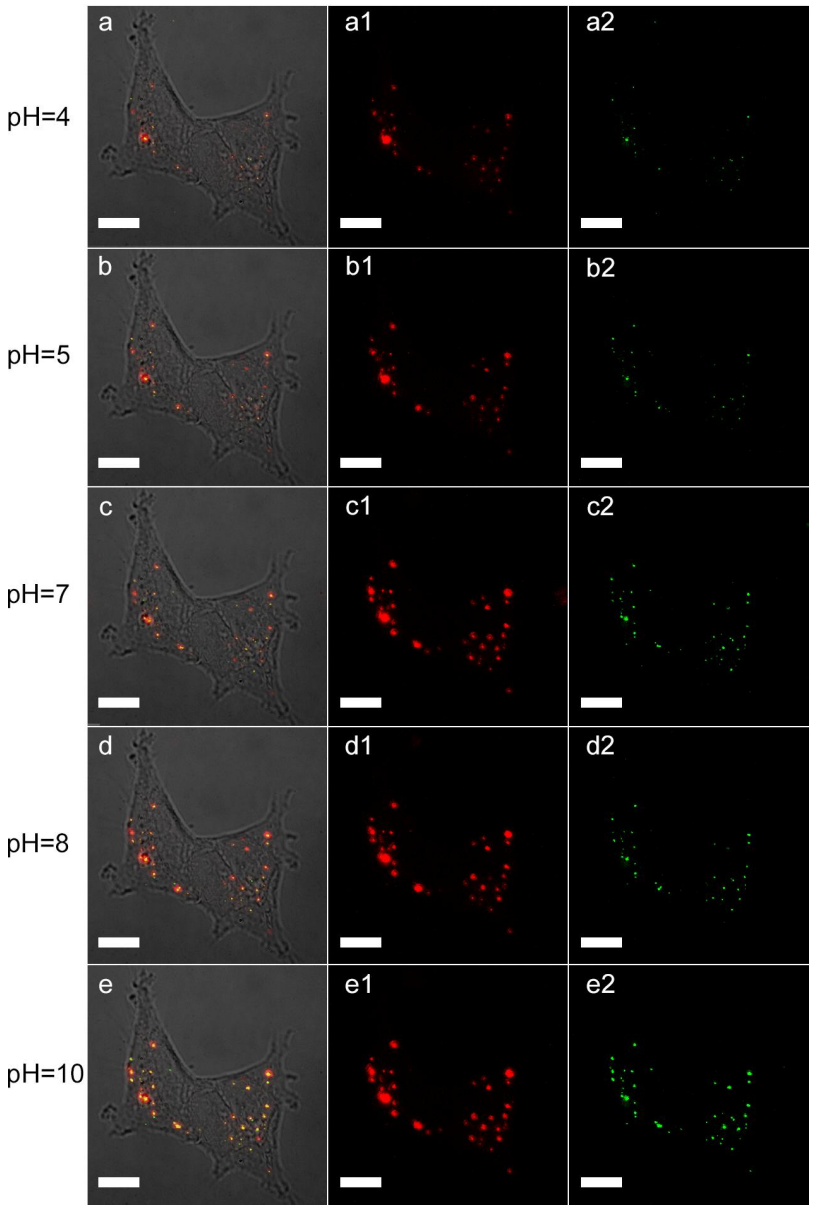

Figure 3.12 Confocal images of HEK-293 cells stained with 130 nM DiB-NCs at increasing pH collected under 405 nm excitation (fluence 18 μJ cm^{-2}). **a**-**e**. Overlay of confocal images and bright-field images collected with a 60x, 1.4 NA, oil immersion objective. Evolution of the core (**a1**-**e1**) and shell (**a2**-**e2**) emission with increasing pH. The scale bar is 10μm for all panels.

In order to emphasize the ratiometric pH response of the DiB-NCs, in Fig.3.12a1-e1 and 3.12a2-e2, I report the fluorescence images collected using the red and green detector channels of the confocal microscope, so as to selectively monitor the evolution of the core and the shell PL, respectively. These set of images show the progressive emergence of the green shell luminescence for increasing pH (pH= 4-10) in agreement with the sensing behaviour observed in the ensemble measurements.

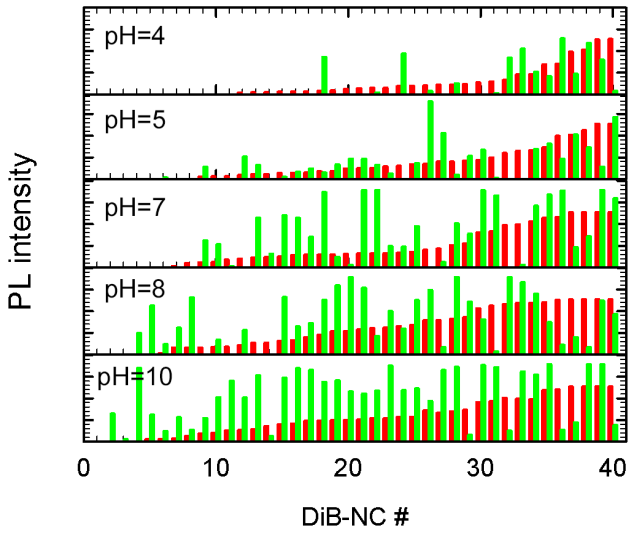

Figure 3.13 Histograms of shell (green bars) and core (red bars) PL intensity of the DiB-NCs collected selectively with the green and the red detector channels at increasing pH.

The quantitative estimation of the ratiometric sensing response obtained by extracting the intensity of the two detection channels for 40 emitting spots as a function of the pH is reported in Fig.3.13. In Fig.3.14, I report the average ratiometric response $\langle I_S/I_C \rangle$ corresponding to the average pH response per detection spot, showing a similar trend as the ensemble response reported in Fig.3.9.

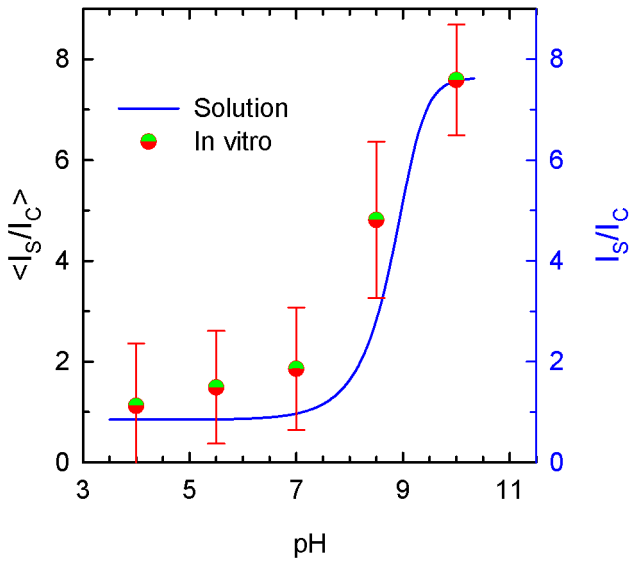

Figure 3.14 Average shell-to-core PL intensity ratio (<I_S/I_C>) as a function of the pH in fixed HEK-293 cells extracted from the histograms in Fig.3.13 (circles). The ensemble I_S/I_C measured in aqueous solution is reported as a blue line.

The differences between the absolute values of the ratiometric response in the confocal and far-field measurements is most likely due to the different optical configuration used in the two experiments and by the local inhomogeneity of the intracellular pH. It is important to note that cell fixation preserves the tissues from degradation, but it terminates every biochemical process inside the cell, resulting in a different chemical environment with respect to that found in a living sample.[141-145]

In vivo measurements

To demonstrate that this approach is suitable for ratiometric intracellular pH sensing also in living cells, I studied internalized DiB-NCs into HEK-293 cells in Krebs-Ringer Bicarbonate (KRH) buffer solution and induced changes in the intracellular pH by exposing the living cells to chloroquine, a weakly basic amine that accumulates into the lysosomes and into the Golgi apparatus, resulting in the basification of the intracellular environment.[146] Prior to the pH monitoring experiments, the cytotoxicity of DiB-NCs has been evaluated by performing the MTT [3-(4,5-dimethylthiazol-2-yl)-2,5-diphenyltetrazolium bromide] assay on the HEK-293 cells after 6h, 24h, 48h and 72h of incubation with and without the NCs. MTT is reduced to formazan in living cells. Since this reduction depends on the cellular metabolic activity, stronger formazan optical absorption indicates progressively larger cell population.[147,148] Figure 3.15 shows the results of the MTT assay on cells stained with increasing concentrations of DiB-NCs, showing that cell proliferation is unaffected by the NCs, even at high concentration, which indicates good biocompatibility of DiB-NCs.

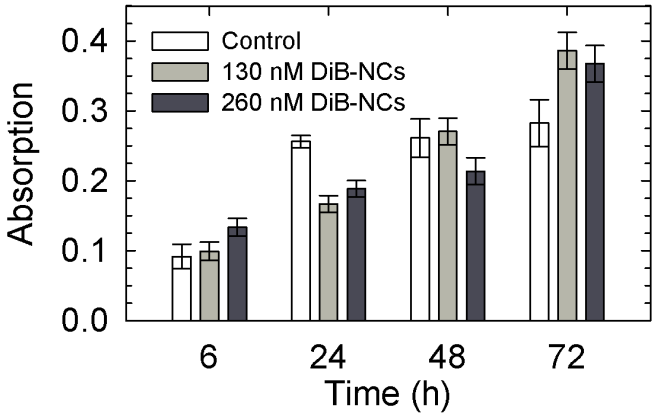

Figure 3.15 MTT test for cell viability up to 3 days in vitro for two different DiB-NCs concentrations (130 nM and 260 nM) and for untreated control cells (ctrl). Data are reported as average n = 12 ± SE.

Based on these results, I proceeded with the pH measurements by exposing the cells to chloroquine. In Figure. 3.16, Ishow confocal images of a single living HEK cell stained with DiB-NCs before and 30 minutes after the exposure to a 400μM chloroquine solution,[149] overlaid to the respective bright field pictures. A first look at the confocal data reveals the significant brightening of the green shell PL upon addition of chloroquine, in agreement with its expected basification effect on the cell cytoplasm.

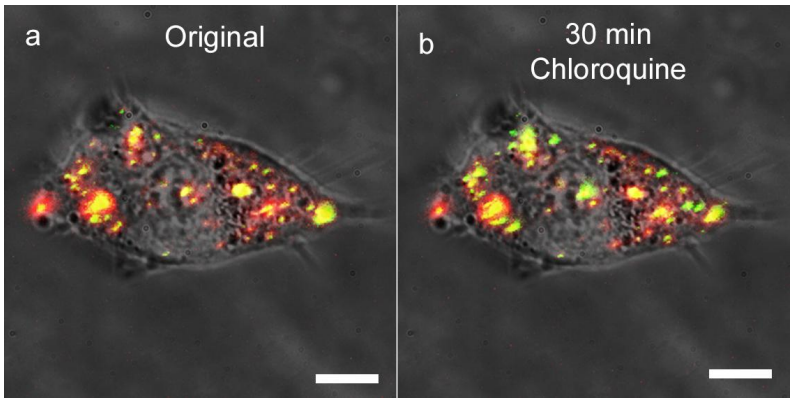

Figure 3.16 Overlay of confocal images collected with the red and green detector channel and bright-field images of living HEK cells stained with 130 nM DiB-NCs at increasing pH. The intracellular pH was modified by adding a 400 μM solution of chloroquine. The measurements were performed 30 min after adding the chloroquine solution.

To quantify the variation of the core and shell PL intensity and confirm the reproducibility of the pH sensing assay, in Fig.3.17 I report the histograms for 40 representative emitting spots for five different cells, showing the progressive enhancement of the shell emission with exposure time, whereas the core PL remains essentially unaltered by the addition of chloroquine.

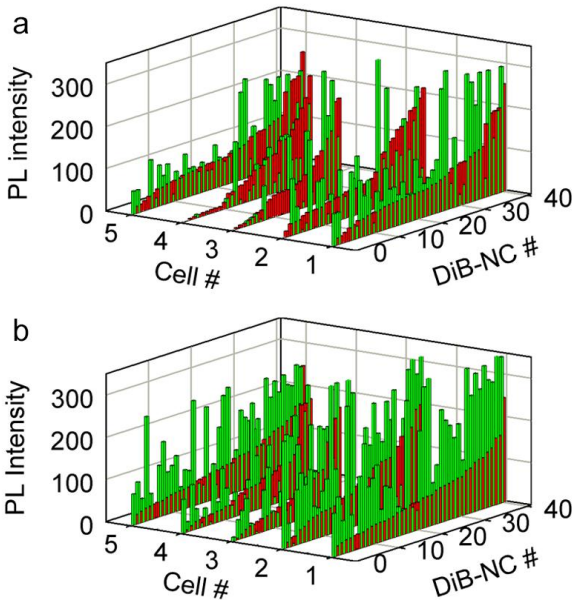

Figure 3.17 Histograms of green and red photoluminescence intensities for a statistically relevant ensemble of 40 NCs repeated for 5 different cell cultures, before (**a**) and 30 minutes after (**b**) the addition of chloroquine.

As a result, the $\langle I_S/I_C \rangle$ ratio increases almost by a factor of two for 30-minutes exposure (Fig.3.18), thus confirming the suitability of the NCs as pH-sensitive optical probes for in-vitro applications.

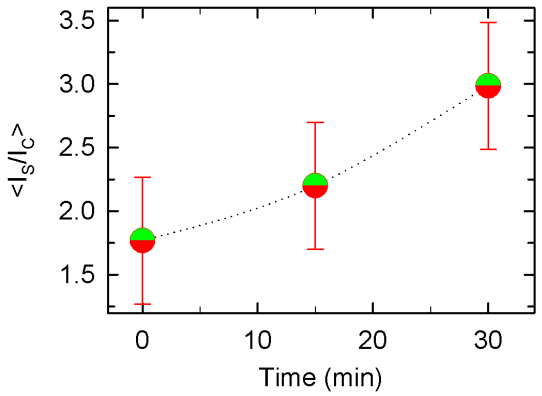

Figure 3.18 Average shell-to-core PL ratio as a function of exposure time to chloroquine extracted from the histograms in Fig.3.17.

3.3 Conclusions

In conclusion, I demonstrated the use of heterostructured NCs as intrinsic ratiometric probes for intracellular pH sensing. With this aim, I used CdSe/CdS DiB-NCs that show a characteristic two-color emission arising from the simultaneous radiative recombination of core and shell excitons that are differently affected by the NC surfaces and chemical agents and can therefore be exploited to ratiometrically probe the local NC environment. This has been demonstrated through far-field spectroscopic measurements upon titration with HNO_3 and NaOH, leading to ~600% enhancement of the shell-to-core PL ratio and through confocal measurements on fixed and living HEK-293 cells in controlled pH conditions. Cell viability studies reveal good bio-compatibility of the DiB-NCs corroborating their potential as intracellular pH sensors. The reported proof-of-principle CdSe/CdS NCs are not optimized in terms of the thickness of the CdS shell or the choice of the capping ligand and further improvements in the photoluminescence quantum efficiency and pH sensitivity might therefore be expected by optimizing the surface coverage and functionalization. The strategy demonstrated here for test-bed CdSe/CdS hetero-NCs is not composition specific and might, in principle, be extended to other semiconductors free from heavy metal elements, such as ternary I-III-VI_2 NCs,[150] as well as to heterostructures with different band alignment (type I, inverted type I etc…), so as to specifically tune the ratiometric response to acidic or basic conditions through selective exposure of holes or electrons to the intracellular environment.

4 Single-particle ratiometric pressure sensitive paints based on 'double-sensor' colloidal nanocrystals

Ratiometric pressure sensitive paints (*r*-PSPs) are all-optical probes for monitoring oxygen flows in the vicinity of complex or miniaturized surfaces. They typically consist of a porous binder embedding mixtures of a reference and a sensor fluorophore exhibiting oxygen-insensitive and oxygen-responsive luminescence, respectively. In this work I realize the first example of an *r*-PSP based on a single two-colour emitter that removes limitations of *r*-PSPs based on fluorophore mixtures such as different temperature dependencies of the two fluorophores, cross-readout between the reference and sensor signals and phase segregation. In this paradigm-changing approach, I utilize a novel "double-sensor" *r*-PSP that features two spectrally-separated emission bands with opposite responses to the O_2 pressure, which boosts the sensitivity with respect to traditional reference-sensor pairs. Specifically, I use two-colour-emitting CdSe/CdS core/shell nanocrystals, exhibiting red and green emission bands from their core and shell states whose intensities are respectively enhanced and quenched in response to the oxygen partial pressure. This leads to strong and reversible ratiometric response at the single particle level and over 100% enhancement in the pressure sensitivity. This proof-of-concept *r*-PSPs further exhibit suppressed cross-readout thanks to zero spectral overlap between the core and shell luminescence and temperature independent ratiometric response between 0°C and 70°C (see previous chapter).

4.1 Introduction

Pressure sensitive paints (PSPs) are effective, non-intrusive tools capable of mapping gas flows near complex surfaces and reporting on the concentration of oxygen in gas mixtures through remote optical detection. The foremost use of PSPs is in aerospace engineering, with applications ranging from aerodynamic tests of aircraft prototypes[151,152] to fundamental studies in acoustics[153], shock-wave propagation and transonic buffeting effects[154] (see Fig.4.1a,b). PSPs are also widely used in the design of complex fluidic and microfluidic systems[155], including supersonic micronozzles[156], microfluidic oscillators[155], microchannels[157], and in studies of pressure, heat-transfer and shear stress in micromechanical devices[158] (Fig.4.1a,b). Furthermore, PSPs are employed in environmental monitoring[159], marine research[160], the food packaging industry[161], medicine[162] and biology[163]. Traditional PSPs consist of an oxygen sensitive organic fluorophore dispersed in a porous organic[164] or inorganic[153,165] matrix (commonly referred to as a "binder"). When exposed to O_2, the luminescence of the fluorophore is quenched proportionally to the oxygen partial pressure, thus allowing for real-time pressure monitoring. The all-optical working mechanism of PSPs makes these devices substantially simpler than conventional piezoresistive[166] or MEMS-based transducers[167] that require the integration of the sensors and the wiring on the investigated surfaces, which hinders their application in the case of moving or miniaturized parts[167]. In addition, traditional non-optical sensors yield point-like pressure measurements, whilst PSPs allow one to map the gas flow with high spatial resolution on extended or complex surfaces with a single optical scan[153,168]. This largely simplifies the data processing, which is particularly challenging in the case of turbulent or supersonic gas flows[169].

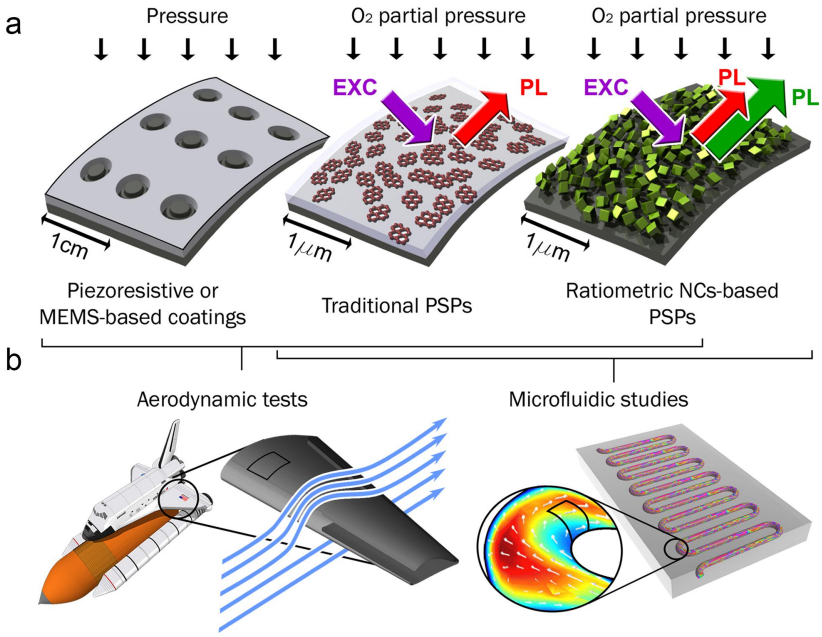

Figure 4.1 Working principles of single- and double-sensor ratiometric PSPs. **a**) Illustration of different technologies for pressure detection: (left) traditional MEMS-based transducers, (center) traditional organic chromophore-based PSPs, and (right) DiB-NC-based ratiometric PSPs. **b**) All of the pressure sensors from panel a can be used in (left) aerodynamic tests on model surfaces, whereas (right) microfluidic systems can be investigated only by means of PSPs.

State-of-the-art organic PSP fluorophores, such as metal porphyrins[170], pyrenes[171], and Ru(II) or Pt(II) complexes[172], have good oxygen sensitivity but suffer from limited thermal[173] and photochemical[174] stability. The interaction with O_2, which generates singlet oxygen radicals, accelerates photodegradation under UV illumination[168,169], leading to luminescence drops ranging from 1%/hour [151,168] up to 15%/hour [175]. In addition, the temperature-dependence of the luminescence efficiency, typical of organic fluorophores, introduces bias errors to the pressure data collected on different model parts and, therefore, requires continuous monitoring of the surface temperature and specific

calibration protocols[151,153,154,176]. Mixtures of O_2-sensitive and temperature-sensitive fluorophores, operating as pressure and temperature references for the other emitter, have been proposed to address this problem[177,178]. These PSPs require, however, effective encapsulation of the temperature sensor in oxygen-impermeable polymers to avoid cross-sensitivity issues.[153,179]

Colloidal semiconductor nanocrystals (NCs) have been recently proposed as potential alternative sensing materials for PSPs. NCs combine high emission efficiency[180-182] and size-tunable electronic properties[183,184] with enhanced stability and exceptionally large surface-to-volume ratios[185,186]. Similarly to organic fluorophores, O_2 sensing with NCs relies on quenching of the luminescence intensity under O_2 flow, mostly due to ultrafast extraction of surface and photogenerated electrons by oxygen[187]. From the physical perspective, the extraction of electrons from the NCs by exposing them to O_2 replicates the effect of lowering the Fermi level by applying a positive (oxidative) potential in electrochemical measurements. In direct analogy, the removal of oxygen from the NC surroundings resembles the effect of raising the Fermi level under negative (reducing) electrochemical potentials[188-190]. An advantageous feature of NCs from the standpoint of potential PSP applications is that the coupling of photogenerated carriers with phonons in these systems is much weaker than in organic fluorophores[191], which results in a smaller variation of the emission quantum yield in the temperature range typically explored in PSP studies (10-40 °C)[153,154,176,178]. Examples of O_2-responsive NCs include CdSe[192], CdTe[193], and CdSe/ZnS core/shell systems[194]. These structures have been utilized for humidity detection and dry gas sensing, as well as biological sensing applications[195]. As distinct from organic fluorophores, the use of NCs as PSPs emitters potentially eliminates the need for the binder, as NCs can be deposited directly onto tested surfaces (Fig.4.1a). This is particularly advantageous for high frequency sensing[154], since the rate-determining process in the sensing response is typically the permeation of a gas into the binder[151], which protracts the

response time from a few microseconds with porous matrices[154] to tens of seconds for traditional polymeric binders[196].

A common experimental difficulty of radiometric luminescence mapping using organic fluorophores or conventional NC-based PSPs is that they require accurate quantitative measurements of the emission intensity across extended or complex surfaces under oxygen flow and UV irradiation. For this reason, wind tunnel aerodynamic tests are typically performed by comparing the results of "wind-on" and "wind-off" measurements in order to account for the experimental geometry, model misplacements[151,169,187], non-uniform distribution of the fluorophore in the binder and an uneven thickness of the binder layer across the model surface[169,176,197].

Some of these issues have been addressed through the use of so-called ratiometric PSPs (*r*-PSP) that exploit the different sensitivity to O_2 of two (or more) fluorophores to detect and quantify local pressure variations. A conventional *r*-PSP consists of an O_2-insensitive fluorophore (the "reference") acting as an internal reference standard for the luminescence intensity of an O_2-responsive emitter (the "sensor"), as depicted in Fig.4.2a. Examples of reported two-component *r*-PSPs include mixtures of organic dyes[169] and dye-polymer conjugates[198] as well as organic/inorganic hybrid systems such as binary blends of dyes and NCs[165,169], NC-polymer nanocomposites[165,199] and dye-functionalized NCs[200]. Although these systems virtually remove the need for the wind-off/wind-on calibration, their use is still associated with several experimental difficulties arising from *i*) the different temperature dependence of the two fluorophores[169,201], *ii*) cross-read out errors due to the spectral overlap between the emission bands of the reference and the sensor[202] and *iii*) spatial inaccuracy due to inhomogeneous distribution of the emitters on the model surfaces or in the binder[202], whose effects are aggravated by intermolecular interactions leading to exciton migration processes[187,198].

Here I demonstrate that all of these limitations can be alleviated using *r*-PSPs based on a single dual-colour emitter that features

intrinsic ratiometric response at the single particle level, suppressed cross-readout due to a zero overlap between the luminescence spectra of the two emissive states, a dynamic range of ratiometric O_2-pressure sensing of three orders of magnitude, and the temperature-independent ratiometric response between 0°C and 70°C. To date, the only example of a single emitter showing ratiometric oxygen response is represented by fluorescent/phosphorescent macromolecules[187,203] proposed for tumor hypoxia diagnostics. An important advantage of this new approach is that it is based not on an inert (pressure-insensitive) reference, but instead combines two pressure-sensitive states in a single emitter and that these states exhibit opposite luminescence responses to changes in the oxygen pressure. In these "double-sensor" systems, one emission channel is quenched, whilst the other is concomitantly enhanced by the presence of O_2, similarly to the so-called "reverse sensing" behaviour recently found in CdSe colloidal quantum wells[186]. Figure 4.2a and 4.2b schematically compare the luminescence-vs.-pressure dependence of a conventional reference-sensor pair (R and S, respectively) and that of a double-sensor *r*-PSP (respectively S_1 and S_2). Importantly, whilst the response of a conventional *r*-PSP featuring an inert reference is given solely by the sensor that determines the maximum ratiometric O_2-sensitivity of the blend (S/R in Fig.4.2a), replacing the inert reference with a "reverse" O_2 sensor exhibiting enhanced luminescence when exposed to O_2 (S_2 in Fig.4.2b), leads to strongly amplified ratiometric sensitivity. I note that in the presence of two sensing species, the ratiometric response can be conveniently chosen (S_1/S_2 vs. S_2/S_1) in order to better suit the experimental conditions, whilst ensuring in both cases enhanced sensitivity with respect to the conventional reference/sensor system.

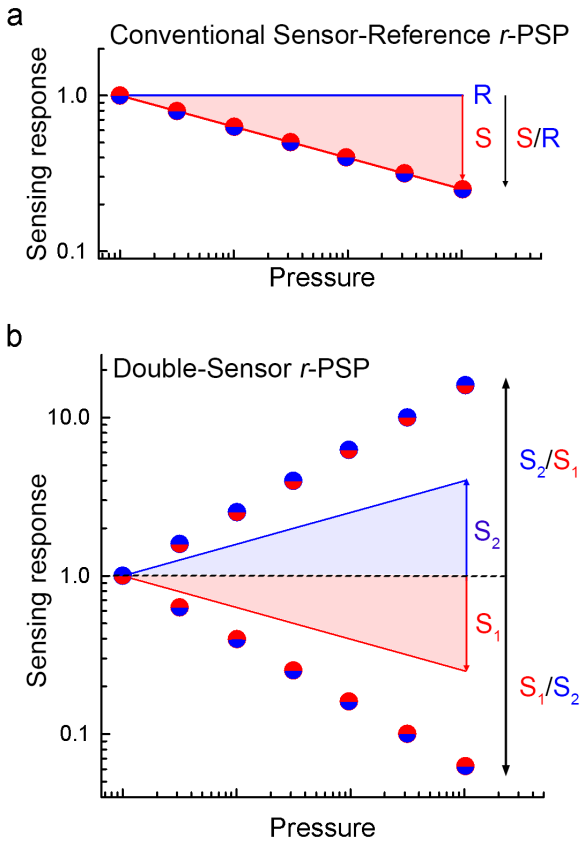

Figure 4.2 Outline of the ratiometric response of **a**) conventional r-PSPs featuring an inert (pressure-insensitive) reference (R, blue line) and an O_2 sensitive emitter (S, blue line). The ratiometric response (circles) is determined by the sensitivity of the sensor. **b**) Ratiometric response of a double-sensor r-PSPs consisting of two O_2 sensing emitters (S_1 and S_2) with opposite luminescence responses. In this case, the ratiometric response (circles) can be expressed as S_1/S_2 or S_2/S_1; in either case, it is strongly amplified with respect to the sensitivity of the individual sensor species.

This "double-sensor", single-emitter *r*-PSP uses CdSe/CdS dot-in-bulk (DiB) NCs that consist of a small CdSe core overcoated with an ultra-thick CdS shell[188,204]. Owing to their peculiar internal structure, DiB-NCs are capable of simultaneously sustaining core and shell excitons, whose radiative

recombination leads to two-colour (red and green) luminescence under both low-fluence continuous wave optical excitation[204] and electrical injection[188]. Two essential structural features of these NCs are an abrupt core/shell confinement potential and an engineered polytypic interphase of zincblende CdS separating the zincblende CdSe core from the thick wurtzite CdS shell. This peculiar structure of the core-shell interface slows down relaxation of shell-localized holes into core states, which leads to the development of efficient shell emission observed simultaneously with emission from the core. Importantly for *r*-PSP applications, the shell excitons are exposed to NC surface species, and their luminescence is highly sensitive to nonradiative electron transfer to surface defects or molecular acceptors (in this case oxygen) adsorbed onto the NC surface that lead to luminescence quenching[77]. In stark contrast, the emission arising from core-localized excitons is enhanced by exposure to O_2 as the removal of extra electrons generated by photocharging would quench nonradiative Auger recombination.[77] As a result of these effects, the two emission channels of the DiB-NCs follow opposite trends with increasing/decreasing O_2 partial pressure, which allows to realize the double-sensor ratiometric response regime using a single emitter.

4.2 Results

Ratiometric oxygen sensing using DiB-NCs

I start this work by demonstrating the ratiometric O_2 sensing ability of DiB-NCs by monitoring the evolution of their PL spectrum during stepwise pressure ramps from P=1 to 10^{-3} bar. In these experiments, the luminescence of a sub-monolayer film of DiB-NCs dip-casted onto a glass substrate is excited by 400 nm light and continuously collected with a CCD camera, while the sample chamber, originally filled with O_2, is progressively evacuated through rapid pressure steps. For each step, the pressure is lowered by a factor of ten and maintained constant for 90 seconds. After the final step at 10^{-3} bar, the chamber was refilled step-wise with O_2 following the same procedure. Since the O_2 concentration is proportional to the total pressure, these measurements directly yield ratiometric estimations of the pressure on the sample surface similarly to what is typically achieved with PSPs. As evident from the PL spectra in Fig.4.3, the core and shell PL intensities demonstrate the opposite trend in response to changes in the chamber pressure. Specifically, the core PL undergoes progressive dimming upon evacuation, while the shell emission increases and becomes dominant at P=10^{-3} bar. Importantly, refilling the sample chamber with nitrogen does not lead to recovery of the PL intensity, which confirms the essential role of oxygen in the sensing response.

The observed difference between the O_2 response of the core and the shell PL can be rationalized by considering the electron withdrawing nature of molecular oxygen, which, in the ground state, is a diradical triplet with strong electron acceptor character. As a result, O_2 is capable of efficiently extracting electrons from both the quantized states[205] of the NCs and electron-rich surface defects that thereby become capable of trapping photogenerated electrons from the NC conduction

band[186]. Similarly to the effect of raising the NC Fermi level obtained by either applying a negative electrochemical potential or direct electric bias in light-emitting diodes[77,188], the removal of oxygen progressively suppresses electron trapping, leading to the observed strong enhancement of the green luminescence due to increased radiative recombination efficiency of shell excitons. On the other hand, as observed previously[206,207] and confirmed by time-resolved PL measurements in controlled atmosphere (see a detailed discussion later in this work), the dimming of the core PL is associated with nonradiative Auger recombination of negatively charged core excitons (negative trions), which are formed due to accumulation of excess electrons in the NCs in the absence of electron withdrawing O_2 molecules. A similar effect has recently been observed with other CdSe/CdS heterostructures including thick-shell NCs[206,207] and colloidal nanoplatelets[186].

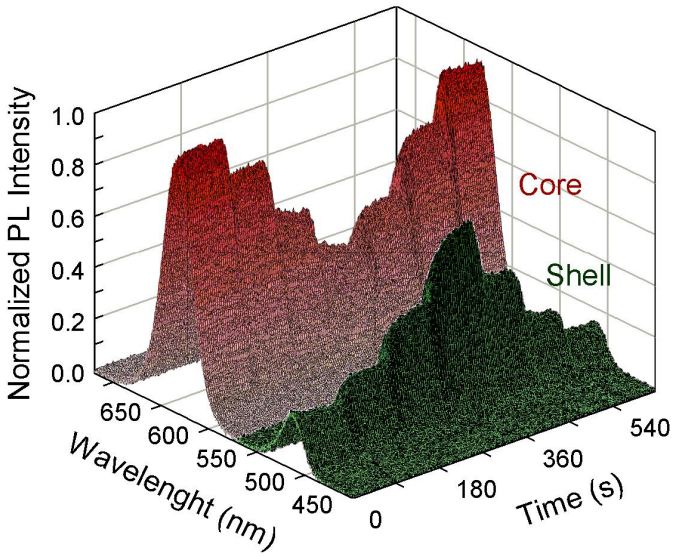

Figure 4.3 A series of PL spectra (1 s acquisition time per frame, 90 s steps) during a stepwise pressure scan. The pressure is reduced rapidly and kept constant for 90 s, starting from atmospheric pressure (P=1 bar) to 10^{-1}, 10^{-2} and 10^{-3} bar, after which the sample chamber is stepwise refilled up to the initial pressure level of P= 1bar.

In order to quantify the ratiometric luminescence response of DiB-NCs, in Fig.4.4 I report the integrated core and shell PL intensity extracted from Fig.4.3, both normalized to their initial value at P=1 bar. Each step-like variation of the O_2 pressure leads to a concomitant modulation of both emission bands. Specifically, lowering the pressure from 1 bar to 10^{-3} bar results in ~60% dimming of I_C and over 300% increase of I_S.

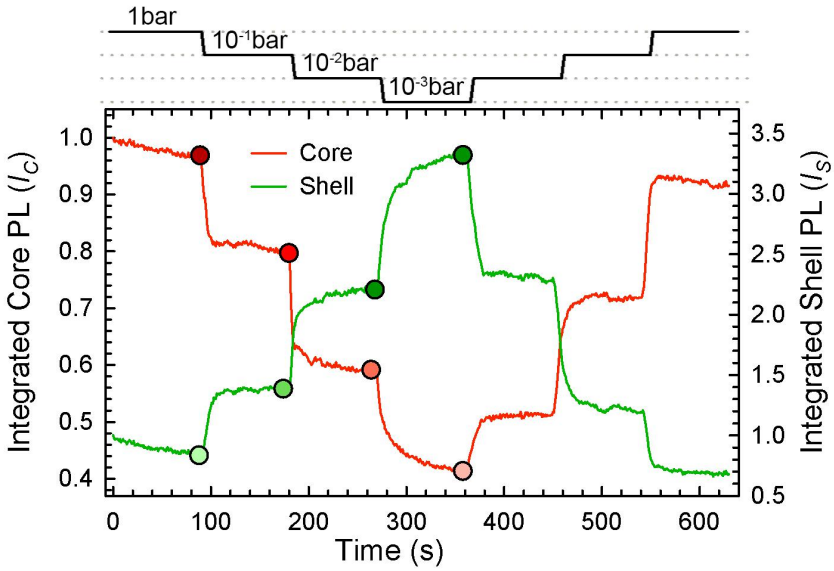

Figure 4.4 Integrated PL intensity of the core (I_C, red line) and the shell (I_S, green line) PL extracted from the stepwise pressure scan in Fig.4.3. Both trends are normalized to the initial PL intensity values at P=1 bar.

Upon ramping the O_2 pressure back up to 1 bar, both the core and the shell emission bands fully recover their original intensities. The opposite sign of the luminescence response of the core and the shell is emphasized in Fig.4.5, where I report I_C and I_S collected at the end of each pressure step (highlighted with dots in Fig.4.4) as a function of the O_2 pressure. Thanks to this peculiar feature of DiB-NCs, the ratiometric response considerably exceeds the sensing response of the individual emitting states, with the enhancement reaching 100% with

respect to I_S and over 600% with respect to I_C across the whole investigated pressure range.

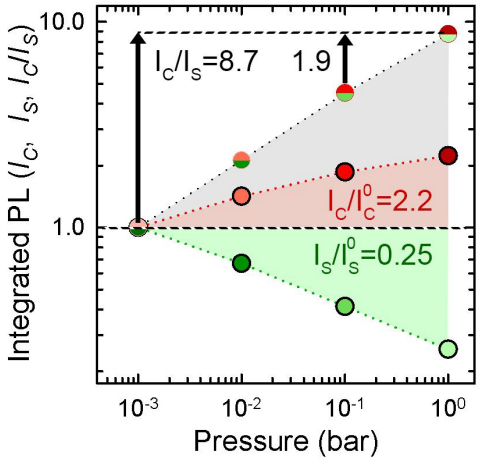

Figure 4.5 The I_C and I_S values (red and green dots, respectively) and the I_C/I_S ratio (red/green dots) as a function of increasing pressure (logarithmic scale). All trends are normalized to their respective value at atmospheric pressure (I^0_C and I^0_S respectively).

Interestingly, the strong response to the O_2 pressure leads to significant change of the total emission colour, as displayed in Fig.4.6a, which shows the projection of the emission colour coordinates extracted from the PL spectra of Fig.4.3 onto the CIE (*Commission Internationale de l'Éclairage*) chromaticity diagram. The colour change is easily appreciated by examining the photographs of the DiB-NCs film taken at P=1 bar and P=10^{-3} bar under UV illumination (Fig.4.6b).

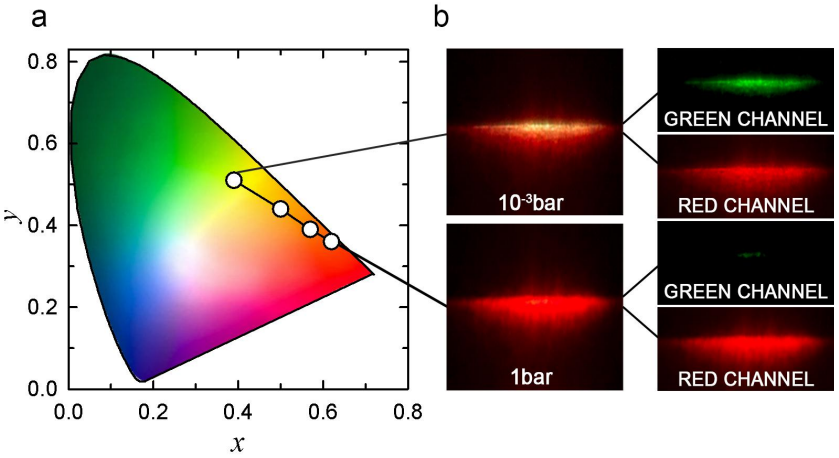

Figure 4.6 **a**) Overall emission colour of a DiB-NC film extracted from the PL spectra in 'a' and projected onto the CIE (Commission Internationale de l'Éclairage) chromaticity diagram. **b**) Photographs of a DiB-NCs sample at oxygen pressure of 1 bar and 10^{-3} bar (top left and top right, respectively) under UV illumination collected using UV-filtered camera. The signals detected selectively by the red and green channels are reported in the right panels for direct confirmation of suppressed cross-readout.

At atmospheric pressure, the film appears red, due to the dominant contribution of the core emission at 632 nm (see PL spectra in Fig.4.3). Upon lowering the O_2 pressure to 10^{-3} bar, the total emission colour turns whitish, as a result of the contribution from strong green emission by the CdS shell. Importantly, since the core and shell emissions are fully spectrally separated, their respective signals are collected selectively by the red and green detection channels with no cross readout. This is highlighted in the right panels of Fig.4.6b, showing a strong red signal and essentially no green emission at P=1 bar. Under vacuum, the green signal increases significantly, whilst the red channel shows a concomitant dimming, in agreement with the quenching of the core PL observed upon evacuation of the sample chamber.

Single particle ratiometric oxygen sensing using DiB-NCs

An important feature of DiB-NCs is that they behave as ratiometric pressure sensors even at the single-NC level, which makes them capable of reporting O_2 pressure variations with nanoscale spatial resolution. This represents a unique advantage over PSPs based on fluorophores blends and simplifies the paint processing by removing issues associated with the inhomogeneous distribution of the emitters on the model surfaces or in the binder, the factors that typically reduce the spatial accuracy in sub-micron-scale pressure studies[202].

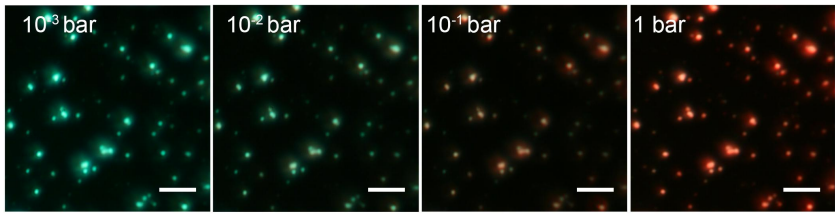

Figure 4.7 A large-area spectrally resolved image of a collection of individual DiB-NCs as a function of the O_2 pressure under 400 nm excitation (excitation fluence 7μJ/cm^2), showing a progressive change of the emission colour from green to red upon increasing the chamber pressure. The scale bar corresponds to 5μm.

The ratiometric sensing ability of individual DiB-NCs is demonstrated in Fig.4.7 and Fig.4.8, where Ishow confocal imaging and micro-PL data of isolated NCs (drop casted from a diluted hexane solution onto a quartz substrate with a nominal NC density of ~0.1/μm^2) as a function of the O_2 pressure. Upon raising the pressure from 10^{-3} bar to 1 bar, all NCs show a progressive transition in their emission colour from green, to orange, and then red, which is in perfect agreement with the results of ensemble measurements (Fig.4.6).

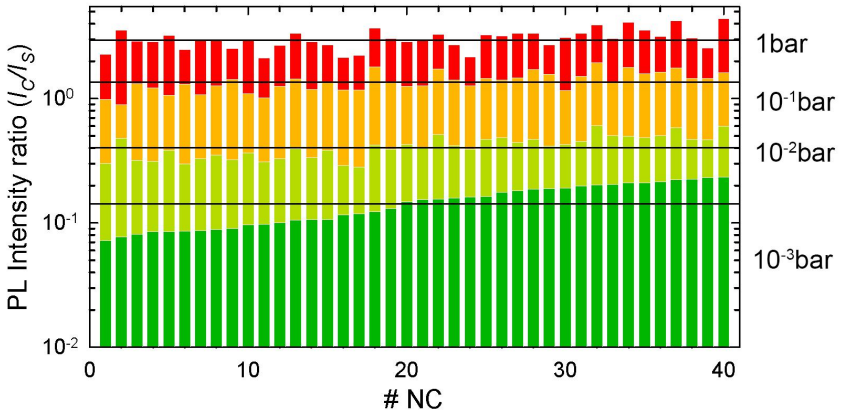

Figure 4.8 Histogram of the single-particle ratiometric response expressed as I_C/I_S for 40 individual NCs at the monitored oxygen pressures. The colour code resembles the total emission 10^{-3} bar, dark green; 10^{-2} bar, light green; 10^{-1} bar, orange; 1 bar, red. The mean values averaged across the whole NC population are indicated with black solid lines; the respective standard deviations are shown by grey shading.

Figure.4.8 reports the histogram of the I_C/I_S ratio for 40 individual DiB-NCs as a function of the chamber pressure, showing remarkable homogeneity of the ratiometric response across the NC population. This indicates that individual DiB-NCs can indeed be used as highly accurate nanoscale ratiometric pressure (or O_2) sensors. Importantly, the ratiometric sensing response I_C/I_S is independent of the total emission intensity, as highlighted in the correlation plot of I_C/I_S vs. (I_C+I_S) in Fig.4.9.

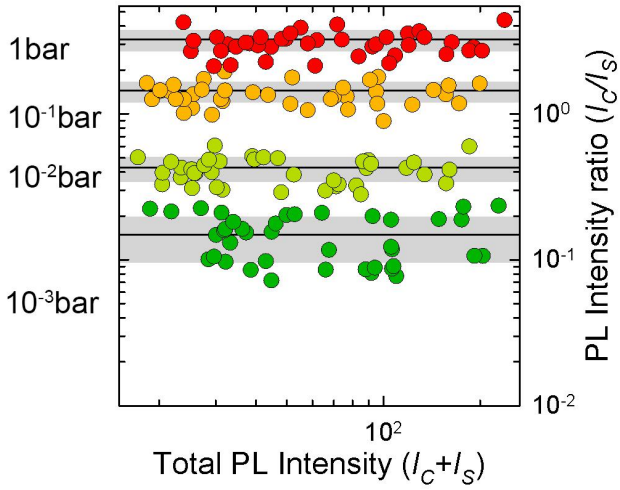

Figure 4.9 Correlation plot of the ratiometric sensing response IC/IS vs. the total PL intensity (I_C+I_S) at increasing O_2 pressure, indicating that the sensing response is independent of the total emission intensity. The colour code resembles the total emission 10^{-3} bar, dark green; 10^{-2} bar, light green; 10^{-1} bar, orange; 1 bar, red. The mean values averaged across the whole NC population are indicated with black solid lines; the respective standard deviations are shown by grey shading.

Photophysical mechanisms of the double sensing response

In order to gain a deeper insight into the photophysical mechanisms underpinning the ratiometric sensing response of DiB-NCs, Ihave measured the decay dynamics of both the shell and the core luminescence in a controlled atmosphere (Fig.4.10a,b).

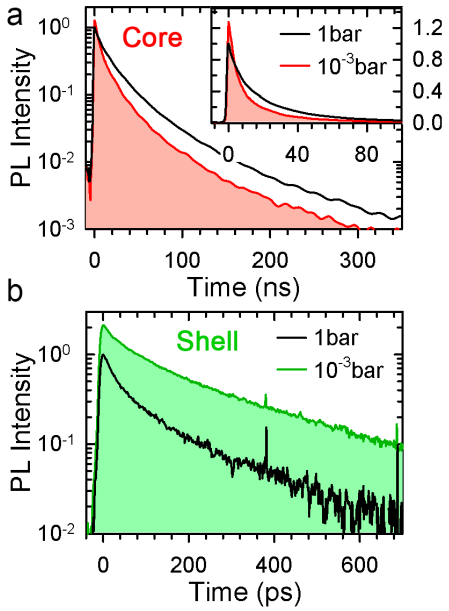

Figure 4.10 PL decay curves of (**a**) core and (**b**) shell emission measured at P=1 bar (red and green lines, respectively) and P=10^{-3} bar (black lines). The inset in 'a' reports the decay curve of the core PL using a linear scale to highlight the increase in the intensity at zero delay time as well as the accelerated decay exhibited at low O_2 pressure.

I start THE analysis with the reversed pressure response of the core luminescence, which is key for the realization of the "double sensing" regime. Examining the core time-resolved PL traces in Fig.4.9a can be noted a ~20% increase of the zero-delay PL intensity with decreasing pressure from 1 bar to 10^{-3} bar, which is accompanied by the acceleration of the decay dynamics. These are the typical spectroscopic signatures of the recombination of charged excitons (trions) consisting of a photoexcited electron-

hole pair and a pre-existing carrier (in the case of CdSe/CdS NCs it is predominantly an electron[190,208,209]) produced by photoionization[77,206]. In atmospheric conditions (Fig.4.11a), molecular oxygen continuously removes excess electrons thereby hindering the formation of negative trions. As a result, the spectroscopic behaviour of DiB-NCs is dominated by neutral excitons. If these excitons are core-localized they are virtually unaffected by surface species due to the protective effect of the ultra-thick CdS shell. Upon evacuation, the oxygen-driven "discharging" process is gradually suppressed, resulting in the formation of negative trions. These species are characterized by an increased emission rate (it is ideally twice that of a neutral exciton), which can explain the increase in the early time PL amplitude observed upon reducing the amount of oxygen in the sample chamber.

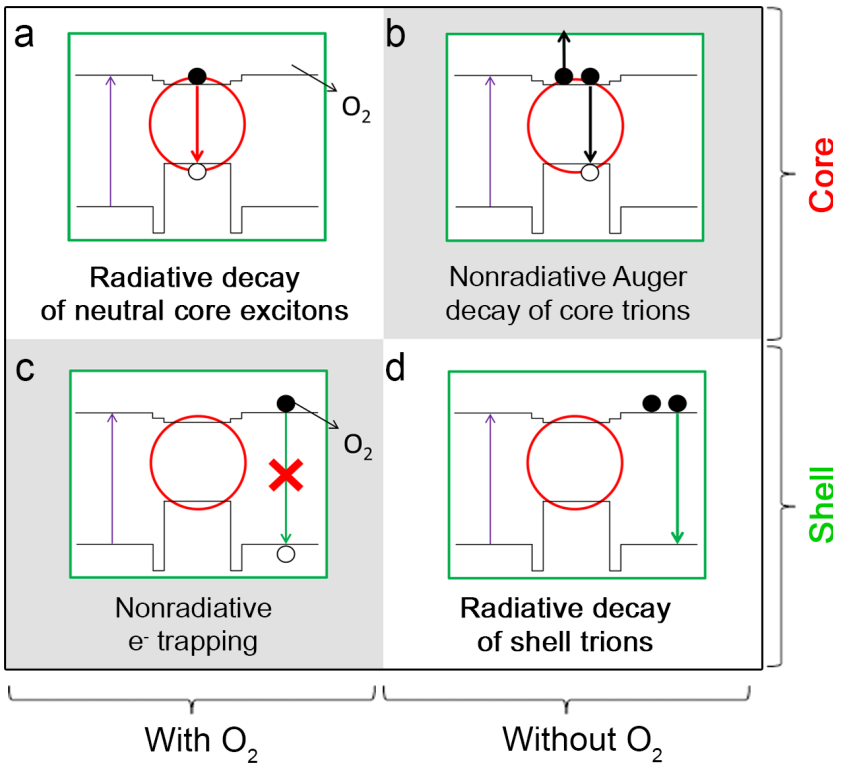

Figure 4.11 Schematics of the NC-O_2 interaction leading to the observed optical responses: In the presence of O_2 (**a**), neutral core excitons recombine radiatively, whilst (**c**) the shell-exciton decay is affected by nonradiative electron processes involving either direct electron extraction by O_2 molecules or trapping at surface defects depleted of electrons due to interactions with O_2. In the absence of O_2, enhanced availability of excess electrons makes nonradiative Auger decay the dominant recombination pathway for negatively charged core excitons (**b**), while shell excitons decay radiatively thanks to impeded electron capture by O_2 and suppressed Auger recombination (**d**); the latter is diminished due to a large volume of the shell. The regimes dominated by nonradiative recombination are highlighted by grey shading.

In addition, I observe the reduction of the PL lifetime, which is due to a combined effect of the enhanced radiative decay and the

activation of nonradiative Auger recombination. In DiB-NCs with a sharp core/shell interface, the Auger process is not as strongly suppressed as in graded or interfacially alloyed thick-shell CdSe/CdS NCs that could exhibit nearly unity trion PL quantum yields[210,211]. As a result, the dominant decay channel for the core PL in the absence of O_2 is nonradiative Auger recombination of negatively charged excitons (Fig.4.11b).

Next, I investigate the effect of O_2 on the shell-PL dynamics. Since the thickness of the CdS shell (8.5 nm) is greater than the exciton Bohr radius in CdS (5.6 nm), the shell excitons are bulk-like and hence are virtually unaffected by Auger recombination. The rate of Auger decay scales inversely with the particle volume and, therefore, is expected to be over 300 times lower than in the 1.5 nm CdSe core[212]. As a result, even in the case of access electrons, the nonradiative decay of shell excitons is primarily not due to Auger recombination, but still surface trapping (Fig.4.11c). Accordingly, upon lowering the chamber pressure, which is equivalent to raising the Fermi levels, leads to passivation of electron surface traps which is manifested in the strong increase of the zero delay PL intensity, accompanied by the extension of the PL lifetime (Fig.4.10b and Fig.4.11e). The resulting effect of these changes is the >300% enhancement of the emission intensity observed in cw measurements (Fig.4.4). This confirms that the shell-PL dynamics is dominated by activation/suppression of electron capture either directly by O_2 or electron-deficient surface traps. This further points to the co-existence of two trapping processes occurring on two different timescales: (*i*) ultrafast electron capture with the characteristic time unresolvable in our measurements with ~6 ps resolution (streak-camera detection), thereby modulating the zero-delay PL intensity without affecting its temporal dynamics, and (*ii*) a slower electron trapping channel competing with radiative recombination of shell excitons, whose progressive suppression at decreasing pressure leads to slower PL dynamics[186,213].

4.3 Conclusions

In conclusion, I have demonstrated the first example of a ratiometric O_2-sensing PSP based on a single type of two-colour emitter, that features (i) intrinsic ratiometric response at the single particle level, (ii) negligible overlap between the luminescence spectra of the reference and the sensor, (iii) enhanced sensitivity to O_2 partial pressure, and (iv) temperature-independent ratiometric behaviour. Due to the fact that the shell- and core-PL bands of the DiB-NCs exhibit trends of opposite directions in response to exposure to oxygen, these "double-sensor" r-PSPs demonstrate an enhanced pressure sensitivity with respect to that achievable with traditional reference-sensor pairs, where the reference channel is "neutral," i.e., not sensitive to O_2. Specifically, as a result of the direct exposure of shell excitons to the NC surfaces, the shell luminescence is strongly affected by effects of electron withdrawing by O_2, which leads to progressive emission quenching with increasing oxygen pressure. In direct contrast, the core PL is enhanced in the presence of oxygen which helps maintain NCs in the neutral state by removing extra-electrons that otherwise trigger fast nonradiative Auger recombination. As a result of these opposing trends, the ratiometric response of the NCs is largely amplified with respect to that achievable by monitoring the individual emissions of core and shell. The sensing response probed both at the ensemble and at the single-particle level using continuous and pulsed excitation is fully reproducible and unaffected by prolonged UV illumination. Finally, a nearly complete spectral separation between the core and the shell emission bands leads to no cross-readout between the two detection channels.

5 References

1 Tang, C. W. 2-LAYER ORGANIC PHOTOVOLTAIC CELL. *App. Phys. Lett.* **48**, 183-185, (1986).

2 Riede, M., Mueller, T., Tress, W., Schueppel, R. & Leo, K. Small-molecule solar cells—status and perspectives. *Nanotechnology* **19**, 424001, (2008).

3 Facchetti, A. Polymer donor-polymer acceptor (all-polymer) solar cells. *Mater. Today* **16**, 123-132, (2013).

4 Shrotriya, V. *et al.* Accurate measurement and characterization of organic solar cells. *Adv. Funct. Mater.* **16**, 2016-2023, (2006).

5 Cravino, A., Schilinsky, P. & Brabec, C. J. Characterization of organic solar cells: the importance of device layout. *Adv. Funct. Mater.* **17**, 3906-3910, (2007).

6 Ramsdale, C. M. *et al.* The origin of the open-circuit voltage in polyfluorene-based photovoltaic devices. *J. Appl. Phys.* **92**, 4266-4270, (2002).

7 Mihailetchi, V. D., Blom, P. W. M., Hummelen, J. C. & Rispens, M. T. Cathode dependence of the open-circuit voltage of polymer : fullerene bulk heterojunction solar cells. *J. Appl. Phys.* **94**, 6849-6854, (2003).

8 Brabec, C. J. *et al.* The influence of materials work function on the open circuit voltage of plastic solar cells. *Thin Solid Films* **403**, 368-372, (2002).

9 Brabec, C. J. *et al.* Origin of the open circuit voltage of plastic solar cells. *Adv. Funct. Mater.* **11**, 374-380, (2001).

10 Scharber, M. C. *et al.* Design rules for donors in bulk-heterojunction solar cells - Towards 10 % energy-conversion efficiency. *Adv. Mater.* **18**, 789-+, (2006).

11 Campoy-Quiles, M. *et al.* Morphology evolution via self-organization and lateral and vertical diffusion in polymer: fullerene solar cell blends. *Nat. Mater.* **7**, 158-164, (2008).

12 Mishra, A. & Bauerle, P. Small Molecule Organic Semiconductors on the Move: Promises for Future Solar Energy Technology. *Angew. Chem. Int. Ed.* **51**, 2020-2067, (2012).

13 Gunes, S., Neugebauer, H. & Sariciftci, N. S. Conjugated polymer-based organic solar cells. *Chem. Rev.* **107**, 1324-1338, (2007).

14 Chen, D. A., Nakahara, A., Wei, D. G., Nordlund, D. & Russell, T. P. P3HT/PCBM Bulk Heterojunction Organic Photovoltaics: Correlating Efficiency and Morphology. *Nano Lett.* **11**, 561-567, (2011).

15 Walker, B. *et al.* Nanoscale Phase Separation and High Photovoltaic Efficiency in Solution-Processed, Small-Molecule Bulk Heterojunction Solar Cells. *Adv. Funct. Mater.* **19**, 3063-3069, (2009).

16 Labram, J. G., Kirkpatrick, J., Bradley, D. D. C. & Anthopoulos, T. D. Impact of Fullerene Molecular Weight on P3HT:PCBM Microstructure Studied Using Organic Thin-Film Transistors. *Adv. Energy Mater.* **1**, 1176-1183, (2011).

17 Rand, B. P., Genoe, J., Heremans, P. & Poortmans, J. Solar cells utilizing small molecular weight organic semiconductors. *Prog. Photovoltaics* **15**, 659-676, (2007).

18 Kim, C. *et al.* Influence of Structural Variation on the Solid-State Properties of Diketopyrrolopyrrole-Based Oligophenylenethiophenes: Single-Crystal Structures, Thermal Properties, Optical Bandgaps, Energy Levels, Film Morphology, and Hole Mobility. *Chem. Mat.* **24**, 1699-1709, (2012).

19 Huang, Q. L. & Li, H. X. Recent progress of bulk heterojunction solar cells based on small-molecular donors. *Chin. Sci. Bull.* **58**, 2677-2685, (2013).

20 Chiu, S.-W. *et al.* A donor-acceptor-acceptor molecule for vacuum-processed organic solar cells with a power conversion efficiency of 6.4%. *Chem. Commun.* **48**, 1857-1859, (2012).

21 Tamayo, A. *et al.* Influence of alkyl substituents and thermal annealing on the film morphology and performance of solution processed, diketopyrrolopyrrole-based bulk heterojunction solar cells. *Energy Environ. Sci.* **2**, 1180-1186, (2009).

22 Feng, H. & Luping, Y. How far can polymer solar cells go? In need of a synergistic approach. *J. Phys. Chem. Lett.* **2**, 3102-3113, (2011).

23 Shieh, J. T. *et al.* The effect of carrier mobility in organic solar cells. *J. Appl. Phys.* **107**, (2010).

24 Coropceanu, V. *et al.* Charge transport in organic semiconductors. *Chem. Rev.* **107**, 926-952, (2007).

25 Hertel, D. & Baessler, H. Photoconduction in amorphous organic solids. *Chemphyschem* **9**, 666-688, (2008).

26 Grancini, G. *et al.* Transient Absorption Imaging of P3HT:PCBM Photovoltaic Blend: Evidence For Interfacial Charge Transfer State. *J. Phys. Chem. Lett.* **2**, 1099-1105, (2011).

27 Bredas, J.-L., Norton, J. E., Cornil, J. & Coropceanu, V. Molecular Understanding of Organic Solar Cells: The Challenges. *Acc. Chem. Res.* **42**, 1691-1699, (2009).

28 Moses, D. Organic photovoltaics Efficient relaxation. *Nat. Mater.* **13**, 4-5, (2014).

29 Vandewal, K. *et al.* Efficient charge generation by relaxed charge-transfer states at organic interfaces. *Nat. Mater.* **13**, 63-68, (2014).

30 Wei, G. D., Wang, S. Y., Renshaw, K., Thompson, M. E. & Forrest, S. R. Solution-Processed Squaraine Bulk Heterojunction Photovoltaic Cells. *ACS Nano* **4**, 1927-1934, (2010).

31 Hoppe, H. & Sariciftci, N. S. Morphology of polymer/fullerene bulk heterojunction solar cells. *J. Mater. Chem.* **16**, 45-61, (2006).

32 Morteani, A. C., Friend, R. H. & Silva, C. Exciton trapping at heterojunctions in polymer blends. *J. Chem. Phys.* **122**, (2005).

33 Campbell, A. R. *et al.* Low-Temperature Control of Nanoscale Morphology for High Performance Polymer Photovoltaics. *Nano Lett.* **8**, 3942-3947, (2008).

34 Moon, J. S., Takacs, C. J., Sun, Y. & Heeger, A. J. Spontaneous Formation of Bulk Heterojunction Nanostructures: Multiple Routes to Equivalent Morphologies. *Nano Lett.* **11**, 1036-1039, (2011).

35 Wang, H. Y. *et al.* Ordered fibrillar morphology of donor-acceptor conjugated copolymers at multiple scales via blending with flexible polymers and solvent vapor annealing: insight into photophysics and mechanism. *Phys. Chem. Chem. Phys.* **16**, 1441-1450, (2014).

36 Kim, J. S. *et al.* Performance Optimization of Polymer Solar Cells Using Electrostatically Sprayed Photoactive Layers. *Adv. Funct. Mater.* **20**, 3538-3546, (2010).

37 Tsoi, W. C. *et al.* In-situ monitoring of molecular vibrations of two organic semiconductors in photovoltaic blends and their impact on thin film morphology. *App. Phys. Lett.* **102**, (2013).

38 Lee, J. K. *et al.* Processing additives for improved efficiency from bulk heterojunction solar cells. *J. Am. Chem. Soc.* **130**, 3619-3623, (2008).

39 Fan, H. J., Shang, H. X., Li, Y. F. & Zhan, X. W. Efficiency enhancement in small molecule bulk heterojunction organic solar cells via additive. *App. Phys. Lett.* **97**, (2010).

40 Palermo, V. & Samori, P. Molecular self-assembly across multiple length scales. *Angew. Chem. Int. Ed.* **46**, 4428-4432, (2007).

41 Piris, J. *et al.* Anisotropy in the mobility and photogeneration of charge carriers in thin films of discotic hexabenzocoronenes, columnarly self-assembled on friction-deposited poly(tetrafluoroethylene). *Adv. Mater.* **15**, 1736-+, (2003).

42 Spencer, S. D. *et al.* The effect of controllable thin film crystal growth on the aggregation of a novel high panchromaticity squaraine viable for organic solar cells. *Sol. Energ. Mat. Sol. Cells* **112**, 202-208, (2013).

43 Zambounis, J. S., Hao, Z. & Iqbal, A. Latent pigments activated by heat. *Nature* **388**, 131-132, (1997).

44 Ichimura, K., Arimitsu, K. & Tahara, M. Photoacid-catalysed pigmentation of dyestuff precursors enhanced by acid amplifiers in polymer films. *J. Mater. Chem.* **14**, 1164-1172, (2004).

45 Glowacki, E. D. *et al.* Hydrogen-Bonded Semiconducting Pigments for Air-Stable Field-Effect Transistors. *Adv. Mater.* **25**, 1563-1569, (2013).

46 Lee, J. *et al.* Solution-Processable Ambipolar Diketopyrrolopyrrole–Selenophene Polymer with Unprecedentedly High Hole and Electron Mobilities. *J. Am. Chem. Soc.* **134**, 20713-20721, (2012).

47 Suna, Y., Nishida, J.-i., Fujisaki, Y. & Yamashita, Y. Ambipolar Behavior of Hydrogen-Bonded Diketopyrrolopyrrole–Thiophene Co-oligomers Formed from Their Soluble Precursors. *Org. Lett.* **14**, 3356-3359, (2012).

48 Yanagisawa, H., Mizuguchi, J., Aramaki, S. & Sakai, Y. Organic field-effect transistor devices based on latent pigments of unsubstituted diketopyrrolopyrrole or quinacridone. *Jpn. J. Appl. Phys.* **47**, 4728-4731, (2008).

49 Tamayo, A. B., Walker, B. & Nguyen, T.-Q. A low band gap, solution processable oligothiophene with a diketopyrrolopyrrole core for use in organic solar cells. *J. Phys. Chem. C* **112**, 11545-11551, (2008).

50 Qu, S. Y. & Tian, H. Diketopyrrolopyrrole (DPP)-based materials for organic photovoltaics. *Chem. Commun.* **48**, 3039-3051, (2012).

51 Ripaud, E. *et al.* Structure-properties relationships in conjugated molecules based on diketopyrrolopyrrole for organic photovoltaics. *Dyes Pigments* **95**, 126-133, (2012).

52 Stas, S. *et al.* Straightforward access to diketopyrrolopyrrole (DPP) dimers. *Dyes Pigments* **97**, 198-208, (2013).

53 Glowacki, E. D. *et al.* A facile protection-deprotection route for obtaining indigo pigments as thin films and their applications in organic bulk heterojunctions. *Chem. Commun.* **49**, 6063-6065, (2013).

54 Li, X. *et al.* Dual Plasmonic Nanostructures for High Performance Inverted Organic Solar Cells. *Adv. Mater.* **24**, 3046-3052, (2012).

55 Lakowicz, J. *Principles of Fluorescence Spectroscopy*. 3rd edn, (2006).

56 Hao, Z. W., O. Solid solutions of 1,4-diketopyrrolopyrroles.

57 Lanzarini, E. *et al.* Polymer-Based Photocatalytic Hydrogen Generation. *J. Phys. Chem. C* **116**, 10944-10949, (2012).

58 Suppes, G., Ballard, E. & Holdcroft, S. Aqueous photocathode activity of regioregular poly(3-hexylthiophene). *Polym. Chem.* **4**, 5345-5350, (2013).

59 Guerrero, A. *et al.* Organic photoelectrochemical cells with quantitative photocarrier conversion. *Energy Environ. Sci.* **7**, 3666-3673, (2014).

60 Bourgeteau, T. *et al.* A H_2-evolving photocathode based on direct sensitization of MoS_3 with an organic photovoltaic cell. *Energy Environ. Sci.* **6**, 2706-2713, (2013).

61 Hin Ng, C., Winther-Jensen, O., Ohlin, C. A. & Winther-Jensen, B. Exploration and optimisation of poly(2,2'-bithiophene) as a stable photo-electrocatalyst for hydrogen production. *J. Mater. Chem. A* **3**, 11358-11366, (2015).

62 Xia, Y., Xie, W., Ruden, P. P. & Frisbie, C. D. Carrier Localization on Surfaces of Organic Semiconductors Gated with Electrolytes. *Phys. Rev. Lett.* **105**, 036802, (2010).

63 Gautam, V., Bag, M. & Narayan, K. S. Dynamics of Bulk Polymer Heterostructure/Electrolyte Devices. *J. Phys. Chem. Lett.* **1**, 3277-3282, (2010).

64 Khodagholy, D. *et al.* In vivo recordings of brain activity using organic transistors. *Nat. Commun.* **4**, 1575, (2013).

65 Toffanin, S. *et al.* N-type perylene-based organic semiconductors for functional neural interfacing. *J. Mater. Chem. B* **1**, 3850-3859, (2013).

66 Martino, N., Ghezzi, D., Benfenati, F., Lanzani, G. & Antognazza, M. R. Organic semiconductors for artificial vision. *J. Mater. Chem. B* **1**, 3768-3780, (2013).

67 Ghezzi, D. *et al.* A hybrid bioorganic interface for neuronal photoactivation. *Nat Commun* **2**, 166, (2011).

68 Ghezzi, D. *et al.* A polymer optoelectronic interface restores light sensitivity in blind rat retinas. *Nat Photon* **7**, 400-406, (2013).

69 Gautam, V., Rand, D., Hanein, Y. & Narayan, K. S. A Polymer Optoelectronic Interface Provides Visual Cues to a Blind Retina. *Adv. Mater.* **26**, 1751-1756, (2014).

70 Benfenati, V. *et al.* A transparent organic transistor structure for bidirectional stimulation and recording of primary neurons. *Nat. Mater.* **12**, 672-680, (2013).

71 Martino, N. *et al.* Photothermal cellular stimulation in functional bio-polymer interfaces. *Sci. Rep.* **5**, 1-8, (2015).

72 Zhuo, J.-M. *et al.* Direct Spectroscopic Evidence for a Photodoping Mechanism in Polythiophene and Poly(bithiophene-alt-thienothiophene) Organic Semiconductor Thin Films Involving Oxygen and Sorbed Moisture. *Adv. Mater.* **21**, 4747-4752, (2009).

73 Norrman, K., Gevorgyan, S. A. & Krebs, F. C. Water-Induced Degradation of Polymer Solar Cells Studied by $H_2{}^{18}O$ Labeling. *ACS Appl. Mater. Interfaces* **1**, 102-112, (2009).

74 Volonakis, G., Tsetseris, L. & Logothetidis, S. Impurity-related effects in poly(3-hexylthiophene) crystals. *Phys. Chem. Chem. Phys.* **16**, 25557-25563, (2014).

75 Brovelli, S. *et al.* Dual-Color Electroluminescence from Dot-in-Bulk Nanocrystals. *Nano Lett.* **14**, 486-494, (2014).

76 Galland, C. *et al.* Dynamic Hole Blockade Yields Two-Color Quantum and Classical Light from Dot-in-Bulk Nanocrystals. *Nano Lett.* **13**, 321-328, (2013).

77 Brovelli, S. *et al.* Electrochemical Control of Two-Color Emission from Colloidal Dot-in-Bulk Nanocrystals. *Nano Letters* **14**, 3855-3863, (2014).

78 Busa, W. B. & Nuccitelli, R. Metabolic regulation via intracellular pH. *Am. J. Physiol.* **246**, R409-438, (1984).

79 Casey, J. R., Grinstein, S. & Orlowski, J. Sensors and regulators of intracellular pH. *Nat. Rev. Mol. Cell. Biol.* **11**, 50-61, (2010).

80 Lagadic-Gossmann, D., Huc, L. & Lecureur, V. Alterations of intracellular pH homeostasis in apoptosis: origins and roles. *Cell Death Differ.* **11**, 953-961, (2004).

81 Wang, H. Y. & Oster, G. Energy transduction in the F-1 motor of ATP synthase. *Nature* **396**, 279-282, (1998).

82 Cardone, R. A., Casavola, V. & Reshkin, S. J. The role of disturbed pH dynamics and the Na+/H+ exchanger in metastasis. *Nat. Rev. Cancer.* **5**, 786-795, (2005).

83 Griffiths, J. R. Are cancer cells acidic? *Br. J. Cancer* **64**, 425-427, (1991).

84 Harguindey, S., Orive, G., Luis Pedraz, J., Paradiso, A. & Reshkin, S. J. The role of pH dynamics and the Na+/H+ antiporter in the etiopathogenesis and treatment of cancer. Two faces of the same coin--one single nature. *Biochim. Biophys. Acta* **1756**, 1-24, (2005).

85 Perona, R. & Serrano, R. Increased pH and tumorigenicity of fibroblasts expressing a yeast proton pump. *Nature* **334**, 438-440, (1988).

86 Tannock, I. F. & Rotin, D. Acid pH in Tumors and Its Potential for Therapeutic Exploitation. *Cancer Res.* **49**, 4373-4384, (1989).

87 Day, S. M. *et al.* Histidine button engineered into cardiac troponin I protects the ischemic and failing heart. *Nat. Med.* **12**, 181-189, (2006).

88 Obara, M., Szeliga, M. & Albrecht, J. Regulation of pH in the mammalian central nervous system under normal and pathological conditions: facts and hypotheses. *Neurochem. Int.* **52**, 905-919, (2008).

89 Sánchez-Armáss, S., Sennoune, S. R., Maiti, D., Ortega, F. & Martínez-Zaguilán, R. Spectral imaging microscopy demonstrates cytoplasmic pH oscillations in glial cells. *Am. J. Physiol.* **290**, C524-C538, (2006).

90 Vaughan-Jones, R. D., Spitzer, K. W. & Swietach, P. Intracellular pH regulation in heart. *J. Mol. Cell. Cardiol.* **46**, 318-331, (2009).

91 Hilderbrand, S. A., Kelly, K. A., Niedre, M. & Weissleder, R. Near Infrared Fluorescence-Based Bacteriophage Particles for Ratiometric pH Imaging. *Bioconjugate Chem.* **19**, 1635-1639, (2008).

92 Li, L., Li, Z., Shi, W., Li, X. & Ma, H. Sensitive and Selective Near-Infrared Fluorescent Off–On Probe and Its Application to Imaging Different Levels of β-Lactamase inStaphylococcus aureus. *Anal. Chem.* **86**, 6115-6120, (2014).

93 Tang, B. *et al.* A Near-Infrared Neutral pH Fluorescent Probe for Monitoring Minor pH Changes: Imaging in Living HepG2 and HL-7702 Cells. *J. Am. Chem. Soc.* **131**, 3016-3023, (2009).

94 Chen, L. *et al.* A novel pH "off-on" fluorescent probe for lysosome imaging. *RSC Adv.* **3**, 13412-13416, (2013).

95 Tian, Y. *et al.* A series of naphthalimide derivatives as intra and extracellular pH sensors. *Biomaterials* **31**, 7411-7422, (2010).

96 Pietryga, J. M. *et al.* Spectroscopic and Device Aspects of Nanocrystal Quantum Dots. *Chemical Reviews* **116**, 10513-10622, (2016).

97 Kovalenko, M. V. *et al.* Prospects of nanoscience with nanocrystals. *ACS nano* **9**, 1012-1057, (2015).

98 Boles, M. A., Ling, D., Hyeon, T. & Talapin, D. V. The surface science of nanocrystals. *Nat Mater* **15**, 141-153, (2016).

99 Gao, X. H., Chan, W. C. W. & Nie, S. M. Quantum-dot nanocrystals for ultrasensitive biological labeling and multicolor optical encoding. *J. Biomed. Opt.* **7**, 532-537, (2002).

100 Ji, X. *et al.* On the pH-Dependent Quenching of Quantum Dot Photoluminescence by Redox Active Dopamine. *J. Am. Chem. Soc.* **134**, 6006-6017, (2012).

101 Kaur, G. & Tripathi, S. K. Size tuning of MAA capped CdSe and CdSe/CdS quantum dots and their stability in different pH environments. *Mater. Chem. Phys.* **143**, 514-523, (2014).

102 Ma, J. *et al.* Photostability of thiol-capped CdTe quantum dots in living cells: the effect of photo-oxidation. *Nanotechnology* **17**, 2083-2089, (2006).

103 Deng, Z., Zhang, Y., Yue, J., Tang, F. & Wei, Q. Green and orange CdTe quantum dots as effective pH-sensitive fluorescent probes for dual simultaneous and independent detection of viruses. *J. Phys. Chem. B* **111**, 12024-12031, (2007).

104 Lakowicz, J. R. *Principles of fluorescence spectroscopy*. (Springer, 2010).

105 Maroto, A., Balasubramanian, K., Burghard, M. & Kern, K. Functionalized Metallic Carbon Nanotube Devices for pH Sensing. *ChemPhysChem* **8**, 220-223, (2007).

106 Medintz, I. L., Uyeda, H. T., Goldman, E. R. & Mattoussi, H. Quantum dot bioconjugates for imaging, labelling and sensing. *Nat. Mater.* **4**, 435-446, (2005).

107 Michalet, X. *et al.* Quantum Dots for Live Cells, in Vivo Imaging, and Diagnostics. *Science* **307**, 538-544, (2005).

108 Panda, B. R. & Chattopadhyay, A. A water-soluble polythiophene–Au nanoparticle composite for pH sensing. *J. Colloid Interface Sci.* **316**, 962-967, (2007).

109 Allard, E. & Larpent, C. Core-shell type dually fluorescent polymer nanoparticles for ratiometric pH-sensing. *J. Polym. Sci. A Polym.* **46**, 6206-6213, (2008).

110 Burns, A., Ow, H. & Wiesner, U. Fluorescent core-shell silica nanoparticles: towards "Lab on a Particle" architectures for nanobiotechnology. *Chem. Soc. Rev.* **35**, 1028, (2006).

111 Burns, A., Sengupta, P., Zedayko, T., Baird, B. & Wiesner, U. Core/Shell Fluorescent Silica Nanoparticles for Chemical Sensing: Towards Single-Particle Laboratories. *Small* **2**, 723-726, (2006).

112 Chen, Y.-N. *et al.* One-pot synthesis of fluorescent BSA–Ce/Au nanoclusters as ratiometric pH probes. *Chem. Commun.* **50**, 8571, (2014).

113 Peng, H.-s., Stolwijk, J. A., Sun, L.-N., Wegener, J. & Wolfbeis, O. S. A Nanogel for Ratiometric Fluorescent Sensing of Intracellular pH Values. *Angew. Chem. Int. Ed.* **49**, 4246-4249, (2010).

114 Wang, X.-d., Meier, R. J. & Wolfbeis, O. S. A Fluorophore-Doped Polymer Nanomaterial for Referenced Imaging of pH and Temperature with Sub-Micrometer Resolution. *Adv. Funct. Mater.* **22**, 4202-4207, (2012).

115 Shi, W., Li, X. H. & Ma, H. M. Fluorescent probes and nanoparticles for intracellular sensing of pH values. *Methods Appl. Fluoresc.* **2**, (2014).

116 Chen, S. *et al.* Full-Range Intracellular pH Sensing by an Aggregation-Induced Emission-Active Two-Channel Ratiometric Fluorogen. *J. Am. Chem. Soc.* **135**, 4926-4929, (2013).

117 Miesenbock, G., De Angelis, D. A. & Rothman, J. E. Visualizing secretion and synaptic transmission with pH-sensitive green fluorescent proteins. *Nature* **394**, 192-195, (1998).

118 Niu, C.-G. *et al.* Fluorescence ratiometric pH sensor prepared from covalently immobilized porphyrin and benzothioxanthene. *Anal. Bioanal. Chem.* **383**, 349-357, (2005).

119 Venn, A. A. *et al.* Imaging intracellular pH in a reef coral and symbiotic anemone. *Proc. Natl. Acad. Sci.* **106**, 16574-16579, (2009).

120 Medintz, I. L. *et al.* Quantum-dot/dopamine bioconjugates function as redox coupled assemblies for in vitro and intracellular pH sensing. *Nat. Mater.* **9**, 676-684, (2010).

121 Paek, K., Yang, H., Lee, J., Park, J. & Kim, B. J. Efficient Colorimetric pH Sensor Based on Responsive Polymer–Quantum Dot Integrated Graphene Oxide. *ACS Nano*, (2014).

122 Snee, P. T. *et al.* A Ratiometric CdSe/ZnS Nanocrystal pH Sensor. *J. Am. Chem. Soc.* **128**, 13320-13321, (2006).

123 Suzuki, M., Husimi, Y., Komatsu, H., Suzuki, K. & Douglas, K. T. Quantum dot FRET Biosensors that respond to pH, to proteolytic or nucleolytic cleavage, to DNA synthesis, or to a

multiplexing combination. *J. Am. Chem. Soc.* **130**, 5720-5725, (2008).

124 Tomasulo, M., Yildiz, I. & Raymo, F. M. pH-Sensitive quantum dots. *J. Phys. Chem. B* **110**, 3853-3855, (2006).

125 Dennis, A. M., Rhee, W. J., Sotto, D., Dublin, S. N. & Bao, G. Quantum Dot–Fluorescent Protein FRET Probes for Sensing Intracellular pH. *ACS Nano* **6**, 2917-2924, (2012).

126 Jin, T., Sasaki, A., Kinjo, M. & Miyazaki, J. A quantum dot-based ratiometric pH sensor. *Chem. Commun.* **46**, 2408, (2010).

127 Shi, W., Li, X. & Ma, H. A Tunable Ratiometric pH Sensor Based on Carbon Nanodots for the Quantitative Measurement of the Intracellular pH of Whole Cells. *Angew. Chem. Int. Ed.* **51**, 6432-6435, (2012).

128 Pinchetti, V. *et al.* Effect of Core/Shell Interface on Carrier Dynamics and Optical Gain Properties of Dual-Color Emitting CdSe/CdS Nanocrystals. *ACS Nano*, (2016).

129 Wong, J. I. *et al.* Dual Wavelength Electroluminescence from CdSe/CdS Tetrapods. *ACS Nano* **8**, 2873-2879, (2014).

130 Soni, U. *et al.* Simultaneous Type-I/Type-II Emission from CdSe/CdS/ZnSe Nano-Heterostructures. *ACS Nano* **8**, 113-123, (2014).

131 Lin, Q. *et al.* Design and Synthesis of Heterostructured Quantum Dots with Dual Emission in the Visible and Infrared. *ACS Nano* **9**, 539-547, (2015).

132 Liu, S., Borys, N. J., Sapra, S., Eychmüller, A. & Lupton, J. M. Localization and Dynamics of Long-Lived Excitations in Colloidal Semiconductor Nanocrystals with Dual Quantum Confinement. *ChemPhysChem* **16**, 1663-1669, (2015).

133 Battaglia, D., Blackman, B. & Peng, X. Coupled and decoupled dual quantum systems in one semiconductor nanocrystal. *J. Am. Chem. Soc.* **127**, 10889-10897, (2005).

134 Nizamoglu, S. *et al.* Dual-color emitting quantum-dot-quantum-well CdSe-ZnS heteronanocrystals hybridized on InGaN⁄GaN light emitting diodes for high-quality white light generation. *Applied Physics Letters* **92**, 113110, (2008).

135 Sapra, S., Mayilo, S., Klar, T. A., Rogach, A. L. & Feldmann, J. Bright White-Light Emission from Semiconductor Nanocrystals: by Chance and by Design. *Advanced Materials* **19**, 569-572, (2007).

136 Teitelboim, A. & Oron, D. Broadband Near-Infrared to Visible Upconversion in Quantum Dot–Quantum Well Heterostructures. *ACS Nano*, (2015).

137 Zhao, H., Vomiero, A. & Rosei, F. Ultrasensitive, Biocompatible, Self-Calibrating, Multiparametric Temperature Sensors. *Small* **11**, 5741-5746, (2015).

138 Zhao, H. *et al.* Dual emission in asymmetric "giant" PbS/CdS/CdS core/shell/shell quantum dots. *Nanoscale*, (2016).

139 Mosconi, E. *et al.* Surface Polarization Drives Photoinduced Charge Separation at the P3HT/Water Interface. *ACS Energy Letters* **1**, 454-463, (2016).

140 Yu, W. W., Qu, L., Guo, W. & Peng, X. Experimental Determination of the Extinction Coefficient of CdTe, CdSe, and CdS Nanocrystals. *Chem. Mater.* **15**, 2854-2860, (2003).

141 Fox, C. H., Johnson, F. B., Whiting, J. & Roller, P. P. Formaldehyde Fixation. *J. Histochem. Cytochem.* **33**, 845-853, (1985).

142 Mariani, M. M., Lampen, P., Popp, J., Wood, B. R. & Deckert, V. Impact of fixation on in vitro cell culture lines monitored with Raman spectroscopy. *Analyst* **134**, 1154-1161, (2009).

143 Meade, A. D. *et al.* Studies of chemical fixation effects in human cell lines using Raman microspectroscopy. *Anal. Bioanal. Chem.* **396**, 1781-1791, (2010).

144 Schnell, U., Dijk, F., Sjollema, K. A. & Giepmans, B. N. G. Immunolabeling artifacts and the need for live-cell imaging. *Nat. Methods* **9**, 152-158, (2012).

145 Williams, Y. *et al.* Comparison of three cell fixation methods for high content analysis assays using quantum dots. *J. Microsc.* **232**, 91-98, (2008).

146 Chudzik, J., Ohkuma, S. & Poole, B. The effects of basic substances and acidic ionophores on the digestion of

exogenous and endogenous proteins in mouse peritoneal macrophages. *J. Cell. Biol.* **102**, 959-966, (1986).

147 Gerlier, D. & Thomasset, N. Use of MTT colorimetric assay to measure cell activation. *Journal of Immunological Methods* **94**, 57-63, (1986).

148 Mosmann, T. Rapid colorimetric assay for cellular growth and survival: Application to proliferation and cytotoxicity assays. *Journal of Immunological Methods* **65**, 55-63, (1983).

149 Liu, Y.-S. *et al.* pH-Sensitive Photoluminescence of CdSe/ZnSe/ZnS Quantum Dots in Human Ovarian Cancer Cells. *J. Phys. Chem. C* **111**, 2872-2878, (2007).

150 Kolny-Olesiak, J. & Weller, H. Synthesis and application of colloidal CuInS2 semiconductor nanocrystals. *ACS applied materials & interfaces* **5**, 12221-12237, (2013).

151 Liu, T. & Sullivan, J. (Springer, Berlin, 2005).

152 Wolfbeis, O. S. Sensor Paints. *Advanced Materials* **20**, 3759-3763, (2008).

153 Disotell, K. *et al.* Single-shot temperature- and pressure-sensitive paint measurements on an unsteady helicopter blade. *Exp Fluids* **55**, 1-15, (2014).

154 Gregory, J. W., Sakaue, H., Liu, T. & Sullivan, J. P. Fast Pressure-Sensitive Paint for Flow and Acoustic Diagnostics. *Annual Review of Fluid Mechanics* **46**, 303-330, (2014).

155 Gregory, J. W., Sullivan, J. P., Raman, G. & Raghu, S. Characterization of the Microfluidic Oscillator. *AIAA Journal* **45**, 568-576, (2007).

156 Nagai, H., Naraoka, R., Sawada, K. & Asai, K. Pressure-Sensitive Paint Measurement of Pressure Distribution in a Supersonic Micronozzle. *AIAA Journal* **46**, 215-222, (2008).

157 Niimi, T. *et al.* Application of pressure-sensitive paints to low-pressure range. *Journal of thermophysics and heat transfer* **19**, 9-16, (2005).

158 Gregory, J., Sullivan, J., Sakaue, H. & Huang, C. Y. in *40th AIAA Aerospace Sciences Meeting & Exhibit Aerospace Sciences Meetings* (American Institute of Aeronautics and Astronautics, 2002).

159 Dickert, F. L., Besenböck, H. & Tortschanoff, M. Molecular Imprinting Through van der Waals Interactions: Fluorescence Detection of PAHs in Water. *Advanced Materials* **10**, 149-151, (1998).

160 Frederiksen, M. S. & Glud, R. N. Oxygen dynamics in the rhizosphere of Zostera marina: A two-dimensional planar optode study. *Limnology and Oceanography* **51**, 1072-1083, (2006).

161 Sánchez-Barragán, I., Costa-Fernández, J. M., Sanz-Medel, A., Valledor, M. & Campo, J. C. Room-temperature phosphorescence (RTP) for optical sensing. *Trends in Analytical Chemistry* **25**, 958-967, (2006).

162 Babilas, P. *et al.* In Vivo Phosphorescence Imaging of pO2 Using Planar Oxygen Sensors. *Microcirculation* **12**, 477-487, (2005).

163 Wu, M., Lin, Z., Schäferling, M., Dürkop, A. & Wolfbeis, O. S. Fluorescence imaging of the activity of glucose oxidase using a hydrogen-peroxide-sensitive europium probe. *Analytical Biochemistry* **340**, 66-73, (2005).

164 Amao, Y., Ishikawa, Y. & Okura, I. Green luminescent iridium(III) complex immobilized in fluoropolymer film as optical oxygen-sensing material. *Analytica Chimica Acta* **445**, 177-182, (2001).

165 Sakaue, H., Miyamoto, K. & Miyazaki, T. A motion-capturing pressure-sensitive paint method. *Journal of Applied Physics* **113**, 084901, (2013).

166 Mosser, V., Suski, J., Goss, J. & Obermeier, E. Piezoresistive pressure sensors based on polycrystalline silicon. *Sensors and Actuators A: Physical* **28**, 113-132, (1991).

167 Li, M., Wang, M. & Li, H. Optical MEMS pressure sensor based on Fabry-Perot interferometry. *Opt. Express* **14**, 1497-1504, (2006).

168 Bell, J. H., Schairer, E. T., Hand, L. A. & Mehta, R. D. Surface pressure measurements using luminescent coatings 1. *Annual Review of Fluid Mechanics* **33**, 155-206, (2001).

169 Khalil, G. E. *et al.* Dual-luminophor pressure-sensitive paint: I. Ratio of reference to sensor giving a small temperature

dependency. *Sensors and Actuators B: Chemical* **97**, 13-21, (2004).

170 Amao, Y., Miyashita, T. & Okura, I. Novel optical oxygen sensing material: platinum octaethylporphyrin immobilized in a copolymer film of isobutyl methacrylate and tetrafluoropropyl methacrylate. *React. Funct. Polym.* **47**, 49-54, (2001).

171 Basu, B. J., Anandan, C. & Rajam, K. S. Study of the mechanism of degradation of pyrene-based pressure sensitive paints. *Sensors and Actuators B: Chemical* **94**, 257-266, (2003).

172 Demas, J. N. & DeGraff, B. A. in *Topics in Fluorescence Spectroscopy* Vol. 4 (ed Joseph R. Lakowicz) Ch. 4, 71-107 (Springer US, 1994).

173 Liu, T., Guille, M. & Sullivan, J. P. Accuracy of Pressure-Sensitive Paint. *AIAA Journal* **39**, 103-112, (2001).

174 Yasuhiro, E. & Keisuke, A. in *22nd AIAA Aerodynamic Measurement Technology and Ground Testing Conference Fluid Dynamics and Co-located Conferences* (American Institute of Aeronautics and Astronautics, 2002).

175 Gregory, J. W., Asai, K., Kameda, M., Liu, T. & Sullivan, J. P. A review of pressure-sensitive paint for high-speed and unsteady aerodynamics. *Proceedings of the Institution of Mechanical Engineers, Part G: Journal of Aerospace Engineering* **222**, 249-290, (2008).

176 Bell, J. H. in *Instrumentation in Aerospace Simulation Facilities, 2001. 19th International Congress on ICIASF 2001.* 5-16.

177 Borisov, S. M., Vasylevska, A. S., Krause, C. & Wolfbeis, O. S. Composite Luminescent Material for Dual Sensing of Oxygen and Temperature. *Adv. Funct. Mater.* **16**, 1536-1542, (2006).

178 Stich, M. I. J., Nagl, S., Wolfbeis, O. S., Henne, U. & Schaeferling, M. A Dual Luminescent Sensor Material for Simultaneous Imaging of Pressure and Temperature on Surfaces. *Adv. Funct. Mater.* **18**, 1399-1406, (2008).

179 Köse, M. E., Omar, A., Virgin, C. A., Carroll, B. F. & Schanze, K. S. Principal Component Analysis Calibration Method for Dual-Luminophore Oxygen and Temperature Sensor Films: Application to Luminescence Imaging. *Langmuir* **21**, 9110-9120, (2005).

180 García-Santamaría, F. *et al.* Suppressed Auger Recombination in Giant Nanocrystals Boosts Optical Gain Performance. *Nano Letters* **9**, 3482-3488, (2009).

181 Klimov, V. I. *et al.* Optical Gain and Stimulated Emission in Nanocrystal Quantum Dots. *Science* **290**, 314-317, (2000).

182 Pal, B. N. *et al.* 'Giant' CdSe/CdS Core/Shell Nanocrystal Quantum Dots As Efficient Electroluminescent Materials: Strong Influence of Shell Thickness on Light-Emitting Diode Performance. *Nano Letters* **12**, 331-336, (2011).

183 Shirasaki, Y., Supran, G. J., Bawendi, M. G. & Bulovic, V. Emergence of colloidal quantum-dot light-emitting technologies. *Nat Photon* **7**, 13-23, (2013).

184 Wan Ki Bae, S. B. a. V. I. K. Spectroscopic insights into the performance of quantum dot light-emitting diodes. *MRS Bulletin* **38**, 721-730, (2013).

185 Ho, Y.-P. & Leong, K. W. Quantum dot-based theranostics. *Nanoscale* **2**, 60-68, (2010).

186 Lorenzon, M. *et al.* Reversed oxygen sensing using colloidal quantum wells towards highly emissive photoresponsive varnishes. *Nat Commun* **6**, (2015).

187 Feng, Y., Cheng, J., Zhou, L., Zhou, X. & Xiang, H. Ratiometric optical oxygen sensing: a review in respect of material design. *The Analyst* **137**, 4885-4901, (2012).

188 Brovelli, S. *et al.* Dual-Color Electroluminescence from Dot-in-Bulk Nanocrystals. *Nano Letters* **14**, 486-494, (2013).

189 Brovelli, S. *et al.* Fully inorganic oxide-in-oxide ultraviolet nanocrystal light emitting devices. *Nat Commun* **3**, 690, (2012).

190 Galland, C. *et al.* Two types of luminescence blinking revealed by spectroelectrochemistry of single quantum dots. *Nature* **479**, 203-207, (2011).

191 Klimov, V. I. *Nanocrystal quantum dots*. (CRC Press, 2010).

192 Nazzal, A. Y., Qu, L., Peng, X. & Xiao, M. Photoactivated CdSe Nanocrystals as Nanosensors for Gases. *Nano Letters* **3**, 819-822, (2003).

193 Pick Chung, L., Robert, A. N., Masud, M. & Nasser, P. An effective and simple oxygen nanosensor made from MPA-capped water soluble CdTe nanocrystals. *Nanotechnology* **24**, 015501, (2013).

194 Pechstedt, K., Whittle, T., Baumberg, J. & Melvin, T. Photoluminescence of Colloidal CdSe/ZnS Quantum Dots: The Critical Effect of Water Molecules. *The Journal of Physical Chemistry C* **114**, 12069-12077, (2010).

195 Ma, J. *et al.* Photostability of thiol-capped CdTe quantum dots in living cells: the effect of photo-oxidation. *Nanotechnology* **17**, 2083, (2006).

196 Kameda, M., Seki, H., Makoshi, T., Amao, Y. & Nakakita, K. A fast-response pressure sensor based on a dye-adsorbed silica nanoparticle film. *Sensors and Actuators B: Chemical* **171–172**, 343-349, (2012).

197 Gouterman, M. Oxygen Quenching of Luminescence of Pressure Sensitive Paint for Wind Tunnel Research. *Journal of Chemical Education* **74**, 697, (1997).

198 Xiang, H. *et al.* Tunable Fluorescent/Phosphorescent Platinum(II) Porphyrin–Fluorene Copolymers for Ratiometric Dual Emissive Oxygen Sensing. *Inorganic Chemistry* **51**, 5208-5212, (2012).

199 Park, J. *et al.* Quantum Dots in an Amphiphilic Polyethyleneimine Derivative Platform for Cellular Labeling, Targeting, Gene Delivery, and Ratiometric Oxygen Sensing. *ACS Nano*, (2015).

200 Amelia, M., Lavie-Cambot, A., McClenaghan, N. D. & Credi, A. A ratiometric luminescent oxygen sensor based on a chemically functionalized quantum dot. *Chem. Comm.* **47**, 325-327, (2011).

201 Borisov, S. M. & Klimant, I. A versatile approach for ratiometric time-resolved read-out of colorimetric

chemosensors using broadband phosphors as secondary emitters. *Analytica Chimica Acta* **787**, 219-225, (2013).

202 Baleizão, C., Nagl, S., Schäferling, M., Berberan-Santos, M. N. & Wolfbeis, O. S. Dual Fluorescence Sensor for Trace Oxygen and Temperature with Unmatched Range and Sensitivity. *Analytical Chemistry* **80**, 6449-6457, (2008).

203 Zhang, G., Palmer, G. M., Dewhirst, M. W. & Fraser, C. L. A dual-emissive-materials design concept enables tumour hypoxia imaging. *Nat Mater* **8**, 747-751, (2009).

204 Galland, C. *et al.* Dynamic Hole Blockade Yields Two-Color Quantum and Classical Light from Dot-in-Bulk Nanocrystals. *Nano Letters* **13**, 321-328, (2012).

205 Choi, J.-H. *et al.* In Situ Repair of High-Performance, Flexible Nanocrystal Electronics for Large-Area Fabrication and Operation in Air. *ACS Nano* **7**, 8275-8283, (2013).

206 Javaux C *et al.* Thermal activation of non-radiative Auger recombination in charged colloidal nanocrystals. *Nat Nano* **8**, 206-212, (2013).

207 Liu, F. *et al.* Spin dynamics of negatively charged excitons in CdSe/CdS colloidal nanocrystals. *Physical Review B* **88**, 035302, (2013).

208 Javaux, C. *et al.* Thermal activation of non-radiative Auger recombination in charged colloidal nanocrystals. *Nat. Nanotechnol.* **8**, 206-212, (2013).

209 Jha, P. P. & Guyot-Sionnest, P. Trion Decay in Colloidal Quantum Dots. *ACS Nano* **3**, 1011-1015, (2009).

210 Park, Y. S. *et al.* Near-Unity Quantum Yields of Biexciton Emission from CdSe/CdS Nanocrystals Measured Using Single-Particle Spectroscopy. *Physical Review Letters* **106**, 187401, (2011).

211 Nasilowski, M., Spinicelli, P., Patriarche, G. & Dubertret, B. Gradient CdSe/CdS Quantum Dots with Room Temperature Biexciton Unity Quantum Yield. *Nano Letters*, (2015).

212 Robel, I., Gresback, R., Kortshagen, U., Schaller, R. D. & Klimov, V. I. Universal Size-Dependent Trend in Auger Recombination in Direct-Gap and Indirect-Gap Semiconductor Nanocrystals. *Physical Review Letters* **102**, 177404, (2009).

213 Lakowicz, J. *Principles of Fluorescence Spectroscopy*. 3rd edn, (Springer, 2006).